Unterschrift BetreuerIn

TECHNISCHE
UNIVERSITÄT
WIEN

DIPLOMARBEIT

The Influence of Higher-Order Modes on Gravitational Waveforms and Parameter Estimation Bias for Intermediate-Mass Black Hole Mergers

ausgeführt am Atominstitut
der Technischen Universität Wien

unter der Anleitung von
Dr. Gianluca Inguglia
Priv.-Doz. DI Dr. Christoph Schwanda

durch

Melvin Cap BSc

December 12, 2024

Unterschrift StudentIn

Die approbierte gedruckte Originalversion dieser Diplomarbeit ist an der TU Wien Bibliothek verfügbar
The approved original version of this thesis is available in print at TU Wien Bibliothek.
TU Bibliothek Your knowledge hub WIEN

Die approbierte gedruckte Originalversion dieser Diplomarbeit ist an der TU Wien Bibliothek verfügbar
The approved original version of this thesis is available in print at TU Wien Bibliothek.

Abstract

Gravitational waves, ripples in spacetime predicted by General Relativity, have transformed our understanding of astrophysical phenomena. IMBHs bridge the gap between stellar black holes and super massive black holes, offering unique insights into astrophysics and cosmology. This thesis focuses on advancing our understanding of gravitational waves from IMBH systems, particularly through the study of higher-order modes and parameter estimation biases.

This work analyses higher-order modes in gravitational waveforms, identifying patterns and quantifying their relative power. It also evaluates how waveform approximants in Bayesian parameter estimation introduce biases, affecting source characterization and population studies.

These findings highlight the role of higher order modes from Intermediate Mass Black Holes (IMBH) systems with high mass ratios and specific inclinations. It draws attention to the need to carefully choose waveform models in order to avoid systematic biases.

Abstract

Gravitationswellen, als Raumzeitkräuselungen von der Allgemeinen Relativitätstheorie vorhergesagt, haben unser Verständnis astrophysikalischer Phänomene revolutioniert. IMBHs (Intermediate-Mass Black Holes) schlagen eine Brücke zwischen stellaren und supermassiven Schwarzen Löchern und bieten einzigartige Einblicke in die Astrophysik und Kosmologie. Diese Arbeit konzentriert sich darauf, unser Verständnis von Gravitationswellen aus IMBH-Systemen zu vertiefen, insbesondere durch die Untersuchung höherer Ordnungen (higher-order modes) und der Verzerrungen in der Parameterabschätzung.

Diese Arbeit analysiert höhere Ordnungen in Gravitationswellenformen, identifiziert Muster und quantifiziert deren relative Stärke. Zudem wird untersucht,

Die approbierte gedruckte Originalversion dieser Diplomarbeit ist an der TU Wien Bibliothek verfügbar
The approved original version of this thesis is available in print at TU Wien Bibliothek.

wie Wellenform-Approximationen in der Bayesschen Parameterabschätzung Verzerrungen einführen, die die Charakterisierung von Quellen und Populationsstudien beeinflussen können.

Diese Ergebnisse unterstreichen die Rolle höherer Ordnungsmoden bei Systemen mit IMBH, die hohe Massenverhältnisse und bestimmte Neigungen aufweisen. Sie weisen auf die Notwendigkeit hin, Wellenformmodelle sorgfältig auszuwählen, um systematische Fehler zu vermeiden.

Die approbierte gedruckte Originalversion dieser Diplomarbeit ist an der TU Wien Bibliothek verfügbar
The approved original version of this thesis is available in print at TU Wien Bibliothek.
TU Bibliothek Your knowledge hub WIEN

Contents

Die approbierte gedruckte Originalversion dieser Diplomarbeit ist an der TU Wien Bibliothek verfügbar
The approved original version of this thesis is available in print at TU Wien Bibliothek.
TU Bibliothek Your knowledge hub WIEN

Die approbierte gedruckte Originalversion dieser Diplomarbeit ist an der TU Wien Bibliothek verfügbar
The approved original version of this thesis is available in print at TU Wien Bibliothek.
TU Bibliothek Your knowledge hub WIEN

1. Introduction

Gravitational waves, the ripples in the fabric of spacetime predicted by Einstein's General Theory of Relativity, represent one of the most transformative discoveries in modern physics. These waves, caused by the most extreme cosmic events—such as the mergers of black holes or neutron stars—have opened an entirely new observational window into the universe. Their detection provides not only confirmation of theoretical physics but also an unparalleled opportunity to study astrophysical phenomena that were previously beyond reach. The first direct detection in 2015 by the LIGO-Virgo collaboration marked a monumental achievement, laying the foundation for the burgeoning field of gravitational wave astronomy.

Among the many discoveries made through gravitational waves, intermediate-mass black holes (IMBHs) stand out as particularly interesting. IMBHs occupy the mass range between stellar-mass black holes, which are formed from the collapse of massive stars, and supermassive black holes, which dominate the centers of galaxies. Despite their theoretical importance, IMBHs have remained elusive, with few detected candidates. Their formation mechanisms and evolution remain open questions. The detection of events such as GW190521, which provided compelling evidence of an IMBH merger, has propelled these enigmatic objects into the spotlight, challenging existing theories and highlighting the need for deeper exploration.

This thesis focuses on advancing our understanding of gravitational waves from IMBH systems, tackling two critical challenges: the influence of higher-order modes in gravitational waveforms and the biases introduced in parameter estimation by waveform approximants. Higher-order modes, often overshadowed by the dominant quadrupole mode, become increasingly significant in systems with large mass ratios or specific orbital inclinations. Their inclusion in waveform models is essential for accurately interpreting signals from IMBH systems, where such effects are more pronounced. Ignoring these contributions can lead to incomplete or biased astrophysical inferences.

In addition to exploring higher-order modes, this work evaluates the impact of waveform approximants on parameter estimation. The approximants used in Bayesian inference methods introduce biases that affect the accuracy of recovered

Die approbierte gedruckte Originalversion dieser Diplomarbeit ist an der TU Wien Bibliothek verfügbar
The approved original version of this thesis is available in print at TU Wien Bibliothek.
TU Bibliothek Your knowledge hub WIEN

source parameters, such as mass, spin, and distance. These biases are particularly consequential for IMBH systems, where accurate characterization is critical for understanding their formation and population dynamics. By identifying and quantifying these biases, this thesis aims to provide insights that can guide the development of more accurate waveform models and analysis pipelines.

By combining theoretical insights with numerical simulations, this study contributes to the growing understanding of IMBH systems and their gravitational wave signals. It highlights areas for improvement in current methods, emphasizing the importance of higher-order modes and accurate parameter estimation techniques. The findings presented here not only deepen our understanding of gravitational wave science but also provide a foundation for refining detection techniques, improving data analysis methods, and advancing astrophysical and cosmological interpretations. Through this work, the thesis aspires to bridge gaps in our knowledge and pave the way for more comprehensive studies of IMBHs and their role in the universe.

This thesis utilized different software tools to assist the generation of results. The Python libraries PyCBC [53] and GWSurrogate [14] for waveform simulation, bilby [10] for parameter estimation matplotlib [36] for generating visualizations and Generative AI tools [55] for assistance in writing.

Die approbierte gedruckte Originalversion dieser Diplomarbeit ist an der TU Wien Bibliothek verfügbar
The approved original version of this thesis is available in print at TU Wien Bibliothek.
TU Bibliothek Your knowledge hub WIEN

2. Theoretical Framework

In this chapter, we establish the theoretical foundation underlying the study of gravitational waves and their astrophysical sources. The discussion begins with an exploration of General Relativity, Einstein's revolutionary framework that redefined our understanding of gravity as the curvature of spacetime. This sets the stage for examining Einstein's Field Equations, the mathematical backbone of gravitational theory, and their implications for the existence of phenomena such as black holes and gravitational waves. We delve into the linearized approximation of General Relativity to describe gravitational waves, deriving key equations that govern their dynamics, propagation, and interaction with matter. Building on this, the multipole expansion technique is introduced to capture the complexities of higher-order modes that arise in strong-field scenarios. The chapter concludes with an overview of gravitational wave sources, with particular emphasis on the astrophysical events that generate these ripples in spacetime, such as binary black hole mergers and gravitational wave bursts. This theoretical framework provides the essential tools and insights for understanding the observational and computational studies that follow in later chapters.

2.1. General Relativity

Albert Einstein developed the General Theory of Relativity in 1915 as an extension of his earlier work on Special Relativity, aiming to address the limitations of Newtonian gravity. While Newton's theory treated gravity as an instantaneous force acting at a distance, Einstein's GR redefined gravity as the curvature of spacetime caused by mass and energy. This new approach resolved key issues such as the precession of Mercury's orbit and the bending of light by gravity (Gravitational lensing), effects that Newtonian mechanics could not fully explain [39].

2.1.1. Einstein's Field Equations

At the heart of General Relativity lie the Einstein Field Equations, a set of ten coupled differential equations that form the theoretical backbone of modern gravitational theory [18]. The equations relate the geometry of spacetime to the dis-

Die approbierte gedruckte Originalversion dieser Diplomarbeit ist an der TU Wien Bibliothek verfügbar
The approved original version of this thesis is available in print at TU Wien Bibliothek.

tribution of matter and energy, captured succinctly as

$$R_{\mu\nu} - \frac{1}{2}Rg_{\mu\nu} + \Lambda g_{\mu\nu} = \frac{8\pi G}{c^4}T_{\mu\nu} \tag{2.1}$$

Each term in this equation carries profound meaning, revealing how matter influences spacetime itself:

- $R_{\mu\nu}$: This is the Ricci curvature tensor, describing how spacetime is curved by the presence of mass and energy in a specific direction. It encapsulates the "local" curvature that reflects how matter affects the bending of spacetime in nearby regions.
- R: The scalar curvature, a single value derived from the Ricci tensor, represents the overall curvature of spacetime at a given point. It gives a more global sense of how spacetime is shaped by all sources of gravity.
- $g_{\mu\nu}$: This is the metric tensor, which defines the structure of spacetime, including distances and angles. It acts as the foundational "map" of spacetime that the other terms modify according to the presence of mass and energy.
- Λ: Known as the cosmological constant, this term accounts for the energy density of empty space, or "dark energy." It was initially introduced by Einstein to allow for a static universe, but today it is used to explain the observed accelerated expansion of the universe.
- $T_{\mu\nu}$: The stress-energy tensor, which encompasses the distribution and flow of energy and momentum in spacetime. It includes all forms of energy, such as matter, radiation, and even pressure, thus representing the "source" term in the equation.

The equation as a whole tells us that spacetime geometry ($R_{\mu\nu}$, R, and $g_{\mu\nu}$) is shaped directly by the presence and distribution of matter and energy ($T_{\mu\nu}$), modulated by universal constants like Newton's gravitational constant G and the speed of light c. This concept is encapsulated by John Archibald Wheeler's well-known summary [50]:

"Space(time) tells matter how to move
Matter tells space(time) how to curve"[1]

[1]The original quote uses "space" instead of "spacetime." "Time" is included here in brackets for clarity.

Die approbierte gedruckte Originalversion dieser Diplomarbeit ist an der TU Wien Bibliothek verfügbar
The approved original version of this thesis is available in print at TU Wien Bibliothek.

2.1.2. Black Holes

One of the most significant consequences of Einstein's Field Equations is the prediction of black holes. First theorized by Schwarzschild in 1916 [62] and later reformulated by Droste [30], Hilbert [35], and Weyl [72] in 1917, black holes emerged as peculiar yet inevitable consequences of Einstein's theory of gravitation. These objects represent regions of spacetime where gravity is so extreme that nothing, not even light, can escape. Within this boundary, defined by the event horizon, lies a gravitational singularity where the curvature of spacetime becomes infinite.

In the early 20th century, theoretical work by Landau [45] and Chandrasekhar [21] [22] demonstrated that black holes are potentially the natural endpoints of massive stars collapsing under their own gravity. However, black holes remained a theoretical concept until 1972, when the "dark" companion in the Cygnus X-1 binary system was dynamically confirmed to have several solar masses [71], firmly establishing it as a stellar-mass black hole. This breakthrough was followed by numerous observations of black hole X-ray binaries [57] [19], further supporting the abundance of stellar-mass black holes in the Universe. The detection of gravitational waves in 2015 [1] from binary black hole mergers provided direct evidence of their existence and properties, marking a new era in black hole astrophysics.

While the mathematical derivation and detailed properties of black hole solutions are of significant interest, these aspects will not be the focus here. A comprehensive mathematical treatment can be found in standard sources such as [50] [18].

Classification of Black Holes

Black holes can be classified into categories based on their masses: primordial, stellar, intermediate, and supermassive black holes. Each class reflects unique physical characteristics and astrophysical origins.

Primordial black holes (PBHs) are hypothetical black holes that may have formed in the early universe due to density fluctuations shortly after the Big Bang [33]. Unlike stellar-mass black holes, PBHs are not remnants of stellar evolution but rather the result of regions of spacetime collapsing under extreme conditions in the universe's first moments. Depending on their formation mechanisms, PBHs can span a wide mass range, from subatomic scales to hundreds of solar masses. While no conclusive evidence for PBHs exists, they remain an active area of research, particularly as potential candidates for dark matter.

Stellar-mass black holes, on the other hand, are formed from the gravitational

Die approbierte gedruckte Originalversion dieser Diplomarbeit ist an der TU Wien Bibliothek verfügbar
The approved original version of this thesis is available in print at TU Wien Bibliothek.
TU Bibliothek Your knowledge hub WIEN

collapse of massive stars ($> 8M_{\odot}$) at the end of their life cycles, typically as a result of supernova explosions. Their masses range from a few solar masses to approximately 100 solar masses [20]. These black holes are often observed in binary systems, where they accrete matter from a companion star. This accretion process generates X-rays, making them detectable through X-ray astronomy. Gravitational waves emitted by merging stellar-mass black holes have also been detected, providing a powerful tool for studying these systems.

Supermassive black holes (SMBHs) dominate the centers of most, if not all, massive galaxies, with masses ranging from $10^5 M_{\odot}$ to $10^{10} M_{\odot}$. Their formation remains a subject of intense research, with proposed mechanisms including the direct collapse of gas clouds in the early universe, prolonged accretion of matter over cosmic timescales, and mergers of smaller black holes. The presence of SMBHs was first suggested in the 1970s, based on dynamical measurements of stellar motions near galactic centers [61]. Subsequent observational evidence has solidified this hypothesis, with notable examples including the 4 million $M_{\odot}$ SMBH at the center of the Milky Way and the imaging of the SMBH in M87 by the Event Horizon Telescope [23].

Intermediate Mass Black Holes

Intermediate-mass black holes occupy a unique position in the black hole mass spectrum, with masses ranging from $10^2 M_{\odot}$ to $10^5 M_{\odot}$. They are hypothesized to bridge the gap between stellar-mass black holes, which form from the collapse of individual stars, and supermassive black holes, which dominate the centers of galaxies. Despite their theoretical importance, the existence and formation of IMBHs have remained enigmatic due to the constraints imposed by stellar physics and astrophysical processes.

A central challenge to the formation of IMBHs arises from the phenomena of the pair-instability supernova (PISN) and pulsation pair instability supernova (PPISN). Stars in a specific mass range, experience conditions in their cores where thermal radiation becomes energetic enough to produce electron-positron pairs [73]. This process reduces the radiation pressure supporting the core against gravitational collapse, leading to a runaway contraction. The contraction heats the core further, igniting explosive thermonuclear reactions that result in either a complete disruption of the star or significant mass loss. Consequently, no black hole remnants are expected to form from stars in this range, creating what is known as the "PISN mass gap." Black holes with masses between $50M_{\odot}$ and $130M_{\odot}$

Die approbierte gedruckte Originalversion dieser Diplomarbeit ist an der TU Wien Bibliothek verfügbar
The approved original version of this thesis is available in print at TU Wien Bibliothek.
TU Bibliothek Your knowledge hub WIEN

should, therefore, be exceedingly rare, as the progenitor stars are entirely disrupted. These processes impose strict constraints on the formation of black holes in the low intermediate-mass range.

Several alternative formation mechanisms have been proposed to explain the existence of IMBHs. A comprehensive discussion can be found in [11]:

- Population III and Metal-Poor Stars: IMBHs can form as remnants of very massive stars (VMSs) with initial masses exceeding $200M_{\odot}$, particularly in the early universe where metallicity was extremely low. These stars evolve over a few million years and may directly collapse into black holes with masses exceeding $100M_{\odot}$ [48]. For metal-poor stars (Population II), weak stellar winds due to low metallicity allow VMSs with zero-age main sequence masses $\gtrsim 250M_{\odot}$ to retain most of their mass during evolution. These stars could also directly collapse to form IMBHs without undergoing supernova explosions [66].
- Formation in Dense Stellar Environments: IMBHs can also form through dynamic processes in dense stellar systems such as globular clusters, nuclear star clusters, and young massive clusters. The high stellar densities in these environments promote gravitational interactions, leading to the formation and growth of massive black holes. An overview is given in figure 2.1. One of the most prominent theories is the *Repeated or hierarchical mergers of stellar-mass BHs*. In clusters where stellar-mass black holes are retained, dynamical friction causes them to segregate into the cluster core. There, stellar black holes interact gravitationally, forming binary systems that eventually merge via gravitational wave emission. The merged black holes can repeat this process, growing into more massive black holes [59] [9].

Despite their elusive nature, compelling evidence for IMBHs has begun to emerge in recent years. Observations of ultraluminous X-ray sources have revealed objects with luminosities too high to be explained by stellar-mass black holes, suggesting IMBHs as potential sources. Dynamical measurements of stellar motions in some globular clusters, such as 47 Tucanae, also hint at the presence of central black holes with intermediate masses [49].

A breakthrough in the search for IMBHs came with the detection of the gravitational wave event GW190521 in 2019. This event involved the merger of two black holes, resulting in a remnant with a total mass of approximately $150M_{\odot}$, firmly placing it in the intermediate-mass range. The component black holes themselves

Die approbierte gedruckte Originalversion dieser Diplomarbeit ist an der TU Wien Bibliothek verfügbar
The approved original version of this thesis is available in print at TU Wien Bibliothek.

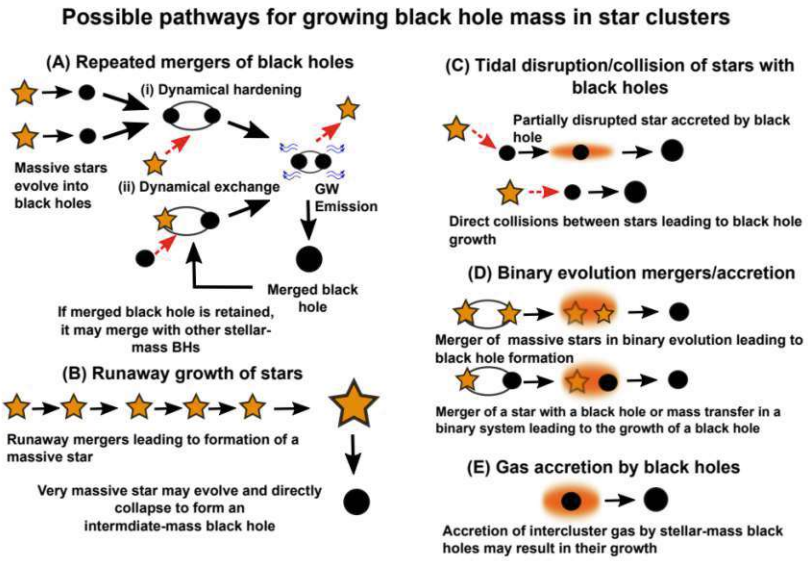

Figure 2.1.: Illustration of potential pathways for the growth of IMBHs in star clusters: (A) Mergers of dynamically formed binary black holes through gravitational wave emission within the cluster. (B) In extremely dense star clusters ($\gtrsim 10^6\, M_\odot\, \mathrm{pc}^{-3}$), runaway mergers between stars can occur, resulting in the formation of a very massive star (greater than a few hundred $M_\odot$), which may collapse into an IMBH of similar mass. (C) Growth of black holes through the tidal disruption or direct collisions with stars in the cluster. (D) Evolution of binary systems, where two massive stars merge to form a single large black hole, or accretion of material from a companion star by a black hole in a binary system, contributing to black hole growth. (E) Accretion of interstellar gas by black holes within the cluster, leading to further mass increase [11].

had masses of $85M_\odot$ and $66M_\odot$, placing one of them within the PISN gap. This discovery challenged our understanding of stellar evolution and black hole formation, suggesting that alternative processes, such as hierarchical mergers, may play a significant role in producing IMBHs [27].

2.2. Gravitational Waves in linearized Gravity

The Einstein Field Equations establish the profound relationship between matter and spacetime curvature, illustrating that mass and energy shape the very fabric of spacetime itself. However, to get a feeling of dynamic phenomena like gravitational waves let's get more technical and consider a regime where gravitational

Die approbierte gedruckte Originalversion dieser Diplomarbeit ist an der TU Wien Bibliothek verfügbar
The approved original version of this thesis is available in print at TU Wien Bibliothek.

fields are weak. In this weak-field limit, we can linearize the Einstein Field Equations, simplifying them to describe small perturbations in spacetime rather than full curvature.

This linearization process allows us to derive the equation of motion for gravitational waves, which reveals how these waves propagate and interact with matter. In the following technical sections, we derive the equations of motion for linearized gravity, discuss gravitational wave solutions, examine their effects, and explore their production. This foundation for understanding gravitational waves is primarily based on Carroll's comprehensive resource [18].

In the following discussion, we adopt natural units where $c = 1$, simplifying the equations by setting the speed of light to unity. Additionally, the metric convention $(-,+,+,+)$ is used, which assigns a negative sign to the time component and positive signs to the spatial components of the metric.

2.2.1. Equation of motion

The metric in the weak field approximation can be decomposed into the flat Minkowski metric and a small pertubation

$$g_{\mu\nu} = \eta_{\mu\nu} + h_{\mu\nu}, \quad |h_{\mu\nu}| \ll 1 \tag{2.2}$$

This assumptions allows us to ignore terms of $\mathcal{O}(h^2)$. Therefore the metric with upper indices is given by [2]

$$g^{\mu\nu} = \eta^{\mu\nu} - h^{\mu\nu} \tag{2.3}$$

The goal now is to find the equations of motion which governs the dynamics of the pertubation $h_{\mu\nu}$. These can be derived by evaluating Einsteins equations to first order. since the derivation of the Ricci tensor and Ricci scalar requires the Riemann tensor, we must first construct the linearized Riemann tensor and then trace its indices. The Riemann tensor itself is expressed in terms of the Christoffel symbols Γ and their products Γ^2. Because the Christoffel symbols are first order quantities the only contribution comes from the derivative of the Γ-terms while neglecting the $\mathcal{O}(\Gamma^2)$

$$\begin{aligned}\Gamma^{\rho}_{\mu\nu} &= \frac{1}{2}\eta^{\rho\lambda}\left(\partial_\mu g_{\nu\lambda} + \partial_\nu g_{\mu\lambda} - \partial_\lambda g_{\mu\nu}\right) \\ &= \frac{1}{2}\eta^{\rho\lambda}\left(\partial_\mu h_{\nu\lambda} + \partial_\nu h_{\mu\lambda} - \partial_\lambda h_{\mu\nu}\right)\end{aligned} \tag{2.4}$$

[2] Derivation can be found in A.1

Die approbierte gedruckte Originalversion dieser Diplomarbeit ist an der TU Wien Bibliothek verfügbar
The approved original version of this thesis is available in print at TU Wien Bibliothek.

The linearized Riemann tensor, with only lower indices for convenience, can therefore be expressed as

$$\begin{aligned} R_{\mu\nu\rho\sigma} &= \eta_{\mu\lambda}\partial_\rho\Gamma^\lambda_{\nu\sigma} - \eta_{\mu\lambda}\partial_\sigma\Gamma^\lambda_{\nu\rho} \\ &= \frac{1}{2}\left(\partial_\rho\partial_\nu h_{\mu\sigma} + \partial_\sigma\partial_\mu h_{\nu\rho} - \partial_\rho\partial_\mu h_{\nu\sigma} - \partial_\sigma\partial_\nu h_{\mu\rho}\right) \end{aligned} \tag{2.5}$$

Contracting[3] over σ and ρ yields the linearized Ricci tensor

$$R_{\mu\nu} = \frac{1}{2}\left(\partial_\alpha\partial_\nu h_\mu{}^\alpha + \partial_\mu\partial^\alpha h_{\nu\alpha} - \partial_\mu\partial_\nu h - \Box h_{\mu\nu}\right) \tag{2.6}$$

where $\Box = -\partial_t^2 + \partial_x^2 + \partial_y^2 + \partial_z^2$ denotes the d'Alembertian operator in flat space. The final contraction gives the linearized Ricci scalar

$$R = \partial_\mu\partial_\nu h^\mu\nu - \Box h \tag{2.7}$$

Combining all terms, we obtain the following expression for the left-hand side[4](2.1)

$$R_{\mu\nu} - \frac{1}{2}\eta_{\mu\nu}R = \frac{1}{2}\left(\partial_\alpha\partial_\nu h_\mu{}^\alpha + \partial_\mu\partial^\alpha h_{\nu\alpha} - \partial_\mu\partial_\nu h - \Box h_{\mu\nu} - \eta_{\mu\nu}\partial_\alpha\partial_\beta h^{\alpha\beta} - \eta_{\mu\nu}\Box h\right) \tag{2.8}$$

Equation 2.2 does not fully determine the coordinate system, as redundant degrees of freedom remain. This redundancy implies that different perturbations can describe the same physical situation, differing only by terms that can be eliminated through coordinate transformations, commonly referred to as *gauge transformations*. The pertubation transforms under an infinitesimal coordinate transformation as[5]

$$h'_{\mu\nu} = h_{\mu\nu} - \partial_\mu\xi_\nu - \partial_\nu\xi_\mu. \tag{2.9}$$

Before we now set a specific gauge condition it is useful to decompose the pertubation into pieces that transform only into themselves under SO(3)[6]. Similar to how the Field strenght tensor in electrodynamics can be decomposed into E and B. We focus on the rotation group SO(3) because gravitational waves primarily manifest through spatial distortions in spacetime. Consequently, we do not employ the full irreducible representations of the Poincaré group[7], as incorporating boosts introduces additional complexity by mixing spatial and temporal components of the metric perturbations. Furthermore, translations are neglected since they only affect the overall position in spacetime without altering the local structure of the

[3] $R_{\mu\nu} = \eta^{\sigma\alpha}\eta^{\rho\alpha}R_{\mu\nu\rho\sigma}$
[4] Replacing $g_{\mu\nu} = \eta_{\mu\nu} + h_{\mu\nu}$ in $g_{\mu\nu}R$ leaves only $\eta_{\mu\nu}R$, as $h_{\mu\nu}R$ is second order.
[5] Derived in A.2
[6] spatial rotations
[7] underlying symmetry group of relativity

Die approbierte gedruckte Originalversion dieser Diplomarbeit ist an der TU Wien Bibliothek verfügbar
The approved original version of this thesis is available in print at TU Wien Bibliothek.
TU Bibliothek Your knowledge hub WIEN

perturbations in a manner that necessitates decomposition based on their transformation properties. The components of the perturbation $h_{\mu\nu}$ are given by

$$h_{00} = -2\Phi, \quad h_{0i} = w_i, \quad h_{ij} = 2s_{ij} - 2\Psi\delta_{ij}, \tag{2.10}$$

where Ψ encodes the trace of h_{ij} as

$$\Psi = -\frac{1}{6}\delta^{ij}h_{ij}, \tag{2.11}$$

and the strain s_{ij} is traceless

$$s_{ij} = \frac{1}{2}\left(h_{ij} - \frac{1}{3}\delta_{ij}\delta^{kl}h_{kl}\right). \tag{2.12}$$

Utilizing the *transverse gauge* which is similar to the Coulomb gauge[8] in Electrodynamics fixes the strain to be spatially transverse by imposing

$$\begin{aligned} \partial_i s^{ij} &= 0 \\ \partial_i w^i &= 0 \end{aligned} \tag{2.13}$$

These conditions transform Einstein's equations into its transverse gauge

$$2\nabla^2\Psi = 8\pi G T_{00} \tag{2.14}$$

$$-\frac{1}{2}\nabla^2 w_j + 2\partial_0\partial_j\Psi = 8\pi G T_{0j} \tag{2.15}$$

$$\left(\delta_{ij}\nabla^2 - \partial_i\partial_j\right)(\Phi - \Psi) - \partial_0\partial_{(i}\omega_{j)} + 2\delta_{ij}\partial_0^2\Psi - \Box s_{ij} = 8\pi G T_{ij} \tag{2.16}$$

Now we want to study the freely propagating degrees of freedom of the gravitational field that do not require any local sources for their existence. Therefore, we set the stress-energy tensor to zero, $T_{\mu\nu} = 0$. This results in the following equations: For the 00-component

$$\nabla^2\Psi = 0, \tag{2.17}$$

for the $0i$-component

$$\nabla^2 w_j = 0, \tag{2.18}$$

and, taking the trace of the ij-component, we obtain

$$\nabla^2\Phi = 0. \tag{2.19}$$

Since all three equations are Laplace equations for Ψ, w_j, and Φ, respectively, the solutions must be unique under specific boundary conditions, leading to $\psi = 0$,

[8] $\partial_i A^i = 0$

Die approbierte gedruckte Originalversion dieser Diplomarbeit ist an der TU Wien Bibliothek verfügbar
The approved original version of this thesis is available in print at TU Wien Bibliothek.

$w_j = 0$, and $\Phi = 0$ throughout the domain. According to the *uniqueness theorem for Laplace's equation*, if Ψ, w_j, and Φ satisfy $\nabla^2\Psi = 0$, $\nabla^2 w_j = 0$, and $\nabla^2\Phi = 0$ within a domain and are zero on the boundary, then the only solution consistent with these conditions is $\Psi = 0$, $w_j = 0$, and $\Phi = 0$ everywhere inside the domain [32].[9]

We are therefore only left with the trace-free part of the ij-equation which becomes a wave equation for the traceless strain tensor

$$\Box s_{ij} = 0 \tag{2.20}$$

Although it has been convenient to work with s_{ij}, it is common in the literature to express the equations in terms of the total metric perturbation $h_{\mu\nu}$ while adopting an ansatz that isolates the other degrees of freedom (Ψ, Φ, ω_i)[10]. This approach is commonly referred to as the *transverse-traceless gauge*, with the metric perturbation written as

$$h^{\mathrm{TT}}_{\mu\nu} = \begin{pmatrix} 0 & 0 & 0 & 0 \\ 0 & & & \\ 0 & & 2s_{ij} & \\ 0 & & & \end{pmatrix}. \tag{2.21}$$

which ultimately leads to its equation of motion

$$\boxed{\Box h^{\mathrm{TT}}_{\mu\nu} = 0} \tag{2.22}$$

2.2.2. Gravitational Wave solutions

This is the first significant equation in linearized gravity without sources, showing that a small disturbance can exhibit modes that act as dynamic degrees of freedom, propagating through spacetime while satisfying the wave equation 2.22. These propagating solutions are what we refer to as *gravitational waves*.

To solve this equation of motion, a particularly useful approach is to consider a plane wave solution of the form

$$h^{\mathrm{TT}}_{\mu\nu} = C_{\mu\nu} e^{ik_\sigma x^\sigma} \tag{2.23}$$

where $C_{\mu\nu}$ is trivially traceless and purely spatial

$$\begin{aligned} C_{0\nu} &= 0 \\ \eta^{\mu\nu} C_{\mu\nu} &= 0 \end{aligned} \tag{2.24}$$

[9] This result also applies in unbounded domains when Ψ, w_j, and Φ are assumed to vanish at infinity.

[10] with s_{ij} taken to be transverse

Die approbierte gedruckte Originalversion dieser Diplomarbeit ist an der TU Wien Bibliothek verfügbar
The approved original version of this thesis is available in print at TU Wien Bibliothek.

Plugging this plane wave ansatz into 2.22 yields

$$\begin{aligned} 0 &= \Box h^{\mathrm{TT}}_{\mu\nu} && (2.25)\\ &= \eta^{\rho\sigma}\partial_\rho\partial_\sigma h^{\mathrm{TT}}_{\mu\nu} && (2.26)\\ &= \eta^{\rho\sigma}\partial_\rho\left(ik_\sigma h^{\mathrm{TT}}_{\mu\nu}\right) && (2.27)\\ &= -\eta^{\rho\sigma}k_\rho k_\sigma h^{\mathrm{TT}}_{\mu\nu} && (2.28)\\ &= -k_\sigma k^\sigma h^{\mathrm{TT}}_{\mu\nu} && (2.29) \end{aligned}$$

Since we are interested in the non trivial solution to this equation where $h^{\mathrm{TT}}_{\mu\nu} \neq 0$ we get the following condition for the wave vector

$$k_\sigma k^\sigma = 0 \tag{2.30}$$

Our ansatz satisfies the equation of motion provided that the wave vector is null, which implies that both the phase velocity v_p and the group velocity v_g of gravitational waves are equal to the speed of light[11].

Furthermore, we must ensure that the ansatz is transverse. This requirement translates to

$$\begin{aligned} 0 &= \partial_\mu h^{\mu\nu}_{\mathrm{TT}}\\ &= iC^{\mu\nu}k_\mu e^{ik_\sigma x^\sigma}, \end{aligned} \tag{2.31}$$

which leads to the condition

$$k_\mu C^{\mu\nu} = 0, \tag{2.32}$$

indicating that the wave vector k_μ is orthogonal to the coefficient tensor $C^{\mu\nu}$.

Let us consider a more concrete example by specifying propagation in the x^3 direction such that[12]

$$k^\mu = (\omega, 0, 0, k^3) = (\omega, 0, 0, \omega) \tag{2.33}$$

Conditions 2.32 and 2.24 imply that all coefficients with at least one index equal to 0 or 3 are zero. Therefore, the only nonzero components of $C_{\mu\nu}$ are C_{11}, C_{12}, C_{21}, and C_{22}.

[11] see Appendix A.3

[12] Utilizing the null property of the wave vector.

Die approbierte gedruckte Originalversion dieser Diplomarbeit ist an der TU Wien Bibliothek verfügbar
The approved original version of this thesis is available in print at TU Wien Bibliothek.

To ensure that $C_{\mu\nu}$ is both symmetric and traceless, we must impose the following constraints:

$$C_{22} = -C_{11}, \tag{2.34}$$
$$C_{12} = C_{21}. \tag{2.35}$$

Consequently, the coefficient tensor $C_{\mu\nu}$ takes the following form

$$C_{\mu\nu} = \begin{pmatrix} 0 & 0 & 0 & 0 \\ 0 & C_{11} & C_{12} & 0 \\ 0 & C_{12} & -C_{11} & 0 \\ 0 & 0 & 0 & 0 \end{pmatrix} \tag{2.36}$$

2.2.3. Effect of gravitational waves

In order to understand the impact of gravitational waves on matter, consider two particles separated by a separation vector S^μ. Let's analyze this scenario in the comoving frame, where the two particles exhibit no relative motion toward or away from each other. In this frame, each particle follows its own geodesic[13] while the separation vector S^μ quantifies the spacetime distance between these geodesics.

When a gravitational wave, which can be conceptualized as a localized curvature disturbance, traverses the region containing the two geodesics, it induces specific distortions in their paths. The geodesic deviation equation characterizes the relative acceleration, or the change in the separation vector, between the two geodesics. This equation is expressed as

$$\frac{D^2 S^\mu}{d\tau^2} = R^\mu{}_{\nu\rho\sigma} U^\nu U^\rho S^\sigma, \tag{2.37}$$

where D is the directional covariant derivative $\frac{D}{d\tau} = \frac{dx^\mu}{d\tau}\nabla_\mu$. This equation describes how spacetime curvature, as encoded in the Riemann tensor, affects the relative acceleration between nearby geodesics.

Since the particles are stationary in their rest frame, their four-velocity through spacetime is

$$U^\nu = (1, 0, 0, 0). \tag{2.38}$$

Substituting the four-velocity U^ν into Equation (2.37) simplifies the computation of the Riemann tensor. Therefore we only need to calculate components $R^\mu_{00\sigma}$ or

[13] the straightest possible path in a given spacetime

Die approbierte gedruckte Originalversion dieser Diplomarbeit ist an der TU Wien Bibliothek verfügbar
The approved original version of this thesis is available in print at TU Wien Bibliothek.

equivalently $R_{\mu 00\sigma}$. Recalling the linearized expression for the Riemann tensor from Equation 2.5, we have

$$R_{\mu 00\sigma} = \frac{1}{2}\left(\partial_0\partial_0 h^{\mathrm{TT}}_{\mu\sigma} + \partial_\sigma\partial_\mu h^{\mathrm{TT}}_{00} - \partial_\sigma\partial_0 h^{\mathrm{TT}}_{\mu 0} - \partial_\mu\partial_0 h^{\mathrm{TT}}_{\sigma 0}\right), \tag{2.39}$$

However, in the TT gauge, the perturbation $h^{\mathrm{TT}}_{\mu\nu}$ is purely spatial, as established in Equation 2.24. This implies that $h^{\mathrm{TT}}_{\mu 0} = 0$. Consequently, the Riemann tensor simplifies to

$$R_{\mu 00\sigma} = \frac{1}{2}\partial_0\partial_0 h^{\mathrm{TT}}_{\mu\sigma}. \tag{2.40}$$

Utilizing the fact that, for stationary particles, the proper time τ coincides with the coordinate time t, Equation (2.37) reduces to

$$\frac{\partial^2 S^\mu}{\partial t^2} = \frac{1}{2} S^\sigma \frac{\partial^2 h^{\mathrm{TT}\mu}_{\sigma}}{\partial t^2}. \tag{2.41}$$

Consider a gravitational wave propagating exclusively in the x^3-direction (z-direction). In this scenario, only the spatial components S^1 and S^2 of the separation vector S^μ are affected, as the components involving the x^3 index vanish due to the propagation direction of the wave.

Since the gravitational wave is characterized by two polarization states, we define the polarization amplitudes as follows for convenience

$$\begin{aligned} h_+ &= C_{11}, \\ h_\times &= C_{12}. \end{aligned} \tag{2.42}$$

With these definitions, the coefficient tensor $C_{\mu\nu}$ has the form

$$C_{\mu\nu} = \begin{pmatrix} 0 & 0 & 0 & 0 \\ 0 & h_+ & h_\times & 0 \\ 0 & h_\times & -h_+ & 0 \\ 0 & 0 & 0 & 0 \end{pmatrix}. \tag{2.43}$$

Let us look at the two polarizations independelty starting with the case $h_\times = 0$. Equation 2.41 simplifies to

$$\frac{\partial^2}{\partial t^2} S^1 = \frac{1}{2} S^1 \frac{\partial^2}{\partial t^2}\left(h_+ e^{ik_\sigma x^\sigma}\right) \tag{2.44}$$

and

$$\frac{\partial^2}{\partial t^2} S^2 = -\frac{1}{2} S^2 \frac{\partial^2}{\partial t^2}\left(h_+ e^{ik_\sigma x^\sigma}\right) \tag{2.45}$$

Die approbierte gedruckte Originalversion dieser Diplomarbeit ist an der TU Wien Bibliothek verfügbar
The approved original version of this thesis is available in print at TU Wien Bibliothek.
TU Bibliothek Your knowledge hub WIEN

We now proceed to solve the governing equations. Due to the symmetry of the equations, it suffices to solve one of them. The solution to the other can be obtained by incorporating the appropriate negative sign. Considering that h_+ represents a small perturbation, we adopt a first-order perturbative approach. This implies that the separation vector S^1 deviates only slightly from its unperturbed state $S^1(0)$. Consequently, the separation vector can be approximated to first order as

$$S^1(t) = S^1(0) + \delta S^1(t). \tag{2.46}$$

Substituting this ansatz into equation (2.44), the equation simplifies to

$$\frac{\partial^2 S^1}{\partial t^2} \approx \frac{1}{2} S^1(0) \frac{\partial^2}{\partial t^2} \left(h_+ e^{ik_\sigma x^\sigma} \right). \tag{2.47}$$

Integrating this expression twice and applying the initial conditions - namely, that the initial velocity is zero and the initial separation corresponds to the unperturbed state - we obtain

$$S^1(t) = \left(1 + \frac{1}{2} h_+ e^{ik_\sigma x^\sigma} \right) S^1(0). \tag{2.48}$$

Similarly, for S^2, the solution is

$$S^2(t) = \left(1 - \frac{1}{2} h_+ e^{ik_\sigma x^\sigma} \right) S^2(0). \tag{2.49}$$

These results indicate that the separation vector in the x^1-direction remains aligned with the x^1-axis but undergoes oscillatory shrinking and squeezing. If particles are arranged in a ring, they would oscillate back and forth, maintaining a plus-shaped configuration.

Performing a similar analysis for the case where $h_+ = 0$ yields the solutions

$$S^1(t) = S^1(0) + \frac{1}{2} h_+ e^{ik_\sigma x^\sigma} S^2(0), \tag{2.50}$$

and

$$S^2(t) = S^2(0) + \frac{1}{2} h_+ e^{ik_\sigma x^\sigma} S^1(0). \tag{2.51}$$

These solutions imply that the ring of particles oscillates in an $\times$-shaped pattern, ultimately clarifying the used notation.

These independent modes can be combined to construct also circular polarized modes by defining

$$\begin{aligned} h_R &= \frac{1}{2} \left(h_+ + i h_\times \right) \\ h_L &= \frac{1}{2} \left(h_+ - i h_\times \right) \end{aligned} \tag{2.52}$$

Die approbierte gedruckte Originalversion dieser Diplomarbeit ist an der TU Wien Bibliothek verfügbar
The approved original version of this thesis is available in print at TU Wien Bibliothek.

We can relate the polarization states of classical gravitational waves to the type of particles that would emerge upon quantization. The spin of a quantized field is determined by the angle under spatial rotations that leaves the polarization invariant, and is given by

$$S = \frac{360°}{\theta} \tag{2.53}$$

As shown in the Appendix A.4, for gravitational waves this angle is $\theta = 180°$, indicating that gravitons would have

$$S = 2 \tag{2.54}$$

2.2.4. Production of gravitational waves

In the previous section, we only considered the possible modes of gravitational waves that can propagate through spacetime. Now, we will examine their production. To do so, we must consider a non-vanishing energy-momentum tensor $T_{\mu\nu}$. For this analysis, the transverse-traceless gauge is not the most suitable. Instead, we work with the full perturbation $h_{\mu\nu}$ and solve for the produced gravitational waves far from the source, where we can then impose the transverse-traceless gauge. Some simplifications can be made in advance. Let us define the trace-reversed perturbation[14]

$$\bar{h}_{\mu\nu} = h_{\mu\nu} - \frac{1}{2} h \eta_{\mu\nu} \tag{2.55}$$

A suitable gauge choice for this investigation is the Lorenz gauge[15]

$$\partial_\mu \bar{h}^{\mu\nu} = 0 \tag{2.56}$$

Using this gauge, along with Equation 2.8, yields the Einstein equations in this gauge, which reduce to a wave equation for each component

$$\Box \bar{h}_{\mu\nu} = -16\pi G T_{\mu\nu} \tag{2.57}$$

This equation can be solved using Green's functions. Here, we outline the method as presented in [70].

The Green function $G(x^\sigma - y^\sigma)$ for the d'Alembertian operator $\Box$ satisfies the wave equation for a delta-like source

$$\Box_x G(x^\sigma - y^\sigma) = \delta^{(4)}(x^\sigma - y^\sigma) \tag{2.58}$$

[14] $\bar{\bar{h}} = -h$, hence the name trace-reversed
[15] $\partial_\mu A^\mu = 0$ in Electromagnetism

Die approbierte gedruckte Originalversion dieser Diplomarbeit ist an der TU Wien Bibliothek verfügbar
The approved original version of this thesis is available in print at TU Wien Bibliothek.

Using the Green function, the general solution[16] of Equation 2.57 can be expressed as

$$\bar{h}_{\mu\nu} = -16\pi G \int G(x^\sigma - y^\sigma) T_{\mu\nu}(y^\sigma)\, d^4y \tag{2.59}$$

The solution to Equation 2.58 is the retarded Green function

$$G(x^\sigma - y^\sigma) = -\frac{1}{4\pi|\mathbf{x}-\mathbf{y}|}\delta(|\mathbf{x}-\mathbf{y}| - (x^0 - y^0))\theta(x^0 - y^0) \tag{2.60}$$

Substituting this into Equation 2.59 and using the delta function to integrate over y^0 yields

$$\bar{h}_{\mu\nu}(t, \mathbf{x}) = 4G \int \frac{1}{|\mathbf{x}-\mathbf{y}|} T_{\mu\nu}\left(t - |\mathbf{x}-\mathbf{y}|, \mathbf{y}\right)\, d^3y \tag{2.61}$$

This expression shows that the disturbance at time t and position $\mathbf{x}$ is influenced by the energy-momentum tensor at the retarded time $t_r = t - |\mathbf{x}-\mathbf{y}|$.

To proceed, we examine the problem in the frequency domain by applying a Fourier transform to the metric disturbance

$$\begin{aligned}
\tilde{h}_{\mu\nu}(\omega, \mathbf{x}) &= \frac{1}{\sqrt{2\pi}} \int dt\, e^{i\omega t} \bar{h}_{\mu\nu}(t, \mathbf{x}) \\
&= \frac{4G}{\sqrt{2\pi}} \int dt\, d^3y\, e^{i\omega t} \frac{T_{\mu\nu}(t - |\mathbf{x}-\mathbf{y}|, \mathbf{y})}{|\mathbf{x}-\mathbf{y}|} \\
&= \frac{4G}{\sqrt{2\pi}} \int dt_r\, d^3y\, e^{i\omega t_r} e^{i\omega|\mathbf{x}-\mathbf{y}|} \frac{T_{\mu\nu}(t_r, \mathbf{y})}{|\mathbf{x}-\mathbf{y}|} \\
&= 4G \int d^3y\, e^{i\omega|\mathbf{x}-\mathbf{y}|} \frac{\tilde{T}_{\mu\nu}(\omega, \mathbf{y})}{|\mathbf{x}-\mathbf{y}|}
\end{aligned} \tag{2.62}$$

In this derivation, the first line defines the Fourier transform, the second substitutes the solution from Equation 2.61, the third involves a change of variables, and the last applies the Fourier transform to $T_{\mu\nu}$.

To simplify the calculation of gravitational waves from a distant source, we make three key assumptions: the source is isolated, far from the observer, and moving slowly. This allows us to approximate the source as centered at a distance r from the observer, with each part of the source located at $r + \delta r$, where $\delta r \ll r$. This means the size of the source is small compared to the distance to the observer.

Since the source is slowly moving, the radiation it emits has relatively low frequencies ω such that the characteristic size of the source δr is much smaller than

[16] No factor $\sqrt{-g}$ is needed since the background is flat

Die approbierte gedruckte Originalversion dieser Diplomarbeit ist an der TU Wien Bibliothek verfügbar
The approved original version of this thesis is available in print at TU Wien Bibliothek.

the wavelength of the emitted waves ($\delta r \ll \omega^{-1}$). This allows us to treat the phase of the wave as nearly uniform across the source, as light propagates much faster than any internal motion within the source.

With these approximations, the term $e^{i\omega|\mathbf{x}-\mathbf{y}|}/|\mathbf{x}-\mathbf{y}|$, which describes the phase and amplitude of the wave as it travels from each point in the source to the observer, can be approximated by $e^{i\omega r}/r$ and taken outside the integral. This simplification yields

$$\tilde{h}_{\mu\nu}(\omega, \mathbf{x}) = 4G\frac{e^{i\omega r}}{r}\int d^3y\, \tilde{T}_{\mu\nu}(\omega, \mathbf{y}). \tag{2.63}$$

The Lorenz gauge in Fourier Space implies

$$\tilde{h}^{0\nu} = \frac{i}{\omega}\partial_i \tilde{h}^{i\nu} \tag{2.64}$$

Therefore, we only need to consider the spatial components and subsequently recover the timelike components using the relation meantioned before. We begin by setting $\nu = j$ to determine $\tilde{h}^{0j}$ from $\tilde{h}^{ij}$, which in turn allows us to find $\tilde{h}^{00}$ and $\tilde{h}^{ij}$. Starting from the integral in equation (2.63), we focus on the spacelike components. We proceed by performing integration by parts in reverse

$$\int d^3y\, \tilde{T}^{ij}(\omega, \mathbf{y}) = \int \partial_k \left(y^i \tilde{T}^{kj}\right) d^3y - \int y^i \left(\partial_k \tilde{T}^{kj}\right) d^3y. \tag{2.65}$$

The first term is a surface integral, which vanishes due to the source being isolated. The second term can be related to $\tilde{T}^{0j}$ using the Fourier-space version of the conservation law $\partial_\mu T^{\mu\nu} = 0$

$$-\partial_k \tilde{T}^{k\mu} = i\omega \tilde{T}^{0\mu}. \tag{2.66}$$

Thus,

$$\begin{aligned}
\int d^3y\, \tilde{T}^{ij}(\omega, \mathbf{y}) &= i\omega \int y^i \tilde{T}^{0j}\, d^3y \\
&= \frac{i\omega}{2}\int \left(y^i \tilde{T}^{0j} + y^j \tilde{T}^{0i}\right) d^3y \\
&= \frac{i\omega}{2}\int \left[\partial_l \left(y^i y^j \tilde{T}^{0l}\right) - y^i y^j \left(\partial_l \tilde{T}^{0l}\right)\right] d^3y \\
&= -\frac{\omega^2}{2}\int y^i y^j \tilde{T}^{00}\, d^3y.
\end{aligned} \tag{2.67}$$

The second line is justified by the symmetry of the left-hand side in the indices i and j. The third and fourth lines result from performing reverse integration by

Die approbierte gedruckte Originalversion dieser Diplomarbeit ist an der TU Wien Bibliothek verfügbar
The approved original version of this thesis is available in print at TU Wien Bibliothek.

parts and applying the conservation of $T^{\mu\nu}$.

Subsequently, we define the quadrupole moment tensor of the energy density of the source as follows:

$$I_{ij}(t) = \int y^i y^j T^{00}(t, \mathbf{y})\, d^3y. \tag{2.68}$$

Substituting this into 2.63 and transforming back to the time domain, we obtain the quadrupole formula:

$$\boxed{\bar{h}_{ij}(t, \mathbf{x}) = \frac{2G}{r} \frac{d^2 I_{ij}}{dt^2}(t_r)} \tag{2.69}$$

This formula indicates that the gravitational wave produced by an isolated, non-relativistic source is proportional to the second derivative of the quadrupole moment of the energy density, evaluated at the point where the past light cone of the observer intersects the source.

In electromagnetic radiation, the primary contribution typically arises from the variation of the dipole moment of the charge distribution. This distinction from gravitational radiation originates from the fundamental differences between electromagnetism and gravitation. Specifically, a changing dipole moment corresponds to motion in the center of the source's charge density for electromagnetism, or energy density in the case of gravitation. Unlike the charge distribution in electromagnetism, which can oscillate freely, the center of mass of an isolated gravitational system cannot oscillate without violating momentum conservation. In an isolated gravitational system, any movement in the center of mass would necessitate a compensating motion in the surrounding environment to conserve momentum.

Consequently, the quadrupole moment, which characterizes the shape or spatial distribution of the source, becomes the leading order term in gravitational radiation. Since the quadrupole moment is generally smaller than the dipole moment, gravitational radiation is inherently weaker than electromagnetic radiation. This difference is further amplified by the relatively weak coupling of matter to gravity, making gravitational radiation substantially weaker than its electromagnetic counterpart.

2.3. Multipole expansion and higher order modes

In the study of gravitational waves, the linearized gravity approximation provides a valuable starting point, especially for systems with weak gravitational fields and slow motion. In this linear framework, the quadrupole formula emerges as

Die approbierte gedruckte Originalversion dieser Diplomarbeit ist an der TU Wien Bibliothek verfügbar
The approved original version of this thesis is available in print at TU Wien Bibliothek.

a powerful result, capturing the dominant wave-generating mechanism for many astrophysical sources. However, the linear approximation only captures a fraction of the complexities involved in gravitational wave generation, particularly when internal gravitational fields are stronger or when relativistic effects become significant.

The limitations of the linear approximation manifest in its restriction to the quadrupole mode as the primary source of radiation, neglecting the contributions of higher-order modes. These higher-order modes become increasingly relevant in strong-field scenarios, such as the late inspiral and merger phases of binary black hole coalescences. In such regimes, the gravitational waves exhibit complex structures beyond the quadrupole mode, and capturing these additional modes is essential for accurately modeling the full waveform.

To extend beyond the limitations of linearized theory, one can use a full multipole expansion approach in general relativity, where Einstein's equations are solved without reducing the problem to a weak-field approximation. This method involves a systematic expansion of the gravitational field into multipole moments, effectively decomposing the field into terms associated with the mass and current distributions of the source. This approach accounts for the nonlinearities inherent in general relativity by including each "mass moment" and "current moment" up to arbitrarily high orders, with each moment contributing uniquely to the radiative structure of the gravitational waves. Consequently, higher-order modes naturally emerge from this expansion, enriching the waveform to reflect the full complexity of the source's dynamics.

A thorough treatment of the full formalism and technical intricacies involved in multipole expansions for gravitational radiation would go beyond the scope of this thesis. However, Kip Thorne has provided an outstanding and unified approach in his comprehensive 1980 review, which consolidates the various multipole formalisms and presents them in a cohesive notation [68].

An alternative to fully model complex relativistic systems is numerical relativity [7] [56], where the Einstein equations are solved numerically, allowing the simulation of the full, non-linear dynamics of gravitational waves. Numerical relativity is particularly valuable for modeling complex systems, such as binary black hole mergers, as it naturally includes all higher-order modes that arise from strong-field interactions.

Die approbierte gedruckte Originalversion dieser Diplomarbeit ist an der TU Wien Bibliothek verfügbar
The approved original version of this thesis is available in print at TU Wien Bibliothek.
TU Bibliothek Your knowledge hub WIEN

2.4. Sources of Gravitational Waves

As discussed in the previous sections, gravitational waves arise from the time-dependent multipole moments of mass distributions. For a system to produce strong gravitational-wave emission, several conditions are necessary: large masses, rapid motion, and intense gravitational fields. These factors influence the system's characteristic timescale, which ultimately determines the primary frequency band of gravitational-wave emission. In binary systems, the orbital frequency primarily governs the gravitational-wave frequency, while signal duration is defined by the rate of energy loss through gravitational radiation, leading to gradual orbital decay and, eventually, coalescence, at which point the gravitational-wave emission ends.

This section is based on the discussion provided in Gravitational-Wave Physics and Astronomy by Creighton and Anderson [29], which outlines the key principles and conditions for gravitational-wave emission in different astrophysical scenarios.

Gravitational-wave sources are often categorized by the frequency range in which they emit. Systems producing gravitational waves in the high-frequency range - typically between approximately 1 Hz and 10 kHz - fall within the detection range of ground-based observatories.

Another useful classification method is based on the nature of the dynamical processes involved, which imprint unique signatures on the gravitational-wave waveform.

The primary categories include:

- **Continuous-wave signals**: These signals are generated by sources exhibiting steady, periodic motion over long timescales, often exceeding the observational period. An example would be a rotating neutron star that as a non-axial deformation. Due to their frequency stability, continuous-wave signals are relatively well-modeled and can be identified through targeted searches.
- **Stochastic background**: Another type of continuous signal emerges from random, persistent processes in the universe, forming a gravitational-wave background analogous to the cosmic microwave background in the electromagnetic spectrum. This background is typically the incoherent sum of gravitational waves from countless independent sources. Although such signals persist beyond observational timescales, their stochastic nature complicates simple modeling, hence they are classified as a stochastic gravitational-wave background.

Die approbierte gedruckte Originalversion dieser Diplomarbeit ist an der TU Wien Bibliothek verfügbar
The approved original version of this thesis is available in print at TU Wien Bibliothek.
TU Bibliothek Your knowledge hub WIEN

- **Burst signals**: These are short-duration signals, where the emission duration[17] is shorter than the observational period.

Since gravitational-wave bursts were a central focus of this research, we will examine their nature in greater depth.

2.4.1. Gravitational Wave Bursts

Burst signals generally arise from violent events, including the coalescence of compact binaries, supernovae from stellar core-collapse, or other highly energetic, short-lived phenomena. For this research, the most relevant of these events are binary coalescences.

As mentioned earlier gravitational wave bursts resulting from binary inspiral and merger events are typically divided into three distinct phases: inspiral, merger, and ringdown. During the inspiral phase, the binary components orbit each other with relatively low velocities, allowing post-Newtonian (PN) methods to accurately model the gravitational radiation as the orbit decays due to energy loss from gravitational waves [15]. As the system progresses to the merger phase, the velocities become highly relativistic and the gravitational fields strong, rendering PN approximations insufficient and necessitating the use of numerical relativity to simulate the complex, non-linear dynamics of the collision [7] [56]. Following the merger, the resulting black hole undergoes the ringdown phase, where it settles into a stable state by emitting gravitational waves characterized by quasi-normal modes [44]. While these modeling techniques provide a robust framework for understanding gravitational wave bursts, they are limited by several factors. Post-Newtonian methods fail in the highly relativistic merger phase and cannot adequately account for tidal interactions or significant spin effects, especially in systems with misaligned angular momenta. Numerical relativity, although powerful, is computationally intensive and struggles with extreme mass ratio inspirals due to the vast difference in scales between the binary components.

[17] within the relevant frequency band

Die approbierte gedruckte Originalversion dieser Diplomarbeit ist an der TU Wien Bibliothek verfügbar
The approved original version of this thesis is available in print at TU Wien Bibliothek.

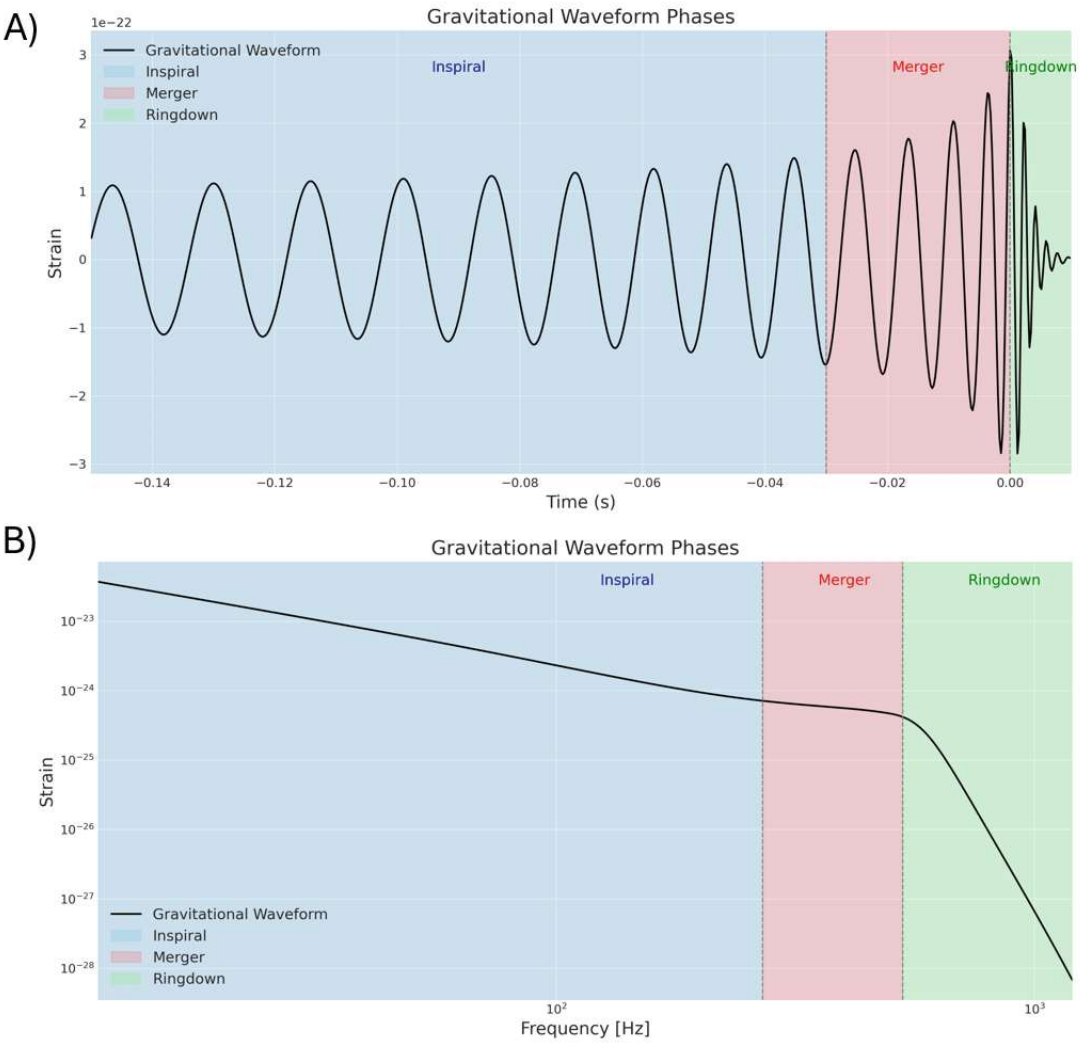

Figure 2.2.: Simulation of a Gravitational waveform, in the A) time domain B) frequency domain, depicting the inspiral, merger, and ringdown phases of a binary black hole coalescence. The waveform was generated using the IMRPhenomPv2 approximant with the following parameters: primary mass $m_1 = 20\,M_\odot$, secondary mass $m_2 = 10\,M_\odot$, non-spinning black holes ($\chi_1 = \chi_2 = 0$), and a luminosity distance of 1 Gpc. The shaded regions highlight each distinct phase **Inspiral** (light blue), **Merger** (light red), and **Ringdown** (light green). Vertical dashed lines indicate the boundaries between these phases, with the merger occurring at $t = 0$ seconds.

Die approbierte gedruckte Originalversion dieser Diplomarbeit ist an der TU Wien Bibliothek verfügbar
The approved original version of this thesis is available in print at TU Wien Bibliothek.

3. Gravitational Wave Detection

Gravitational waves are detected using specialized instruments, such as ground-based laser interferometers. These detectors, with kilometer-scale arms, are most sensitive in the frequency band of approximately 10 Hz to 1 kHz. In this chapter, we focus on these detectors, following the description in [29]. We begin by discussing the basic Michelson interferometer and proceed to more advanced versions, as illustrated in Figure 3.1.

3.1. Michelson Interferometer

A Michelson interferometer operates by splitting a laser beam into two orthogonal paths using a beam splitter. The two beams propagate towards mirrors placed at the ends of each arm, reflect back, and are recombined at the beam splitter, where they interfere. If the arms are of equal length[1], the returning light is entirely directed back toward the laser due to destructive interference in all other directions. Conversely, if the arm lengths differ by a non-integer multiple of the wavelength, the destructive interference away from the laser is incomplete, and light is captured by a photodiode.

The interferometer is typically configured such that no light reaches the photodiode in the absence of external perturbations. When a gravitational wave passes through the interferometer, it induces a strain[2] $h := \Delta l/l$, where $\Delta l := \Delta l_1 - \Delta l_2$ is the change in the arm length l. This strain alters the interference pattern, leading to a detectable signal at the photodiode. For a gravitational wave signal to be measurable, the induced change in arm length Δl must be comparable to the wavelength of the laser light, $\Delta l \approx \lambda_{\text{laser}}$.

To estimate the metric perturbation h detectable by a laser interferometer, we consider a simplified high-level calculation. Assume an infrared laser with a wavelength of approximately $\lambda_{\text{laser}} = 1\ \mu$m and detector arm lengths $l = 1$km. The

[1] Up to an integer multiple of the laser's wavelength.
[2] h is of the order of the metric perturbation.

Die approbierte gedruckte Originalversion dieser Diplomarbeit ist an der TU Wien Bibliothek verfügbar
The approved original version of this thesis is available in print at TU Wien Bibliothek.
TU Bibliothek Your knowledge hub WIEN

strain sensitivity can be expressed as

$$h := \frac{\Delta l}{l} \approx \frac{\lambda_{\text{laser}}}{l} \approx \frac{10^{-6}\ \text{m}}{10^{3}\ \text{m}} = 10^{-9} \tag{3.1}$$

This sensitivity, $h \approx 10^{-9}$, is far from sufficient to detect gravitational waves originating from black hole binaries, which typically induce metric perturbations on the order of $h \approx 10^{-20}$ or smaller. To bridge this gap, advanced techniques are required to enhance the sensitivity of ground-based interferometers.

One such method involves increasing the optical path length in the detector arms by incorporating optical cavities. These cavities allow the laser light to bounce multiple times, effectively increasing the arm length ℓ to an effective optical path ℓ_{eff}. However, when ℓ_{eff} approaches the gravitational wavelength λ_{GW}, given by $\lambda_{\text{GW}} \approx c/f_{\text{GW}}$, the sensitivity begins to degrade due to phase differences introduced by the gravitational wave.

Extending our calculation, targeting $f_{\text{GW}} \approx 300$ Hz implies $\lambda_{\text{GW}} \approx 1000$ km. Using multiple bounces, the strain sensitivity improves to:

$$h \approx \frac{\lambda_{\text{laser}}}{\lambda_{\text{GW}}} \approx \frac{10^{-6}\ \text{m}}{10^{6}\ \text{m}} = 10^{-12}. \tag{3.2}$$

While this represents a significant enhancement, it is still far from the required sensitivity of minimum $h \approx 10^{-20}$. Further improvements necessitate refining the measurement of the changes in the optical path lengths. Sensitive photodiodes play a crucial role in achieving this by enabling detection of changes much smaller than the laser wavelength λ_{laser}.

The primary challenge in this context is shot noise, which limits the precision of photon detection. Photon arrivals follow a Poisson process, resulting in natural fluctuations of order $\sqrt{N_{\text{photons}}}$. To detect a meaningful change in light intensity, the optical path difference must satisfy:

$$\Delta\ell \approx \frac{\sqrt{N_{\text{photons}}}}{N_{\text{photons}}}\lambda_{\text{laser}}. \tag{3.3}$$

The number of photons collected depends on the laser power P_{laser}, the photon energy $hc/\lambda_{\text{laser}}$, and the observation time τ, which is limited by the gravitational wave period $\tau \approx 1/f_{\text{GW}}$. Therefore

$$N_{\text{photons}} = \frac{P_{\text{laser}}\tau}{hc/\lambda_{\text{laser}}} = \frac{P_{\text{laser}}\lambda_{\text{laser}}}{hcf_{\text{GW}}}. \tag{3.4}$$

Die approbierte gedruckte Originalversion dieser Diplomarbeit ist an der TU Wien Bibliothek verfügbar
The approved original version of this thesis is available in print at TU Wien Bibliothek.
TU Bibliothek Your knowledge hub WIEN

For a typical setup with $P_{\text{laser}} = 1$ W, $\lambda_{\text{laser}} = 1$ μm, and $f_{\text{GW}} = 300$ Hz, we find $N_{\text{photons}} \approx 10^{16}$. The corresponding strain sensitivity is

$$h \approx \frac{\Delta\ell}{\ell_{\text{eff}}} \approx \frac{\sqrt{N_{\text{photons}}} \cdot \lambda_{\text{laser}}}{\lambda_{\text{GW}}} \approx \frac{10^{-8} \cdot 10^{-6}\ \text{m}}{10^{6}\ \text{m}} = 10^{-20}. \tag{3.5}$$

This level of sensitivity aligns with the strain amplitude h expected from astrophysical sources of gravitational waves.

To further improve sensitivity one can increase the laser power, which reduces shot noise. However, practical constraints on laser stability and power output are mitigated through power recycling. This technique reflects otherwise lost light back into the interferometer, boosting the circulating power by roughly one order of magnitude improvement in sensitivity. Beyond power recycling, advanced techniques such as signal recycling and quantum squeezing are employed to further optimize sensitivity, particularly in specific frequency bands critical for gravitational wave detection.

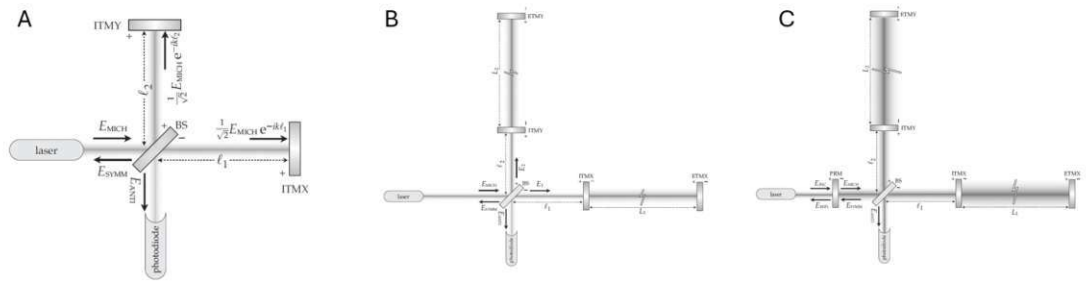

Figure 3.1.: Optical configurations of: A) Michelson Interferometer, B) Michelson Interferometer with Fabry-Perot cavities, and C) Michelson Interferometer with Fabry-Perot cavities and Power Recycling [29].

3.2. Detector Noise

As we have seen, the antisymmetric port of the power-recycled Fabry–Pérot Michelson interferometer is designed to remain dark when the light is resonant within the interferometer. However, imperfections and the necessity to measure minuscule changes in arm lengths introduce challenges that result in detectable signals at the antisymmetric port. These signals encompass contributions from gravitational-wave-induced strains as well as various noise sources that limit sensitivity. To assess the impact of these noise sources, it is essential to describe them in terms of amplitude spectral density and power spectral density. These metrics characterize

Die approbierte gedruckte Originalversion dieser Diplomarbeit ist an der TU Wien Bibliothek verfügbar
The approved original version of this thesis is available in print at TU Wien Bibliothek.

how noise power is distributed across different frequencies, enabling the identification of the detector's sensitivity to gravitational wave signals within specific frequency bands.

At the core of sensor noise are quantum effects, primarily shot noise and radiation pressure noise. Shot noise arises from the quantum fluctuations in the number of photons detected, constraining the precision of the interferometric measurements. Mitigating shot noise typically involves increasing the light power within the Fabry–Pérot cavities, thereby reducing shot noise at higher frequencies. However, this approach introduces radiation pressure noise, a low-frequency noise source resulting from fluctuations in the radiation field that exert forces on the test masses (mirrors). The radiation pressure force

$$F_{\text{rad}} = \frac{2I}{c}$$

where c is the speed of light and I is the power of the light hitting the mirror induces mirror position fluctuations which affect the overall sensor noise. The interplay between shot noise and radiation pressure noise defines the Standard Quantum Limit (SQL), a fundamental sensitivity benchmark rooted in quantum measurement theory and the Heisenberg uncertainty principle. The SQL represents the optimal balance between these two noise sources and depends on the interferometer's physical parameters, such as mirror mass M and arm length L.

Beyond quantum noise, environmental factors significantly impact detector sensitivity. Seismic noise, originating from ground motion due to natural and anthropogenic activities, for instance, trains passing near the LIGO Livingston detector contribute to low-frequency ground vibrations that can couple into the sensitive frequency band of the interferometer [31], primarily affects the detector at frequencies below approximately 40 Hz. Advanced seismic isolation systems, including pendulum suspensions and multi-layer mass-spring stacks, reduce this noise, achieving substantial suppression at higher frequencies where seismic noise would otherwise dominate.

Thermal noise, arising from the Brownian motion of mirror molecules and suspension systems, becomes the dominant noise source in the intermediate frequency range up to about 100 Hz. The fluctuation–dissipation theorem relates this noise to the material's internal losses, characterized by the loss angle ϕ. Cryogenic cooling and optimized suspension designs are crucial in minimizing thermal noise.

Gravity gradient noise, caused by density fluctuations in the ground and atmosphere, imposes additional low-frequency noise. While negligible in first-generation

Die approbierte gedruckte Originalversion dieser Diplomarbeit ist an der TU Wien Bibliothek verfügbar
The approved original version of this thesis is available in print at TU Wien Bibliothek.
TU Bibliothek Your knowledge hub WIEN

detectors, it becomes increasingly relevant in advanced and future interferometers due to improved seismic isolation. Mitigation strategies for gravity gradient noise may include subterranean installations and real-time compensation techniques based on local density measurements.

Together, these noise sources—quantum and environmental - define the sensitivity landscape of interferometric gravitational - wave detectors.

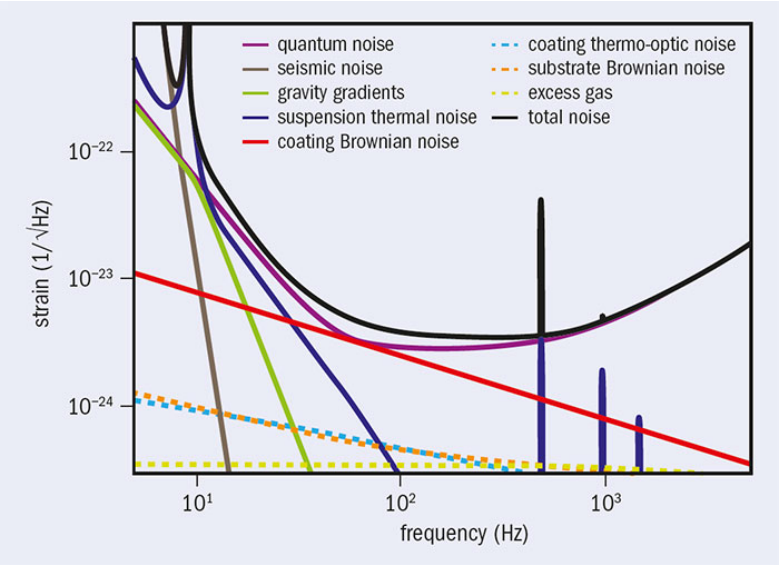

Figure 3.2.: The noise budget of advanced LIGO (aLIGO), illustrating the contributions of key noise sources to the total noise. Quantum noise, encompassing shot noise and radiation pressure noise, defines the high- and low-frequency limits of sensitivity, respectively. Environmental noise sources such as seismic noise, suspension thermal noise, and coating Brownian noise dominate in the low- to mid-frequency ranges. These noise curves highlight the challenges in achieving optimal detector sensitivity across different frequency bands [24].

3.3. Ground based Detectors

Ground-based gravitational wave detectors are currently the most important instruments in the field of gravitational wave detection. Among these detectors, the Laser Interferometer Gravitational-Wave Observatory (LIGO), Virgo, and KAGRA stand out as the most prominent and operational facilities.

Die approbierte gedruckte Originalversion dieser Diplomarbeit ist an der TU Wien Bibliothek verfügbar
The approved original version of this thesis is available in print at TU Wien Bibliothek.
TU Bibliothek Your knowledge hub WIEN

3.3.1. aLIGO (Advanced Laser Interferometer Gravitational Wave Detectors

aLIGO, operated by the National Science Foundation, comprises two geographically separated interferometers located in Hanford, Washington, and Livingston, Louisiana, in the United States. Each LIGO detector employs a Michelson interferometer configuration with two perpendicular arms, each extending 4 kilometers in length. The design integrates advanced laser systems, high-precision mirrors, and Fabry-Pérot cavities. Additionally, LIGO utilizes power recycling among other signal recycling techniques [67].

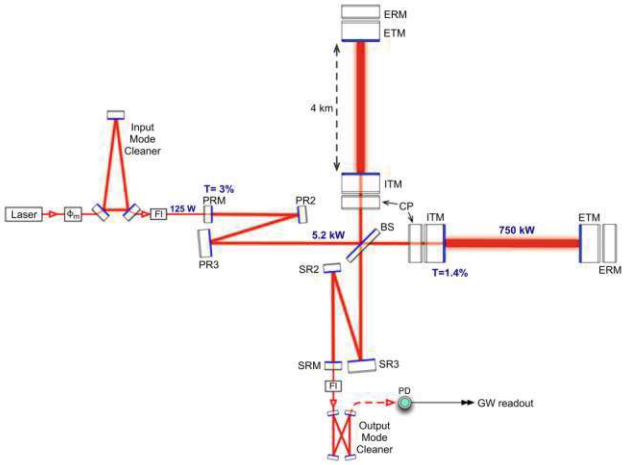

Figure 3.3.: Advanced LIGO optical layout: Laser light is recycled and amplified between mirrors (ITM, ETM) in a 4 km interferometer. Key components include beam splitter (BS), power recycling mirrors (PR2/PR3), and signal recycling mirrors (SR2/SR3) [67].

The significance of LIGO cannot be overstated, as it achieved a groundbreaking milestone in September 2015 with the first direct detection of gravitational waves (GW150914) emanating from a binary black hole merger [1]. This monumental discovery not only confirmed one prediction of Einstein's General Relativity but also inaugurated a new era in astrophysics. Since then, LIGO has consistently detected numerous gravitational wave events, including event GW190521 [27], where IMBHs had their first central stage.

3.3.2. Advanced Virgo (AdV)

Located in Cascina and operated by the Euopean Gravitational Wave Observatory, Italy, AdV is a key player in the global network of gravitational wave detectors.

Die approbierte gedruckte Originalversion dieser Diplomarbeit ist an der TU Wien Bibliothek verfügbar
The approved original version of this thesis is available in print at TU Wien Bibliothek.
TU Bibliothek Your knowledge hub WIEN

Similar to LIGO, Virgo employs a Michelson interferometer design, featuring two 3-kilometer-long arms. The detector utilizes advanced laser technology and high-precision mirrors within Fabry-Pérot cavities. Furthermore, Virgo incorporates sophisticated seismic isolation systems to minimize environmental noise [5] [6].

Virgo plays a critical role in the global gravitational wave detection network. Its strategic location in Europe, alongside LIGO's facilities in the United States, complements for superior localization of gravitational wave sources. Together they contributed to many first observations and the publication of three "catalog" papers [3] [26] [4]. A notable achievement of was its instrumental role in the first multi-messenger observation of a binary neutron star merger GW170817 in August 2017 [25], which was simultaneously detected in form of the gamma-ray burst GRB 170817A[34], measured by Fermi-GBM 1.7 seconds after the coalescence.

3.3.3. KAGRA

KAGRA, formerly known as the Large-scale Cryogenic Gravitational wave Telescope, and operated by the ministry of Education, Culture, Sports, Science and Technology-Japan, is the third detector within the Ligo-Virgo-Kagra collaboration (LVK). located in Kamioka, Gifu, Japan. Located in Kamioka, Gifu, Japan inside the Mt. Ikenoyama mine, KAGRA features a Michelson interferometer with two 3-kilometer-long arms arranged in an L-shape. Distinguished as a 2.5 generation GW detector, KAGRA incorporates unique technological advancements such as underground construction and cryogenic operation of sapphire mirrors.

Operational since 2019, KAGRA is the first major gravitational wave detector built underground and the first to utilize cryogenic mirror cooling, which are key technologies of the third generation large scale detectors. These innovations position KAGRA as a pioneering facility in the field, enhancing the global gravitational wave network's sensitivity and sky coverage. KAGRA's integration into the LVK collaboration strengthens the LVK network's ability to detect and precisely localize gravitational wave sources.

Die approbierte gedruckte Originalversion dieser Diplomarbeit ist an der TU Wien Bibliothek verfügbar
The approved original version of this thesis is available in print at TU Wien Bibliothek.
TU Bibliothek Your knowledge hub WIEN

Figure 3.4.: Overhead view of the underground KAGRA gravitational wave observatory, featuring 3 km-long arms forming an L-shaped tunnel [40].

3.3.4. The LVK Collaboration (LIGO-Virgo-KAGRA)

The LVK collaboration represents a unified international effort among the LIGO, Virgo, and KAGRA detectors to enhance the detection and analysis of gravitational wave events. This set of detectors uses the unique strengths and capabilities of each detector to form a highly sensitive and geographically dispersed network. This significantly improves the overall performance and scientific output of gravitational wave astronomy.

The detectors operate in observing runs (denoted as O1, O2, O3, etc.), alternating with periods of no data collection. During these non-operational periods, known as commissioning phases, the detectors undergo maintenance, upgrades, and calibration to improve their sensitivity and reliability [2]. Observing runs are the active data-gathering phases, typically lasting several months to over a year, during which all participating detectors are synchronized to maximize the detection of gravitational waves. The current and planned states of operation can be seen in 3.6. Their respective PSD per observation run can be seen in

Die approbierte gedruckte Originalversion dieser Diplomarbeit ist an der TU Wien Bibliothek verfügbar
The approved original version of this thesis is available in print at TU Wien Bibliothek.
TU Bibliothek Your knowledge hub WIEN

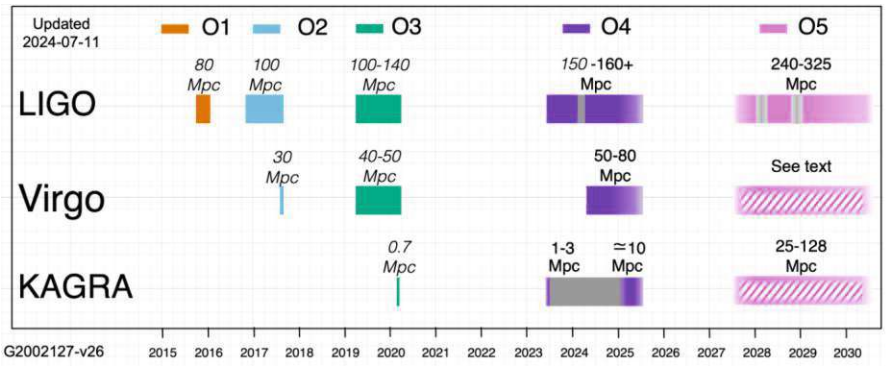

Figure 3.5.: Timeline of observing runs and sensitivity ranges for the LIGO, Virgo, and KAGRA detectors. The figure shows the progression of observing runs O1 through O5, with corresponding binary mergers, detection ranges in megaparsecs (Mpc). Sensitivity improvements are indicated for each detector: LIGO reaching up to 160+ Mpc in O4 and projected 240–325 Mpc in O5, Virgo achieving up to 80 Mpc in O4, and KAGRA improving from 1–3 Mpc in O4 to a projected range of 25–128 Mpc in O5 [52].

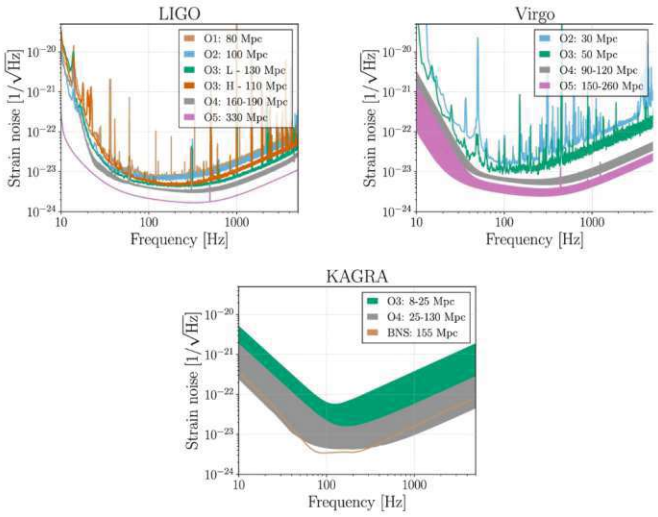

Figure 3.6.: Strain sensitivity curves for LIGO (top left), Virgo (top right), and KAGRA (bottom) during observing runs. Sensitivity improvements over time are shown, with corresponding binary neutron star (BNS) detection ranges in megaparsecs (Mpc). Projected sensitivities for future runs (O4 and O5) indicate significant advancements in detection capabilities [2].

Die approbierte gedruckte Originalversion dieser Diplomarbeit ist an der TU Wien Bibliothek verfügbar
The approved original version of this thesis is available in print at TU Wien Bibliothek.

3.3.5. Future Expansion of the LVK Collaboration

Einstein Telescope

The Einstein Telescope (ET) is the European initiative for a third-generation gravitational wave (GW) detector, designed to significantly advance GW astronomy by detecting sources throughout cosmic history, including those from the early Universe. ET's reference configuration features a triangular geometry composed of three nested detectors, each with 10-kilometer-long arms, and employs a "xylophone" setup that integrates interferometers optimized for both high and low frequencies, operating at cryogenic temperatures. Furthermore is will be positioned 200-300 meters underground to mitigate seismic noise. This design enhances sensitivity by an order of magnitude compared to second-generation detectors like Advanced LIGO and Advanced Virgo, and broadens the detectable frequency range. In figure 3.7 one can see the optical layout proposed for the ET [16].

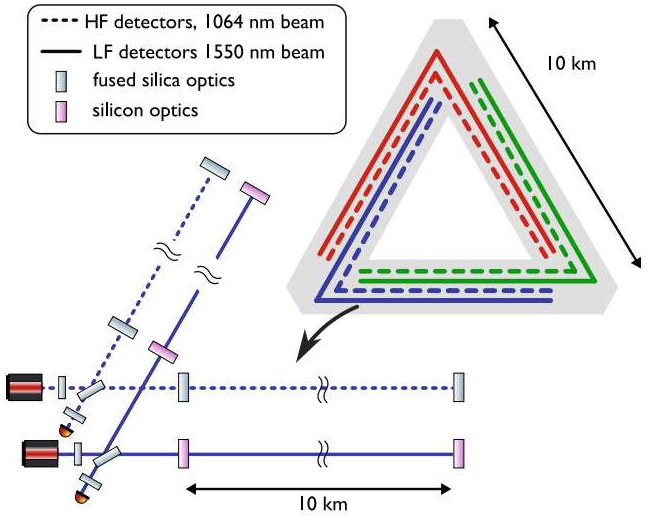

Figure 3.7.: General overview of the Einstein Telescope (ET) layout, featuring three detectors arranged in a 10 km equilateral triangle. Bottom left: Each detector consists of two interferometers, optimized for high frequencies (HF) and low frequencies (LF). The core design is based on a Michelson interferometer with Fabry-Perot cavities in the arms and recycling techniques [60].

Laser Interferometer Space Antenna (LISA)

While the focus of this section is on ground-based detectors, it is essential to acknowledge the complementary role of space-based observatories like LISA. Op-

Die approbierte gedruckte Originalversion dieser Diplomarbeit ist an der TU Wien Bibliothek verfügbar
The approved original version of this thesis is available in print at TU Wien Bibliothek.

erating in the low-frequency range between 0.1 mHz and 1 Hz, LISA targets gravitational waves with much longer wavelengths compared to those detectable by ground-based instruments. This distinct frequency range allows LISA to observe a different set of gravitational wave sources, including ultra-compact binaries within our Galaxy, mergers of supermassive black holes, and extreme mass ratio inspirals.

LISA consists of three spacecraft forming an equilateral triangle with arm lengths of approximately one million miles. Positioned in space, LISA avoids terrestrial noise and leverages its extensive arm lengths to access regions of the gravitational wave spectrum that are inaccessible from Earth. By covering a broader frequency spectrum, LISA significantly broadens the detection landscape, enabling the exploration of a wider variety of astrophysical phenomena and providing invaluable data that complements the observations made by ground-based detectors within the global gravitational wave network [51].

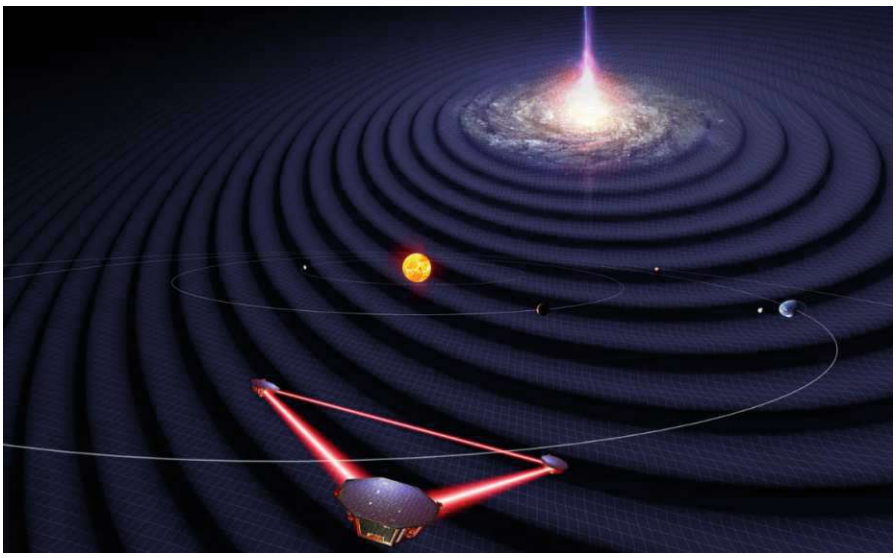

Figure 3.8.: A schematic illustration of LISA within the solar system. (Created by Simon Barke, University of Florida. Licensed under CC BY 4.0. Source: `https://news.ufl.edu/2024/02/uf-contributes-to-lisa-mission/`

Other Detector projects

LIGO-India is a joint initiative between the U.S. National Science Foundation's LIGO Laboratory and three prominent Indian institutions: the Raja Ramanna Center for Advanced Technology in Indore, the Institute for Plasma Research in Ahmedabad, and the Inter-University Centre for Astronomy and Astrophysics in

Die approbierte gedruckte Originalversion dieser Diplomarbeit ist an der TU Wien Bibliothek verfügbar
The approved original version of this thesis is available in print at TU Wien Bibliothek.
TU Bibliothek Your knowledge hub WIEN

Pune. This collaboration aims to enhance the network's geographical diversity, thereby improving source localization and polarization measurement capabilities, which are crucial for accurate gravitational wave astronomy [46].

Cosmic Explorer, the United States' contribution to the next-generation observatory network, features two L-shaped interferometers with 40-kilometer and 20-kilometer arms, respectively. It is designed to achieve an order of magnitude increase in sensitivity over current detectors, which will enable the detection of a vastly greater number of gravitational wave events with significant precision, including those from intermediate-mass black hole mergers [28].

Die approbierte gedruckte Originalversion dieser Diplomarbeit ist an der TU Wien Bibliothek verfügbar
The approved original version of this thesis is available in print at TU Wien Bibliothek.

4. Data Analysis

Gravitational-wave (GW) astronomy has opened a new window into the cosmos, enabling the observation of phenomena that are otherwise invisible through electromagnetic means. However, detecting and interpreting GW signals poses significant challenges due to their inherently weak nature and the presence of substantial noise within the detectors. This section follows the review of [29] and outlines the fundamental principles of GW data analysis, focusing on the characterization of detector noise, the concept of power spectral density, and the two pivotal techniques of matched filtering and Bayesian parameter estimation. These methodologies are essential for optimizing the extraction of GW signals from noisy data and for accurately determining the properties of their astrophysical sources.

4.1. Fundamentals of Detector Noise

Ligo and Virgo, is limited by various noise sources that obscure the faint GW signals. Detector noise is often modeled as Gaussian because many independent noise contributions - such as thermal noise, seismic noise, and quantum noise - combine according to the Central Limit Theorem, resulting in a Gaussian distribution. This assumption is only valid when the noise is the sum of a large number of small, independent disturbances, each contributing minimally to the overall noise. This approach greatly simplifys the analysis.

Modeling detector noise as Gaussian implies that the noise is fully described by its first two moments: the mean (typically zero) and the covariance (or power spectral density). This property facilitates the use of linear filtering techniques, such as matched filtering, which are optimal for maximizing the signal-to-noise ratio (SNR) in the presence of Gaussian noise. Additionally, Gaussian noise allows for the derivation of analytical expressions for the probability of false alarms and detection efficiencies, which are crucial for assessing the reliability of GW detections.

Die approbierte gedruckte Originalversion dieser Diplomarbeit ist an der TU Wien Bibliothek verfügbar
The approved original version of this thesis is available in print at TU Wien Bibliothek.
TU Bibliothek Your knowledge hub WIEN

4.1.1. Power Spectral Density (PSD)

The power spectral density (PSD) is a fundamental concept in GW data analysis, quantifying how the power of a signal or noise is distributed across different frequency components.

For a stationary random process $x(t)$, the power spectral density (PSD) $S_x(f)$ is defined as the Fourier transform of its autocorrelation function $R_x(\tau)$:

$$S_x(f) = 2 \int_0^\infty R_x(\tau) e^{-2\pi i f \tau} \, d\tau \tag{4.1}$$

The PSD provides a frequency-dependent measure of the noise power, enabling the characterization of noise properties across the detector's sensitive band. Understanding the PSD is crucial for designing filters that can effectively distinguish GW signals from noise by emphasizing frequency ranges where the detector is most sensitive as we will see later.

4.2. Matched Filtering

Matched filtering is the currently most relevant technique for detecting GW signals within noisy data. It leverages the known or hypothesized waveform shapes of potential GW sources to maximize the SNR, thereby enhancing the probability of signal detection. It involves correlating the detector data $s(t)$, which may contain both noise $n(t)$ and a potential gravitational wave (GW) signal $h(t)$, with a set of theoretical waveform templates $h(\lambda)$ parameterized by λ:

$$s(t) = n(t) + h(t; \lambda) \tag{4.2}$$

The goal is to compute the inner product between the data and each template, weighted by the inverse of the PSD $S_n(f)$:

$$(s, h) = 4 \, \mathrm{Re} \int_0^\infty \frac{\tilde{s}(f) \tilde{h}^*(f)}{S_n(f)} \, df \tag{4.3}$$

where $\tilde{s}(f)$ and $\tilde{h}(f)$ are the Fourier transforms of $s(t)$ and $h(t)$, respectively. This inner product, known as the matched filter output, effectively measures the overlap between the data and the template, scaled by the noise characteristics.

In the absence of a gravitational wave (GW) signal ($h(t; \lambda) = 0$), the matched filter output is a Gaussian random variable with zero mean and variance $\sigma^2 = (h, h)$. When a signal is present, the output becomes a Gaussian random variable with

Die approbierte gedruckte Originalversion dieser Diplomarbeit ist an der TU Wien Bibliothek verfügbar
The approved original version of this thesis is available in print at TU Wien Bibliothek.

mean $A\sigma^2$ (where A is the signal amplitude) and the same variance σ^2. The signal-to-noise ratio (SNR) ρ is defined as

$$\rho = \frac{(s,h)}{\sigma} \tag{4.4}$$

A higher SNR indicates a more significant detection, as the probability of false alarms decreases exponentially with increasing ρ.

To detect a signal, a discrete collection of templates is used to cover the relevant parameter space. A dense template bank ensures that any real signal closely aligns with at least one template, reducing the loss of SNR caused by parameter mismatches. The matched filter then systematically analyzes the data, comparing it against each template to find the best match, ultimately identifying potential gravitational wave signals based on the highest overlap with the data.

4.3. Baysian Parameter Estimation

Once a GW signal is detected, the next critical step is to accurately estimate the parameters that characterize the source of the signal. Bayesian parameter estimation provides a comprehensive framework for inferring the posterior probability distributions of these parameters, integrating both the observed data and prior knowledge.

Bayesian parameter estimation relies on Bayes' theorem, which relates the posterior probability $P(\lambda \mid s)$ of the parameters λ given the data s to the likelihood $P(s \mid \lambda)$ and the prior $P(\lambda)$

$$P(\lambda \mid s) = \frac{P(s \mid \lambda)P(\lambda)}{P(s)} \tag{4.5}$$

Here, $P(s)$ is the evidence, which acts as a normalizing factor. In the context of gravitational wave (GW) data analysis, λ typically includes intrinsic parameters, such as the masses and spins of the binary components, as well as extrinsic parameters like the distance and orientation of the source.

The posterior probability distribution $P(\lambda \mid s)$ provides a complete statistical description of the uncertainties in the estimated parameters. The peak of this distribution, often referred to as the maximum a posteriori (MAP) estimate, corresponds to the most probable set of parameters given the data and prior information.

Die approbierte gedruckte Originalversion dieser Diplomarbeit ist an der TU Wien Bibliothek verfügbar
The approved original version of this thesis is available in print at TU Wien Bibliothek.

When assuming Gaussian noise, the likelihood function is given by:

$$P(s \mid \lambda) \propto \exp\left(-\frac{1}{2}(s - h(\lambda), s - h(\lambda))\right) \tag{4.6}$$

where $h(\lambda)$ is the gravitational wave waveform model dependent on the parameters λ, and $(\cdot, \cdot)$ denotes the noise-weighted inner product. This formulation encapsulates how well the waveform $h(\lambda)$ matches the observed data $s(t)$ within the noise characteristics.

Accurate parameter estimation highly depends on the waveform models used. Systematic errors arise when there are discrepancies between the true GW signal and the modeled waveforms.

4.4. Nested Sampling

While Bayesian parameter estimation provides a powerful framework for inferring the posterior distributions of GW source parameters, the computational complexity of calculating a high dimensional posterior distribution posses some challenges.

Nested Sampling, introduced by John Skilling in 2004 [64], is a computational algorithm designed to efficiently compute the Bayesian evidence[1]

$$P(s) = \int P(s \mid \lambda) P(\lambda) d\lambda \tag{4.7}$$

while simultaneously generating samples from the posterior distribution.

It operates by iteratively exploring regions of parameter space with increasing likelihood, effectively "nesting" the search within higher likelihood contours. The algorithm maintains a set of active points [2] that sample the prior distribution under the constraint of increasing likelihood. At each iteration, the point with the lowest likelihood is replaced with a new sample drawn from the prior, constrained to have a higher likelihood than the discarded point. This process continues, progressively narrowing down the parameter space to regions of higher posterior probability.

[1] or marginal likelihood
[2] live points

Die approbierte gedruckte Originalversion dieser Diplomarbeit ist an der TU Wien Bibliothek verfügbar
The approved original version of this thesis is available in print at TU Wien Bibliothek.

4.4.1. Step-by-Step Algorithm

1. **Initialization**
   a) Select Number of Live Points (N): Choose a set number of active samples (live points) to explore the parameter space. The choice of N balances computational efficiency with the accuracy of the evidence estimate.
   b) Sample Initial Live Points: Draw N independent samples $\{\lambda_1, \lambda_2, \ldots, \lambda_N\}$ from the prior distribution $P(\lambda)$.
   c) Define the Likelihood function L
   d) Initialize the prior volume X_0 to 1, representing the entire parameter space
   e) Initialize the evidence $P_0(s)$ to zero
2. **Iterative Sampling** (For each iteration i):
   a) Identify the Lowest Likelihood Live Point:

$$\theta_{\min} = \arg\min\{L(\lambda_1), L(\lambda_2), \ldots, L(\lambda_N)\}, \tag{4.8}$$

   b) Estimate Prior Volume Shrinkage (ΔX_i):

$$\Delta X_i = X_{i-1} t_i, \quad \text{where} \quad t_i \approx e^{-1/N} \quad [3] \tag{4.9}$$

   c) Accumulate Evidence:

$$P(s) \approx P(s) + L_{\min} \Delta X_i. \tag{4.10}$$

   d) Replace the Discarded Live Point: Draw a new sample λ_{new} from the prior $P(\lambda)$ subject to the constraint:

$$P(s \mid \lambda_{\text{new}}) > L_{\min}. \tag{4.11}$$

   Add λ_{new} to the set of live points, maintaining the number of live points N.
   e) Update Prior Volume:

$$X_i = X_{i-1} - \Delta X_i. \tag{4.12}$$

[3] t_i is inherently a random variable because the shrinkage depends on the specific realization of live points and their likelihoods, but the expected shrinkage in each iteration is on average $e^{-1/N}$.

Die approbierte gedruckte Originalversion dieser Diplomarbeit ist an der TU Wien Bibliothek verfügbar
The approved original version of this thesis is available in print at TU Wien Bibliothek.

3. **Termination**

   The algorithm continues iterating until either the estimated remaining evidence from the live points falls below a predefined threshold ϵ, ensuring that the majority of the evidence has been accounted for or a number of iterations were made or a certain number of iterations were made.

4. **Posterior Sampling**

   Throughout the iterative process, the discarded points λ_{min} and their associated weights ΔX_i form a representative sample of the posterior distribution $P(\lambda \mid s)$.

Die approbierte gedruckte Originalversion dieser Diplomarbeit ist an der TU Wien Bibliothek verfügbar
The approved original version of this thesis is available in print at TU Wien Bibliothek.

5. Gravitational Wave Burst Simulations

Simulating gravitational wave bursts is crucial for detecting and interpreting signals from events like binary black hole mergers, neutron star collisions, and supernovae. This chapter focuses on the methodologies for simulating these bursts, the limitations of pure numerical relativity, and the practical use of surrogate and phenomenological models as efficient alternatives, with key examples highlighted.

5.1. Methodologies for Simulating Gravitational Wave Bursts

5.1.1. Numerical Relativity

Numerical Relativity involves discretizing Einstein's equations on a computational grid and evolving them over time to simulate the merger and ringdown phases of compact binary systems. This approach captures the full nonlinear dynamics of spacetime, including effects like gravitational wave emission, black hole horizons, and matter interactions in neutron star mergers.

NR provides the most accurate waveforms available, capturing all nonlinear and complex interactions during the merger process including higher order modes. This high fidelity is crucial for:

- Validating and calibrating approximate waveform models.
- Accurately modeling the late inspiral, merger, and ringdown phases where analytical approximations break down.

Currently NR simulations are computationally expensive, often requiring supercomputers with extensive computational resources and weeks of computation time for a single simulation. This high computational cost limits the number of simulations that can be feasibly performed, restricting coverage of the vast parameter space of compact binary systems. Therefore scaling NR to cover extensive

Die approbierte gedruckte Originalversion dieser Diplomarbeit ist an der TU Wien Bibliothek verfügbar
The approved original version of this thesis is available in print at TU Wien Bibliothek.
TU Bibliothek Your knowledge hub WIEN

populations or to perform real-time analyses is impractical. The prohibitive computational demands makes it unsuitable for real-time GW detection and parameter estimation or large-scale population studies requiring thousands to millions of waveforms.

5.1.2. NRSur7dq4: A Surrogate Model for Gravitational Waveforms

Surrogate models have emerged as a powerful tool to bridge the gap between the high accuracy of Numerical Relativity and the computational efficiency required for large-scale gravitational wave data analysis. `NRSur7dq4` [69] is a prominent surrogate model that enables rapid and accurate waveform generation for precessing binary black hole systems.

Surrogate models like `NRSur7dq4` are constructed using a systematic process to combine the accuracy of Numerical Relativity simulations with computational efficiency. The process begins with generating a dataset of NR waveforms by solving Einstein's equations for a representative set of parameters, such as mass ratios and spin vectors, within the target parameter space. The resulting waveforms are then decomposed into simpler components using techniques such as singular value decomposition. These components are parameterized and interpolated using empirical methods to create a surrogate model capable of generating waveforms for arbitrary parameter values within the training range. Once developed, `NRSur7dq4` generates waveforms with similar accuracy to direct NR simulations but at speeds orders of magnitude faster, effectively addressing the computational limitations of numerical relativity [13].

However, `NRSur7dq4` is constrained to the parameter ranges covered by its underlying NR simulations, and extrapolations beyond these ranges can lead to inaccuracies. While the model provides significant efficiency gains for waveform generation, its initial development requires a substantial investment in NR simulations and computational resources, making the creation and extension of such models resource-intensive.

5.1.3. IMRPhenomPv2: A Phenomenological Waveform Model

Phenomenological waveform models play a crucial role in gravitational wave data analysis by providing computationally efficient approximations to the complex waveforms predicted by Numerical Relativity. `IMRPhenomPv2` is a widely used

Die approbierte gedruckte Originalversion dieser Diplomarbeit ist an der TU Wien Bibliothek verfügbar
The approved original version of this thesis is available in print at TU Wien Bibliothek.

within the community as a state of the art phenomenological waveform model that incorporates spin precession effects, making it suitable for analyzing signals from precessing binary black hole systems.

`IMRPhenomPv2` is constructed by fitting analytical expressions to NR simulations, capturing the essential features of GW signals from compact binary mergers. The model spans the inspiral, merger, and ringdown phases of the waveform, integrating spin precession to account for the dynamics of systems with misaligned spins.

The development of `IMRPhenomPv2` involves:

1. **Inspiral Modeling**: Utilizing post-Newtonian approximations to model the early inspiral phase where the binary components are well-separated.
2. **Merger and Ringdown Fitting**: Employing NR simulations to fit the waveform during the highly nonlinear merger and subsequent ringdown phases.
3. **Spin Precession Incorporation**: Incorporating the effects of spin precession by modeling the waveform in a co-precessing frame and then transforming it to the inertial frame.

`IMRPhenomPv2` is designed to generate waveforms rapidly even faster than the surrogate models, making it also suitable for the points numerical relativity was missing.

Phenomenological models are designed to be accurate, but they rely on approximations that can miss subtle nonlinear effects captured by numerical relativity (NR) or lead to errors in parts of the parameter space that aren't well-represented by the fitting process.

`IMRPhenomPv2` is extensively utilized in GW data analysis pipelines for Matched-filtering searches to detect BBH mergers, Bayesian parameter estimation to infer the physical properties of detected GW events or Multi-messenger astronomy, where rapid waveform generation is essential for coordinating electromagnetic follow-ups [41].

5.1.4. Efficient Waveform Generation with PyCBC and GWSurrogate

The advent of sophisticated software libraries has significantly streamlined the process of gravitational wave waveform generation, enabling researchers to produce complex waveforms with minimal computational effort. Libraries such as

Die approbierte gedruckte Originalversion dieser Diplomarbeit ist an der TU Wien Bibliothek verfügbar
The approved original version of this thesis is available in print at TU Wien Bibliothek.
TU Bibliothek Your knowledge hub WIEN

PyCBC [53] and GWSurrogate [14] provide user-friendly interfaces that facilitate the rapid generation of waveforms using state-of-the-art models like NRSur7dq4 and IMRPhenomPv2.

Waveforms from various models can be easily generated with PyCBC. For instance, the IMRPhenomPv2 model can be used with the following command

```
from pycbc.waveform import get_td_waveform
hp, hc = get_td_waveform(
    approximant="IMRPhenomPv2",
    mass1=20,
    mass2=10,
    dist_mpc=5000,
    f_lower = 10,
    delta_t=1/4069
)
```

Generating waveforms with GWSurrogate requires first downloading the desired surrogate model and specifying its path, but the process remains simple. Once the surrogate is available, waveforms can be generated with the following command

```
import gwsurrogate
sur = gwsurrogate.LoadSurrogate('NRSur7dq4')
t, h_full, dyn = sur(
    q=1.2,
    M=200,
    dist_mpc=5000,
    chiA0=[0,0,0],
    chiB0=[0,0,0],
    units="mks",
    f_low=10
)
```


Die approbierte gedruckte Originalversion dieser Diplomarbeit ist an der TU Wien Bibliothek verfügbar
The approved original version of this thesis is available in print at TU Wien Bibliothek.

6. Research

Sophisticated online pipelines developed by the LIGO, Virgo, and KAGRA collaborations play a crucial role in the real-time detection and analysis of gravitational waves. These systems enable rapid identification of GW events, timely alerts for multi-messenger astronomy, and in-depth astrophysical studies of the universe's most extreme phenomena.

The online search pipelines used by these collaborations are broadly categorized into modeled and unmodeled searches, each designed to detect distinct classes of GW signals. Modeled searches, also known as Compact Binary Coalescence (CBC) searches, specifically target signals originating from the mergers of compact binary systems, including binary neutron stars, neutron star black hole binaries , and binary black holes. These searches utilize matched-filtering techniques, employing discrete banks of waveform templates that encapsulate the expected signal characteristics of these mergers. Prominent examples of modeled pipelines include PyCBC Live [17] [54] and GstLAL [8].

Conversely, unmodeled searches, commonly referred to as Burst searches, are engineered to detect a broader spectrum of GW signals without relying on specific waveform models. This versatility allows them to identify signals from a variety of astrophysical sources beyond compact binary mergers, including the core-collapse of massive stars, magnetar star-quakes, and more speculative origins like intersecting cosmic strings or other yet-to-be-discovered GW sources. Notable examples of unmodeled pipelines include cWB [42] [43], oLIB[47], and MLy ("Emily") [63], each employing distinct methodologies to reconstruct and identify transient GW signals across multiple detectors [37].

Central to the efficacy of modeled searches is the construction and utilization of template banks. These banks consist of waveform templates generated using specific approximants, which are mathematical models that approximate the true GW signals produced by compact binary mergers. The choice of approximant is important, as waveforms produced by different approximants, even when based on identical physical parameters, can exhibit significant discrepancies. Such differences can lead to residuals differences between the actual GW signal and the closest matching template - that are substantial enough to mimic or be mistaken

Die approbierte gedruckte Originalversion dieser Diplomarbeit ist an der TU Wien Bibliothek verfügbar
The approved original version of this thesis is available in print at TU Wien Bibliothek.
TU Bibliothek Your knowledge hub WIEN

for genuine GW signals. For instance, a residual from a mismatched approximant might be as large as another independent GW event, potentially leading to false detections or missed signals as seen in 6.1.

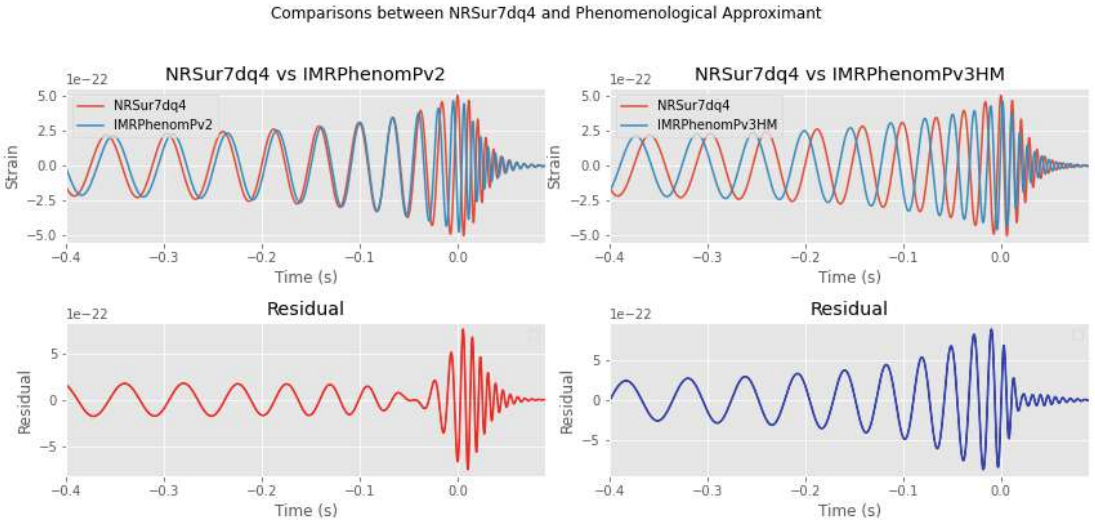

Figure 6.1.: Comparison of waveforms and residuals between surrogate model NRSur7dq4 and phenomenological approximants with equal parameters. Top panels show the strain waveforms for NRSur7dq4 against IMRPhenomPv2 (left) and IMRPhenomPv3HM (right). Bottom panels display the corresponding residuals.

Therefore template banks must be dense enough to ensure that for most of GW signals, there exists a template closely matching its waveform. This density prevents the loss of detections due to the absence of a suitably similar template within the bank. Additionally, the inherent limitations of waveform approximants introduce the possibility that a GW signal may be matched to a template with parameters that do not precisely reflect the true source characteristics. This phenomenon arises from the approximations and simplifications embedded within the waveform models, which may omit certain physical effects or fail to capture complex dynamics accurately. Consequently, a signal may be erroneously associated with a template possessing different parameters.

Following the detection of a gravitational wave (GW) signal, parameter estimation is essential for uncovering the physical properties of the source. This process typically relies on Bayesian parameter estimation techniques, which combine prior knowledge with observational data to derive posterior distributions for the source parameters. A leading pipeline for this purpose is Bilby [10]. For all detected

Die approbierte gedruckte Originalversion dieser Diplomarbeit ist an der TU Wien Bibliothek verfügbar
The approved original version of this thesis is available in print at TU Wien Bibliothek.

events, an automated Bilby analysis is conducted, where the choice of approximant depends on the initial chirp mass estimate provided by the search pipeline. Notably, all approximants used in this analysis are phenomenological models [38].

The result of Bayesian parameter estimation is dependent on the accurate specification of both priors and waveform models (approximants) used in the analysis. The selection of an inappropriate waveform model can potentially introduce biases in the estimated parameters, skewing the properties of the event. Similarly, poorly chosen priors can compound these biases, particularly if the priors. For example, utilizing a phenomenological waveform model that lacks higher-order modes, as opposed to a more accurate surrogate model that incorporates these modes, can result in systematic biases in parameter estimation. Such biases could be particularly pronounced in the context of intermediate mass black holes, where the omission of higher-order modes can significantly distort the inferred properties. This poses substantial challenges for accurately characterizing IMBHs, necessitating a focused investigation into the interplay between waveform approximants and parameter estimation accuracy.

This chapter explores the gravitational waves generated by intermediate mass black hole mergers, with a particular emphasis on higher-order modes. We begin by introducing the characteristics of higher order modes in IMBHs. Through visual inspections and the development of the relative power measure, we quantify the impact of higher order modes in waveforms across different parameters. Finally, we assess the impact of Approximant choice in parameter estimation accuracy, highlighting potential biases and their implications for future gravitational wave astronomy.

6.1. Visual Inspection of Gravitational Waves from IMBHs

In order to get a feeling of the impact and size of higher-order modes, it is useful to first visually analyze the decomposition of these waveforms. This visual inspection allows us to observe how different physical parameters, such as mass ratio, spin, and inclination angle, influence the gravitational waveforms emitted by intermediate mass black hole mergers. By breaking down the waveforms into their individual modes and examining them graphically, we can identify patterns, trends, and unique features.

Die approbierte gedruckte Originalversion dieser Diplomarbeit ist an der TU Wien Bibliothek verfügbar
The approved original version of this thesis is available in print at TU Wien Bibliothek.
TU Bibliothek Your knowledge hub WIEN

6.1.1. Methodology

The waveforms analyzed in this visual study are generated using the `GWsurrogate` library, which provides a convenient interface for simulating gravitational waveforms. For waveform generation, we employ the approximant `NRSUR7dq4`. As discussed in 5.1.2, this approximant is based on numerical relativity, ensuring that the generated waveforms naturally include higher-order modes. Unlike phenomenological models that may require additional techniques to incorporate these modes, `NRSur7dq4` provides built-in support for higher-order modes up to $\ell = 4$. This eliminates the need for any specialized methods to extract or compute the higher-order contributions.

Once the gravitational waveform for a given set of parameters is generated, it is output as a complex-valued superposition of the plus and cross polarizations, given by $h = h_\times - ih_+$. Since only real-valued functions can be directly plotted, the cross polarization $h_\times$ is chosen for visualization.

The library simplifies the process of generating gravitational waveforms, allowing for straightforward simulation and decomposition into their individual modes. This ease of use enables efficient exploration of how different parameters, such as mass ratio and spin, influence the higher-order mode contributions to the waveform.

The results of the visual analysis are presented in a 2D grid of subplots. In this grid, the vertical axis represents the increasing mass ratio q, ranging from $q = 1$ (equal masses) at the top to $q = 3$ at the bottom, in steps of 0.5. Along the horizontal axis, a second parameter is varied, depending on the specific visualization. The parameters explored on the horizontal axis include the total mass M, varied from $100M_\odot$ to $400M_\odot$ in steps of $100M_\odot$, and the inclination angle, ranging from 0 to $\pi/2$ in steps of $\pi/6$. This arrangement allows for systematic comparisons across multiple parameter configurations within a single visual framework, facilitating the identification of trends and correlations.

To ensure consistency and maintain focus on the chosen varying parameters, certain other parameters are held constant throughout the analysis. Specifically, the luminosity distance is fixed at 5 Gpc, and the spin vectors of the black holes are aligned with the z-axis, each with a magnitude of $\chi = 1$. Depending on the parameters being varied, additional parameters are also fixed. For the analysis of mass ratio versus total mass, the inclination angle is fixed at zero. Conversely, for the analysis of mass ratio versus inclination, the total mass is fixed at $M = 200M_\odot$, as this value is slightly less than in the middle of the observed total mass range. These

Die approbierte gedruckte Originalversion dieser Diplomarbeit ist an der TU Wien Bibliothek verfügbar
The approved original version of this thesis is available in print at TU Wien Bibliothek.

fixed parameters are chosen to simplify the analysis and reduce the dimensionality of the parameter space, while still allowing meaningful exploration of waveform variations driven by mass ratio, total mass and inclination.

6.1.2. Results

The results of this study are presented through a systematic exploration of the gravitational waveforms. By examining the full waveforms, the higher-order modes in isolation, and their combined contributions, we uncover the significant role of higher-order modes in shaping the gravitational wave signal under different parameter configurations.

Mass Ratio vs. Total Mass

The first set of plots in 6.2 illustrates the full waveforms for different mass ratios and total masses. In symmetric systems, where the mass ratio is $q = 1$, the waveforms are highly symmetric and dominated by the quadrupole mode. The amplitude of the waveform grows smoothly as the binary system approaches merger, and the oscillatory behavior remains regular throughout the inspiral phase.

The waveform remains stable with varying mass ratio but as the total mass increases the waveforms change significantly. Systems with low total masses produce waveforms with higher frequencies and more oscillations. As M increases, the waveform shifts to lower frequencies, with fewer oscillations, and the signal appears stretched in time.

Die approbierte gedruckte Originalversion dieser Diplomarbeit ist an der TU Wien Bibliothek verfügbar
The approved original version of this thesis is available in print at TU Wien Bibliothek.
TU Bibliothek Your knowledge hub WIEN

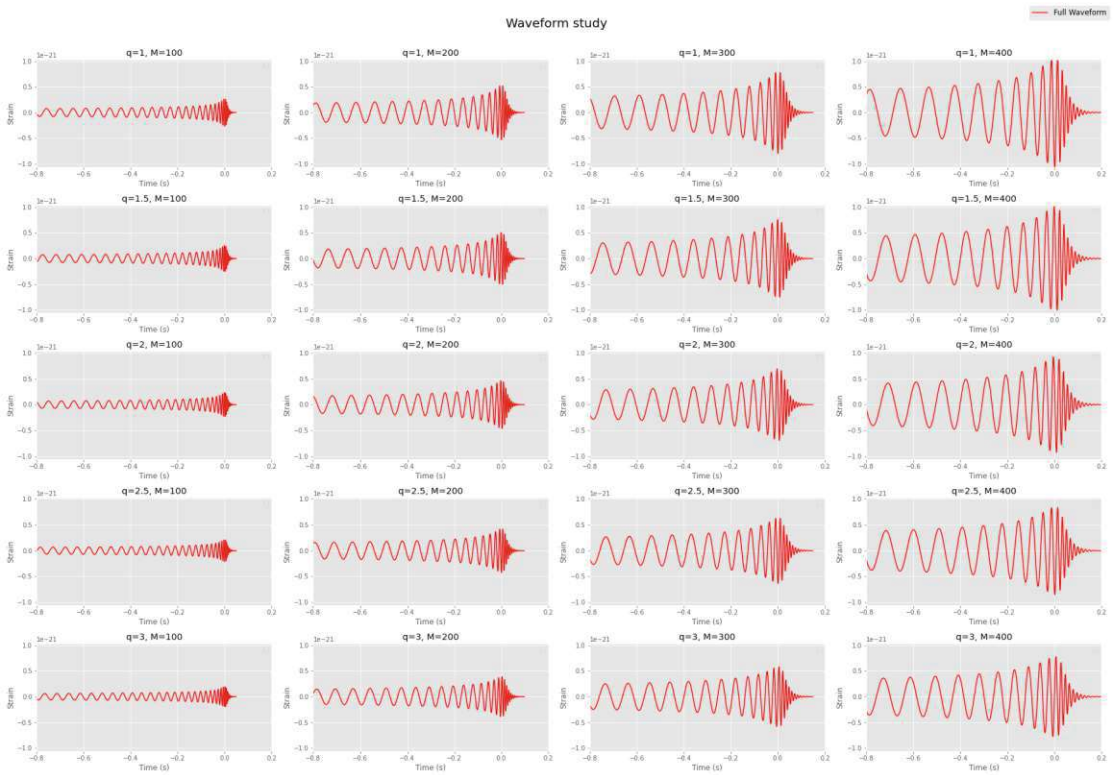

Figure 6.2.: Full gravitational waveforms for varying mass ratios (q) and total masses (M). The vertical axis represents increasing mass ratio ($q = 1$ to $q = 3$), while the horizontal axis represents increasing total mass ($M = 100M_\odot$ to $M = 400M_\odot$). Each plot shows the strain ($h_\times$) as a function of time (t) for the given parameter combination.

The second set of plots in Figure 6.3 show the higher order modes isolated. For symmetric systems, the higher-order modes are almost negligible. Their amplitudes and their oscillatory contributions are miniscule. This is consistent with the expectation that symmetric binaries primarily emit gravitational waves dominated by the quadrupole mode.

In contrast, as the total mass increases, one can now clearly see that the higher-order modes become significantly more pronounced. Their amplitudes are much larger, and the oscillatory behavior becomes more complex.

Die approbierte gedruckte Originalversion dieser Diplomarbeit ist an der TU Wien Bibliothek verfügbar
The approved original version of this thesis is available in print at TU Wien Bibliothek.
TU Bibliothek Your knowledge hub WIEN

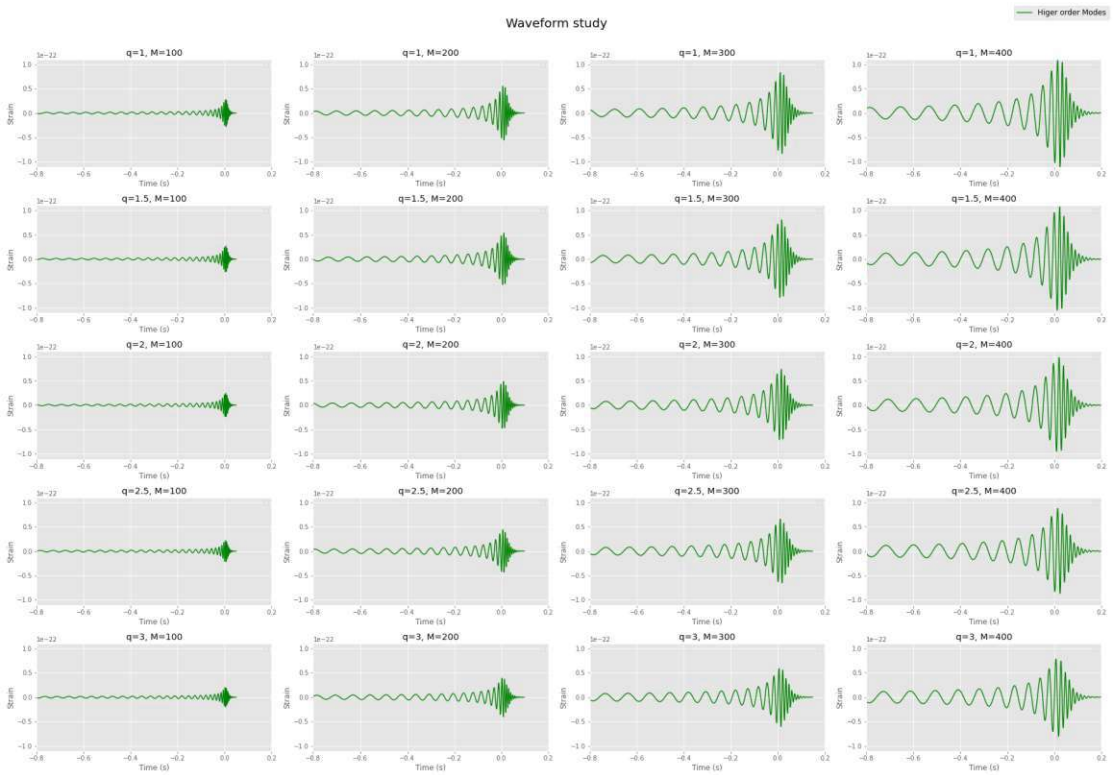

Figure 6.3.: Higher-order mode contributions to the gravitational waveforms for varying mass ratios (q) and total masses (M). The vertical axis corresponds to increasing mass ratio ($q = 1$ to $q = 3$), while the horizontal axis corresponds to increasing total mass ($M = 100M_\odot$ to $M = 400M_\odot$). Each plot shows the strain ($h_\times$) as a function of time (t) for the isolated higher-order modes.

The third set of plots overlays the full waveform with the higher-order modes, visually illustrating the relative contributions of the higher-order modes to the overall signal. While this visualization provides a qualitative sense of how higher-order modes influence the full waveform, especially near the merger phase, it becomes increasingly challenging to evaluate their precise impact with just a visual inspection. The complexity of the waveforms, particularly for systems with high mass ratios and large total masses, makes it difficult to quantify the trends and relative significance of the higher-order modes purely by eye.

Die approbierte gedruckte Originalversion dieser Diplomarbeit ist an der TU Wien Bibliothek verfügbar
The approved original version of this thesis is available in print at TU Wien Bibliothek.
TU Bibliothek Your knowledge hub WIEN

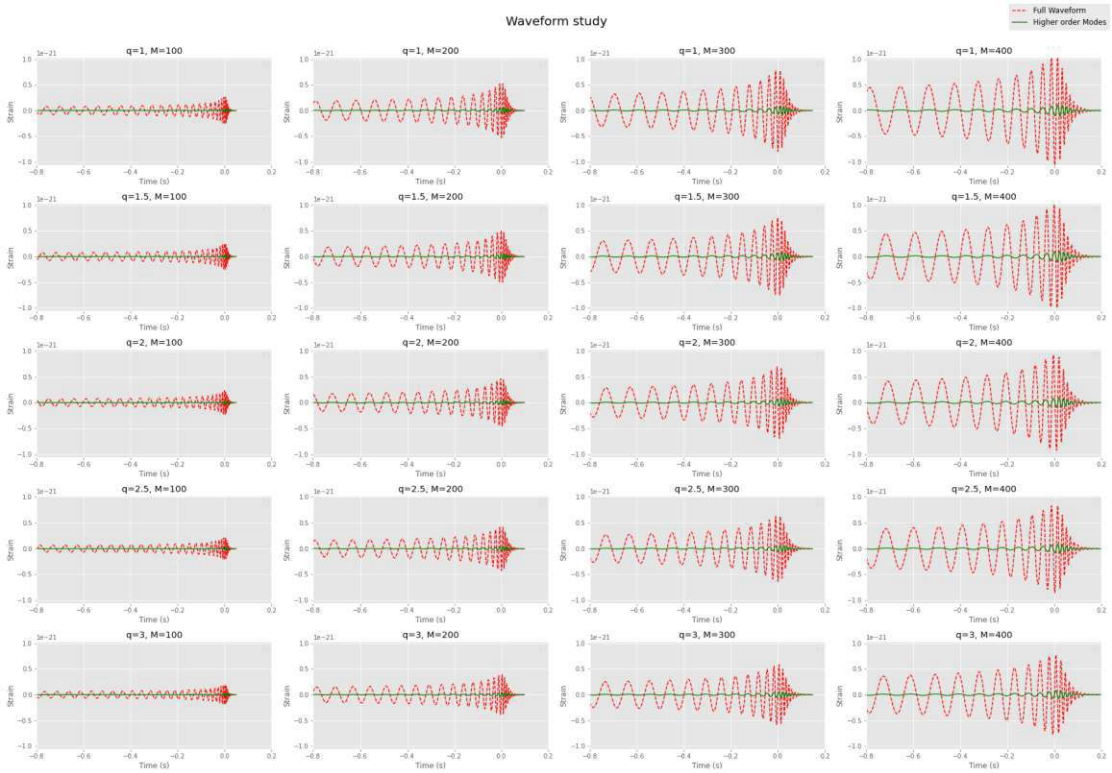

Figure 6.4.: Comparison of the full gravitational waveforms (red) and the higher-order mode contributions (green) for varying mass ratios (q) and total masses (M). The vertical axis represents increasing mass ratio ($q = 1$ to $q = 3$), while the horizontal axis represents increasing total mass ($M = 100M_\odot$ to $M = 400M_\odot$). Each plot shows the strain ($h_\times$) as a function of time (t), with the full waveform and higher-order modes overlaid.

While the analysis so far has fixed the inclination angle, we now turn to a similar investigation where the inclination is systematically varied and the total mass is fixed. This analysis will provide insights into how the relative orientation of the binary system with respect to the observer influences the contributions of higher-order modes, complementing the trends observed in the mass ratio and total mass study.

Mass ratio vs inclination angle

In Figure 6.5, which displays the full waveform, it is evident that the signal amplitude is highest when the system is observed in the face-on orientation. As the

Die approbierte gedruckte Originalversion dieser Diplomarbeit ist an der TU Wien Bibliothek verfügbar
The approved original version of this thesis is available in print at TU Wien Bibliothek.
TU Bibliothek Your knowledge hub WIEN

inclination angle increases, the signal gradually decreases in amplitude likely due to the reduced projection of the dominant quadrupole mode. A notable feature is that as the inclination approaches the edge-on configuration the difference in amplitude between the inspiral and merger phases diminishes. This results in a less pronounced transition between these phases.

Another observation is that for systems with higher mass ratios and larger inclination angles, the waveform begins to deform significantly, losing its characteristic shape. The waveform at the bottom-right corner of the grid nearly loses a clear distinction between the inspiral and merger phases, appearing quite distorted.

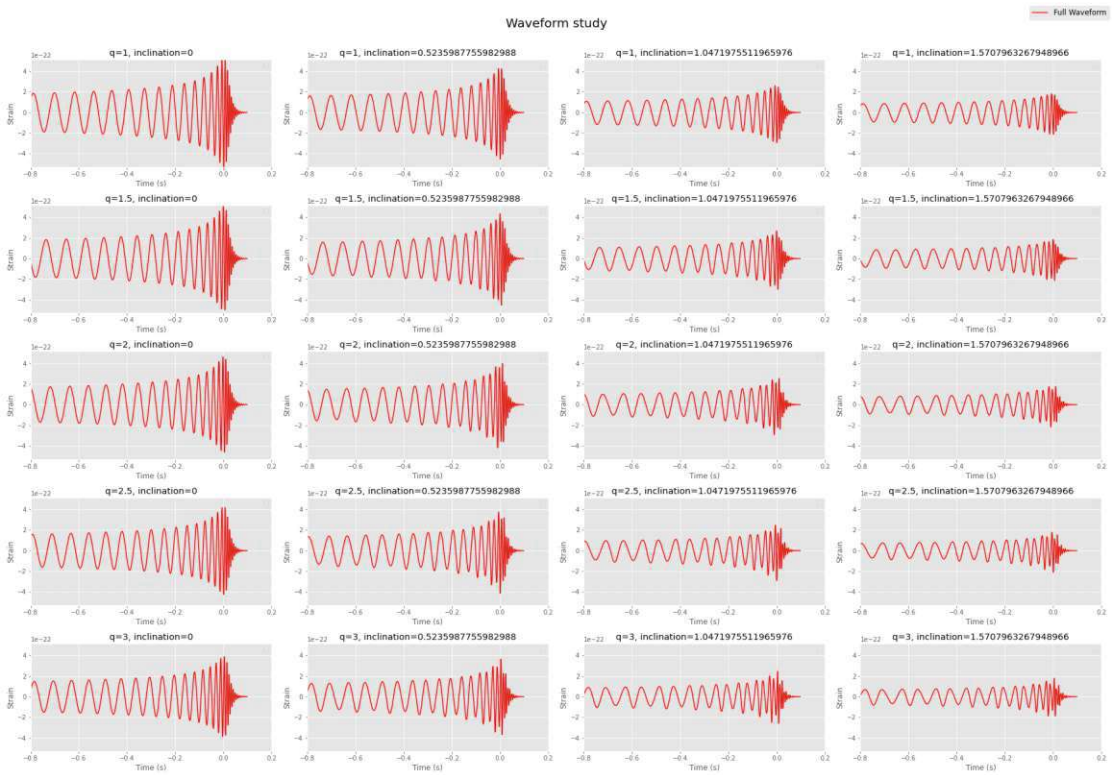

Figure 6.5.: Full gravitational waveforms for varying mass ratios and inclination. The vertical axis represents increasing mass ratio, while the horizontal axis represents increasing inclination. Each plot shows the strain ($h_\times$) as a function of time for the given parameter combination.

Figure 6.6 displays the higher-order modes in isolation. For the first column, corresponding to the face-on orientation, the waveform remains relatively stable across different mass ratios, with minimal variation in amplitude. However, as

Die approbierte gedruckte Originalversion dieser Diplomarbeit ist an der TU Wien Bibliothek verfügbar
The approved original version of this thesis is available in print at TU Wien Bibliothek.
TU Bibliothek Your knowledge hub WIEN

the inclination angle increases, the amplitude of the higher-order modes grows significantly, becoming much more pronounced. Additionally, the inspiral phase exhibits a distinct periodicity that deviates from the typical waveform structure, further emphasizing the contribution of higher-order modes. These observations indicate that higher-order modes play a crucial role in shaping the waveform at larger inclination angles, particularly in asymmetric systems.

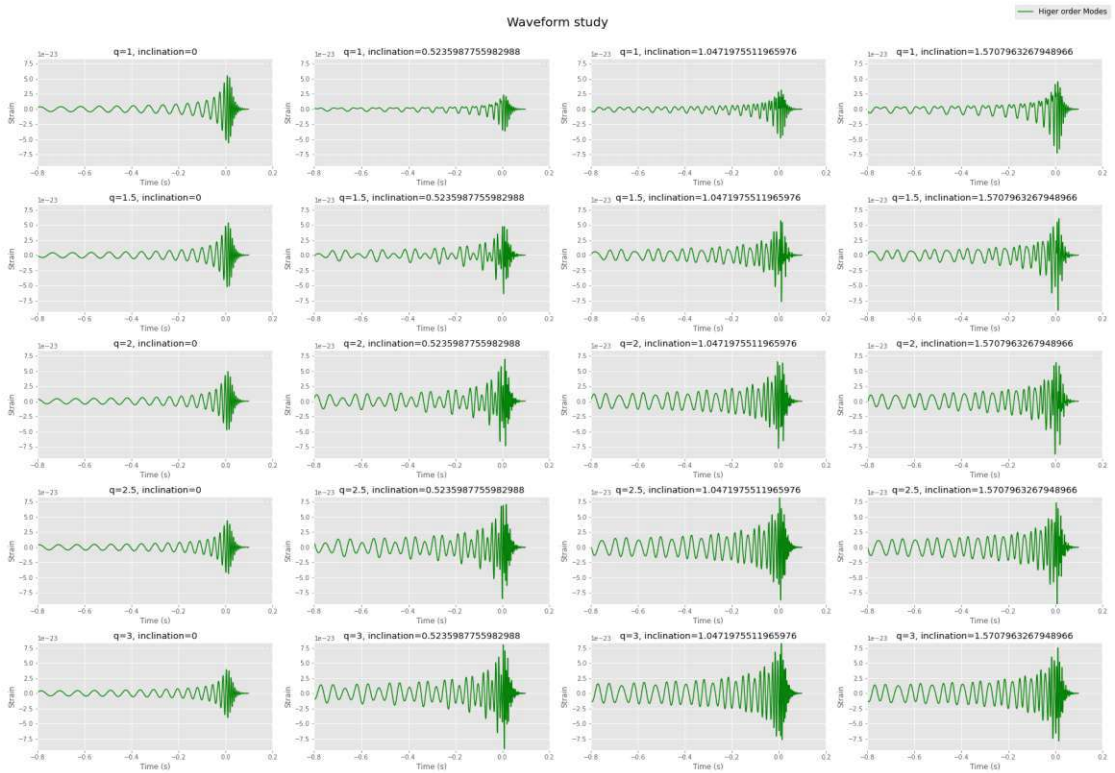

Figure 6.6.: Higher order modes for varying mass ratios and inclination. The vertical axis represents increasing mass ratio , while the horizontal axis represents increasing inclination. Each plot shows the strain ($h_\times$) as a function of time for the given parameter combination.

The last figure, 6.7, presents a different behavior compared to its counterpart with varying total mass. As the overall amplitude of the waveform decreases with increasing inclination, the contribution of the higher-order modes grows progressively. By the last column, corresponding to edge-on orientation, the higher-order modes dominate the majority of the signal. This observation confirms that inclination is a critical parameter when considering the contribution of higher-order modes to the gravitational waveform.

Die approbierte gedruckte Originalversion dieser Diplomarbeit ist an der TU Wien Bibliothek verfügbar
The approved original version of this thesis is available in print at TU Wien Bibliothek.
TU Bibliothek Your knowledge hub WIEN

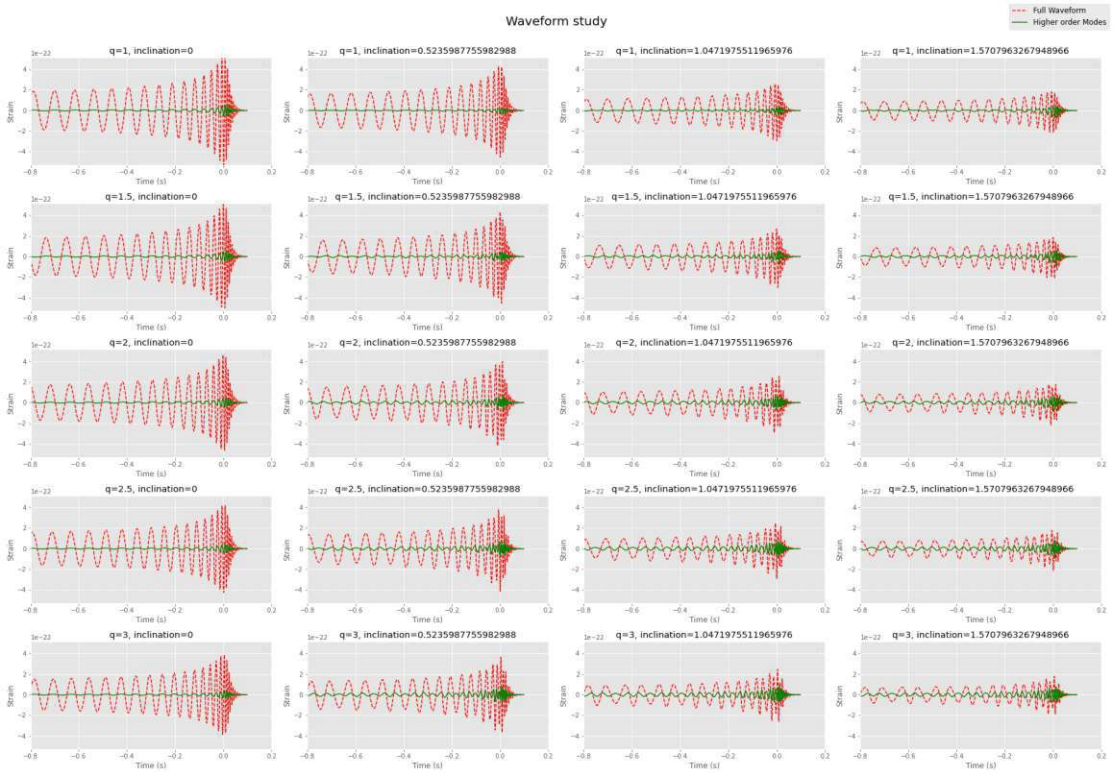

Figure 6.7.: Comparison of the full gravitational waveforms (red) and the higher-order mode contributions (green) for varying mass ratios and inclination. The vertical axis represents increasing mass ratio, while the horizontal axis represents increasing total mass. Each plot shows the strain ($h_\times$) as a function of time , with the full waveform and higher-order modes overlaid.

6.1.3. Summary

This initial analysis provides valuable insights into how different parameters, such as total mass, mass ratio, and inclination, affect gravitational waveforms and the contributions of higher-order modes.

However, while this qualitative approach is useful for understanding broad patterns, it becomes challenging to quantify the relative impact of higher-order modes.

This limitation highlights the need for a more rigorous quantitative analysis, which forms the focus of the next chapter. There, we will build upon the visual insights gained in this study and systematically quantify the contributions of higher-order

Die approbierte gedruckte Originalversion dieser Diplomarbeit ist an der TU Wien Bibliothek verfügbar
The approved original version of this thesis is available in print at TU Wien Bibliothek.

modes. Specifically, we aim to measure their relative power and evaluate how these modes influence key waveform parameters, providing a more detailed and objective understanding of their role in gravitational waveforms.

6.2. Quantitative Analysis of Higher-Order Modes in Gravitational Waveforms

While insightful, these comparisons are inherently qualitative and do not provide a clear numerical assessment of the significance of individual modes. This limitation motivates the adoption of a quantitative framework to measure the contribution of each mode dynamically throughout phases.

6.2.1. Methodology

To address this, the contribution of each gravitational-wave mode is quantified through its relative power, P_i^{rel}, which is defined as the fraction of the total power in the waveform attributable to a specific mode:

$$P_i^{\text{rel}} = \frac{P_i}{P^{\text{tot}}}, \tag{6.1}$$

where P_i represents the power of the i-th mode, computed as:

$$P_i = \frac{1}{N} \sum_{j=1}^{N} \left(\frac{\partial h_i(t_j)}{\partial t} \right)^2, \quad P^{\text{tot}} = \sum_i P_i. \tag{6.2}$$

Here, $h_i(t_j)$ is the strain amplitude of the i-th mode at the j-th discrete time step. Since waveform simulations are inherently discrete, the analysis must account for this discretization. The derivative $\frac{\partial h_i(t_j)}{\partial t}$ is approximated numerically using Python's `np.gradient` function. This method ensures accurate calculation of the derivative, even at the edges of the sampled time range, by employing a second-order finite difference scheme.

The power P_i of each mode is calculated as the squared magnitude of these numerically computed derivatives, summed over N discrete time steps. The summation over j effectively averages the power contribution across all time steps, ensuring that P_i reflects the overall contribution of the mode throughout the signal's evolution. The total power P^{tot} is then obtained by summing the individual mode powers P_i over all modes.

Die approbierte gedruckte Originalversion dieser Diplomarbeit ist an der TU Wien Bibliothek verfügbar
The approved original version of this thesis is available in print at TU Wien Bibliothek.
TU Bibliothek Your knowledge hub WIEN

This approach provides a dynamic, quantitative measure of each mode's significance relative to the total signal. By isolating the relative power P_i^{rel}, the methodology highlights how individual modes contribute to the overall waveform across different stages of the signal's evolution.

The analysis extends across specific parameter space, systematically varying the mass ratio, total mass, and inclination angle to understand their influence on mode contributions. The results are presented through a set of contour and 2D plots, which effectively visualize the dependence of relative power on specific parameters or combinations thereof.

6.2.2. Results

Figure 6.8 illustrates the relative power contributions of gravitational wave modes, comparing the dominant 2nd-order modes ($\ell = 2$) with the subdominant higher-order modes ($2 < \ell \leq 4$) for several values of total Mass inclination and mass ratio.

The 2nd-order and higher-order modes are complementary components of the gravitational-wave signal. For most configurations, the 2nd-order modes contribute the majority of the power, often exceeding 90% across the parameter space. Their dominance is particularly evident at low inclinations, where symmetry in the binary's radiation pattern suppresses higher-order contributions. However, as the inclination increases toward edge-on configurations, the relative power of higher-order modes grows significantly up until 25%.

Mass ratio also plays a crucial role in determining the balance between these modes. For symmetric binaries ($q \approx 1$), the 2nd-order modes dominate across all inclinations, while higher-order contributions remain minimal. As the mass ratio increases, the gravitational field asymmetry becomes more pronounced, leading to enhanced contributions from higher-order modes, particularly at high inclinations. This interplay is visible in the contour plots, where higher-order contributions increase with q, particularly in the regions of parameter space corresponding to edge-on orientations.

Interestingly, while the total mass does impact the gravitational-wave frequency spectrum, it appears to have little to no effect on the relative power distribution between the 2nd-order and higher-order modes within the considered mass range. The trends observed in relative power as a function of inclination and mass ratio remain consistent across all four mass values. This suggests that the relative balance between the 2nd-order and higher-order modes is governed primarily by the geometry and asymmetry of the binary, rather than the absolute scale of the

Die approbierte gedruckte Originalversion dieser Diplomarbeit ist an der TU Wien Bibliothek verfügbar
The approved original version of this thesis is available in print at TU Wien Bibliothek.
TU Bibliothek Your knowledge hub WIEN

system's mass.

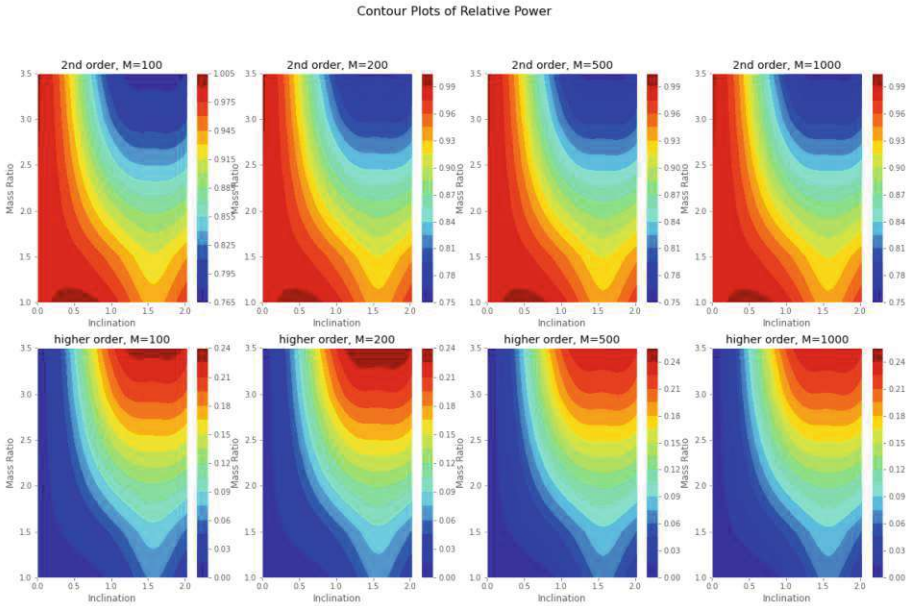

Figure 6.8.: Contour plots showing the relative power contributions of 2nd-order modes (top row) and higher-order modes (bottom row) for total masses $M = 100, 200, 500, 1000\,M_{\odot}$, as functions of mass ratio and inclination. The color intensity represents the proportion of total power contributed by each set of modes.

Figure 6.9 focuses on the individual contributions of higher-order modes as a function of q. As the mass ratio increases, certain modes, particularly $(3, \pm 3)$, exhibit a noticeable increase in their relative power contributions. For symmetric systems ($q \approx 1$), the contributions from all higher-order modes remain minimal.

Die approbierte gedruckte Originalversion dieser Diplomarbeit ist an der TU Wien Bibliothek verfügbar
The approved original version of this thesis is available in print at TU Wien Bibliothek.

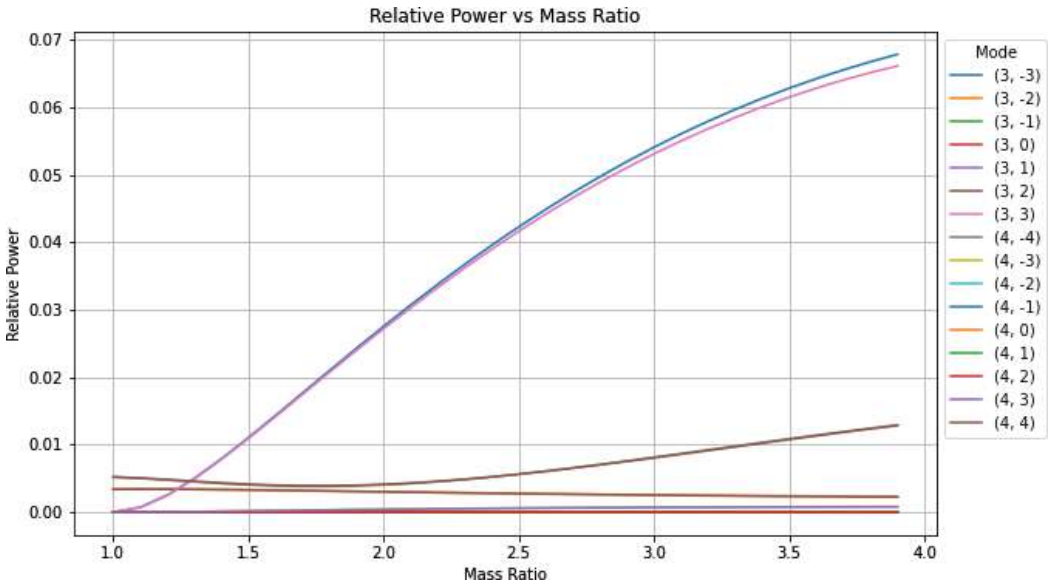

Figure 6.9.: Relative power contributions of individual higher-order modes ($\ell > 2$) as a function of mass ratio (q).

On the other side Figure 6.10 shows the individual contributions of 2nd-order modes ($\ell = 2$). For these modes, the relative power contributions remain relatively stable or show a slight decline as the mass ratio increases. Among these modes, the $(2, \pm 2)$ modes overwhelmingly dominate the relative power, contributing a significant fraction of the total signal across all mass ratios. This behavior is consistent with the dominant role of 2nd-order modes in gravitational-wave signal. The contributions of other 2nd-order modes, such as $(2, -1)$, $(2, 0)$, $(2, 1)$, and $(2, 2)$, are almost negligible in comparison.

Die approbierte gedruckte Originalversion dieser Diplomarbeit ist an der TU Wien Bibliothek verfügbar
The approved original version of this thesis is available in print at TU Wien Bibliothek.
TU Bibliothek Your knowledge hub WIEN

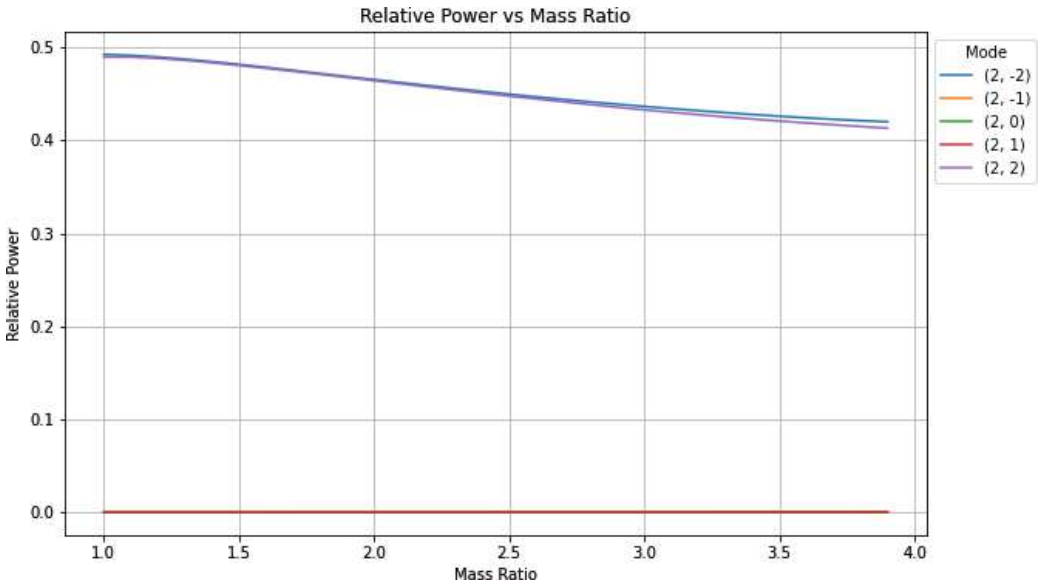

Figure 6.10.: Relative power contributions of individual 2nd order modes ($\ell = 2$) as a function of mass ratio (q).

Figure 6.11 illustrates the cumulative relative power contribution of all higher-order modes ($\ell > 2$) as a function of mass ratio. As q increases, the gravitational field asymmetry enhances the higher-order mode contributions significantly, with the total relative power exceeding 16% at the highest mass ratios analyzed.

Die approbierte gedruckte Originalversion dieser Diplomarbeit ist an der TU Wien Bibliothek verfügbar
The approved original version of this thesis is available in print at TU Wien Bibliothek.

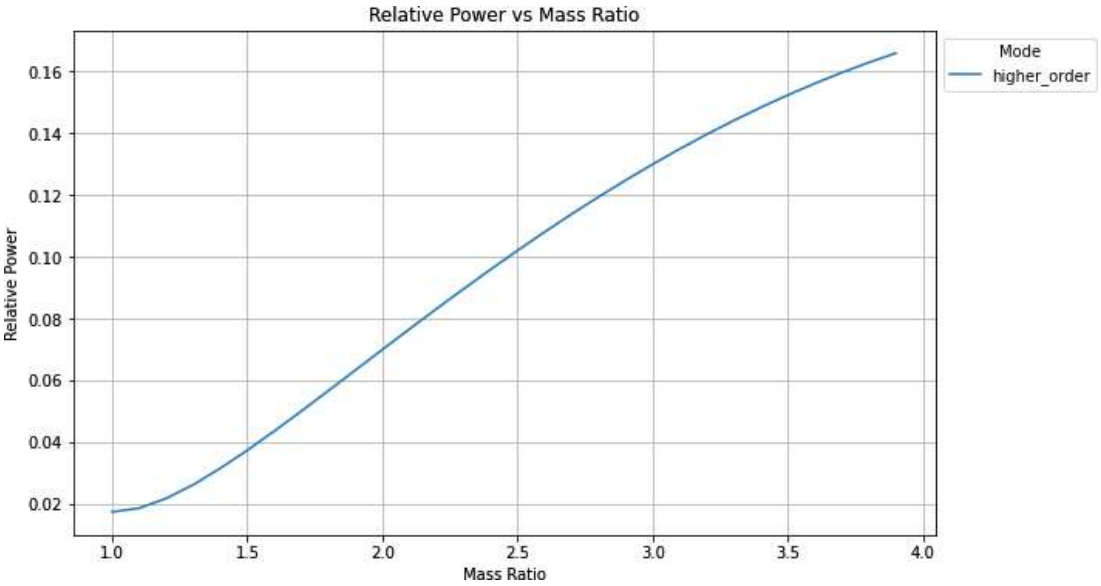

Figure 6.11.: Relative power contributions of all higher order modes ($\ell > 2$) summed as a function of mass ratio.

6.2.3. Summary

This study quantitatively assessed the relative power contributions of 2nd-order ($\ell = 2$) and higher-order ($\ell > 2$) gravitational-wave modes across a range of binary parameters, including mass ratio, inclination angle, and total mass.

The results show that 2nd-order modes dominate the signal in symmetric binaries ($q \approx 1$) and low inclinations, contributing over 90% of the total power. Higher-order modes become significant with increasing mass ratio and inclination, contributing up to 25% of the total power in highly asymmetric systems. The total mass had minimal impact on the relative power distribution, emphasizing that geometry and asymmetry primarily govern mode contributions.

6.3. Parameter Estimation Bias

This study focuses on evaluating the biases introduced by waveform approximant mismatches between injection signals produced with waveform model NRSur7dq4 and estimation signals produced by approximant IMRPhenomPv2 during the parameter estimation process. By creating a synthetic population of GW events representative of IMBH systems and utilizing the Bilby pipeline with the Dynesty

Die approbierte gedruckte Originalversion dieser Diplomarbeit ist an der TU Wien Bibliothek verfügbar
The approved original version of this thesis is available in print at TU Wien Bibliothek.
TU Bibliothek Your knowledge hub WIEN

nested sampling algorithm [65], this analysis aims to quantify deviations in recovered source parameters resulting from the use of different waveform approximants. The methodology involves systematically estimating key source parameters, and comparing the results against the true values. The detailed setup of the population generation process and the steps for parameter recovery are outlined below.

6.3.1. Methodology

A synthetic population of GW events is generated, simulating IMBH systems by sampling uniformly selected parameters within predefined ranges and fixing others at constant values. The parameter distributions used for population generation are summarized in Table 6.1.

Table 6.1.: Parameter Distributions for Population Generation

Parameter	**Description**	**Estimate**	**Range**
`mass_1`	Mass of the primary black hole (solar masses)	True	120 – 200
`mass_2`	Mass of the secondary black hole (solar masses)	True	50 – 100
`a_1`	Spin magnitude of the primary black hole	False	0 – 0
`a_2`	Spin magnitude of the secondary black hole	False	0 – 0
`tilt_1`	Tilt angle of the primary spin (radians)	False	0 – 0
`tilt_2`	Tilt angle of the secondary spin (radians)	False	0 – 0
`phi_12`	Azimuthal angle between the spins (radians)	False	0 – 0
`phi_jl`	Azimuthal angle between total and orbital angular momentum (radians)	False	0 – 0
`luminosity_distance`	Luminosity distance to the source (megaparsecs)	True	1000 – 1000
`theta_jn`	Inclination angle (radians)	False	0 – 0
`psi`	Polarization angle (radians)	False	0 – 0
`phase`	Phase at coalescence (radians)	False	0 – 0
`ra`	Right ascension of the source (radians)	False	0 – 0
`dec`	Declination of the source (radians)	False	0 – 0

Notes:

Die approbierte gedruckte Originalversion dieser Diplomarbeit ist an der TU Wien Bibliothek verfügbar
The approved original version of this thesis is available in print at TU Wien Bibliothek.

- Parameters marked as `False` are fixed at zero.

- `mass_1` and `mass_2` are randomly sampled within the specified ranges to simulate a diverse set of IMBH systems.

- `luminosity_distance` is held constant at 1000 megaparsecs to standardize signal strength across the population.

For each GW event in the generated population, parameter estimation is conducted using the `IMRPhenomPv2` waveform model, initialized with signals generated by `NRSur7dq4`. The pipeline estimates the key parameters (`mass_1`, `mass_2`, and `luminosity_distance`) through the following steps:

1. **Waveform Injection**: Use `NRSur7dq4` to generate the injection signal.

2. **PE Execution**: Use `IMRPhenomPv2` in the PE pipeline to estimate source parameters.

3. **Parameter Extraction**: Extract posterior distributions of the estimated parameters.

To quantify biases arising from approximant mismatches, the following calculations are performed:

- **Mass Bias**:

$$\Delta m_1 = m_{1,\text{estimated}} - m_{1,\text{real}}, \quad \Delta m_2 = m_{2,\text{estimated}} - m_{2,\text{real}}$$

- **Total Mass Bias**:

$$\Delta M = (m_{1,\text{estimated}} + m_{2,\text{estimated}}) - (m_{1,\text{real}} + m_{2,\text{real}})$$

- **Luminosity Distance Bias**:

$$\Delta D_L = D_{L,\text{estimated}} - D_{L,\text{real}}$$

For each parameter (`mass_1`, `mass_2`, total mass, and `luminosity_distance`), histograms of the bias distributions are constructed to visualize systematic offsets caused by the waveform approximant mismatch.

Die approbierte gedruckte Originalversion dieser Diplomarbeit ist an der TU Wien Bibliothek verfügbar
The approved original version of this thesis is available in print at TU Wien Bibliothek.

6.3.2. Results

Figure 6.12 illustrates that the primary mass m_1 exhibits a pronounced bias towards overestimation, with a mean overestimation of $31\,M_\odot$. This trend can also clearly be seen in Figure 6.15 as it shows a consistent offset of the redline which indicates perfect predictions. This indicates a systematic trend in the parameter estimation, where the heavier component of the binary system is consistently overestimated. Figure 6.18 and Figure 6.15 also indicate that there seems to be a cutoff and the algorithm actually wants to estimate the primary mass even higher.

In contrast, the secondary mass m_2 demonstrates a more balanced, more gaussian-like distribution with a mean underestimation of $4\,M_\odot$, suggesting that the bias for m_2 is less severe and more symmetrically distributed around its true value, which is also confirmed by having a slightly higher density below the red line in 6.16. This discrepancy between m_1 and m_2 biases highlights the differing sensitivities of the waveform model to the individual masses in the binary system.

When examining the total mass, Figure 6.13 reveals that the combined effects of m_1 and m_2 result in a Gaussian-like bias distribution with a mean bias of $27\,M_\odot$. This suggests that while the biases in m_1 and m_2 may partially offset each other in some cases, their combined contribution still leads to a consistent overestimation of the total mass. This observation aligns with the expected behavior, as the total mass is a direct sum of the individual components, amplifying any systematic deviations present in m_1 and m_2.

Additionally, the luminosity distance shows a consistent positive bias across the population, as depicted in Figure 6.13. This indicates a systematic tendency to overestimate the distance to the source, which could significantly impact astrophysical interpretations.

Figure 6.14 further examines the bias in the total mass and remnant mass by plotting the absolute values, which confirm a concentrated bias in both at around $30\,M_\odot$. Said trend is also clearly visible in 6.17 as an offset from the red line. This analysis reinforces the conclusion that there is a systematic overestimation of the total mass and remnant mass across this population of events. The consistent magnitude of the absolute bias highlights the robustness of this trend, irrespective of whether individual events show larger or smaller relative biases.

Die approbierte gedruckte Originalversion dieser Diplomarbeit ist an der TU Wien Bibliothek verfügbar
The approved original version of this thesis is available in print at TU Wien Bibliothek.
TU Bibliothek Your knowledge hub WIEN

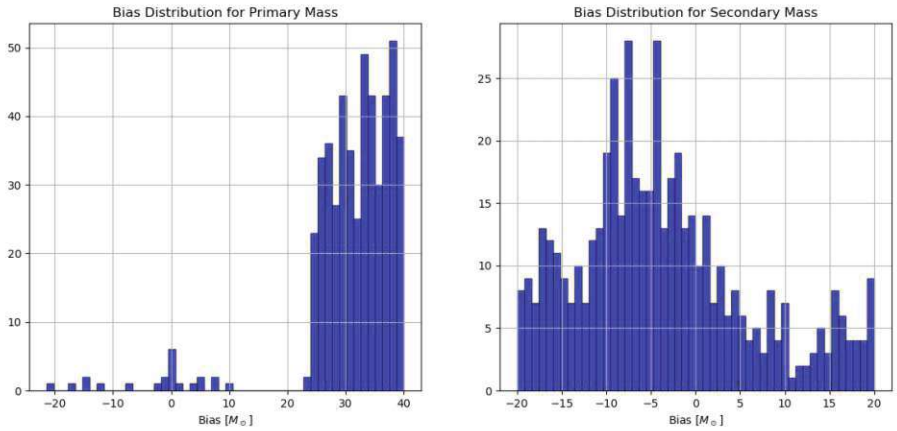

Figure 6.12.: Bias distribution for primary and secondary mass

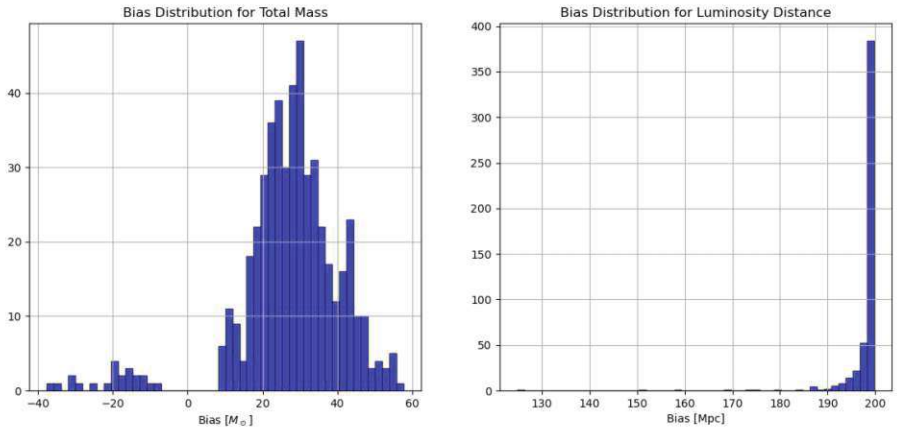

Figure 6.13.: Bias distribution for total mass and luminosity distance

Die approbierte gedruckte Originalversion dieser Diplomarbeit ist an der TU Wien Bibliothek verfügbar
The approved original version of this thesis is available in print at TU Wien Bibliothek.

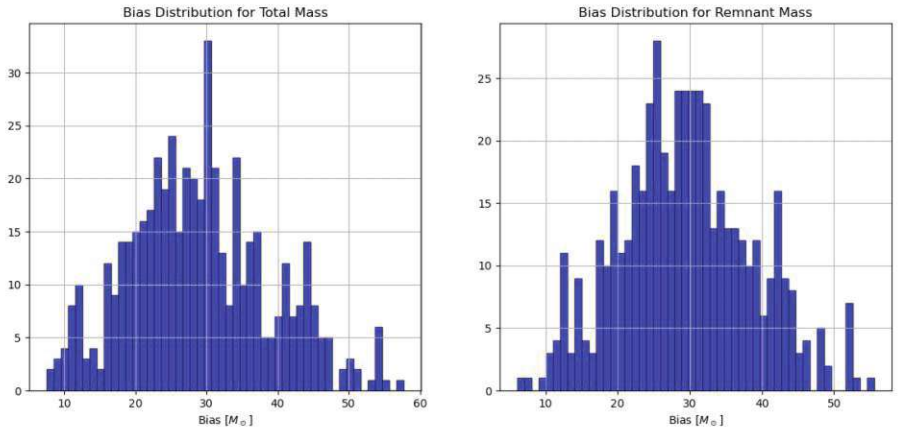

Figure 6.14.: Bias distribution of the absolute value of the total mass and remnant mass

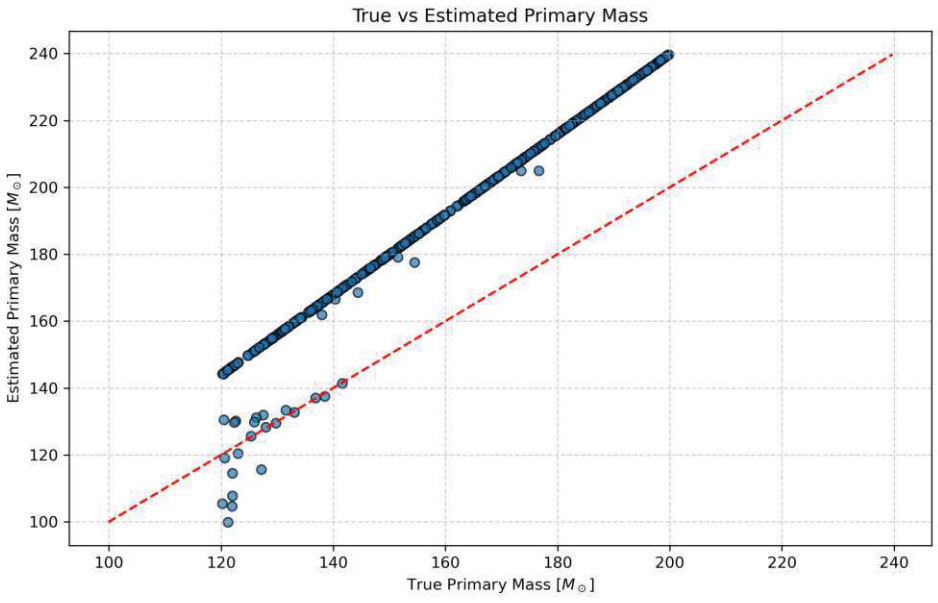

Figure 6.15.: Scatter plot between true and estimated primary mass

Die approbierte gedruckte Originalversion dieser Diplomarbeit ist an der TU Wien Bibliothek verfügbar
The approved original version of this thesis is available in print at TU Wien Bibliothek.

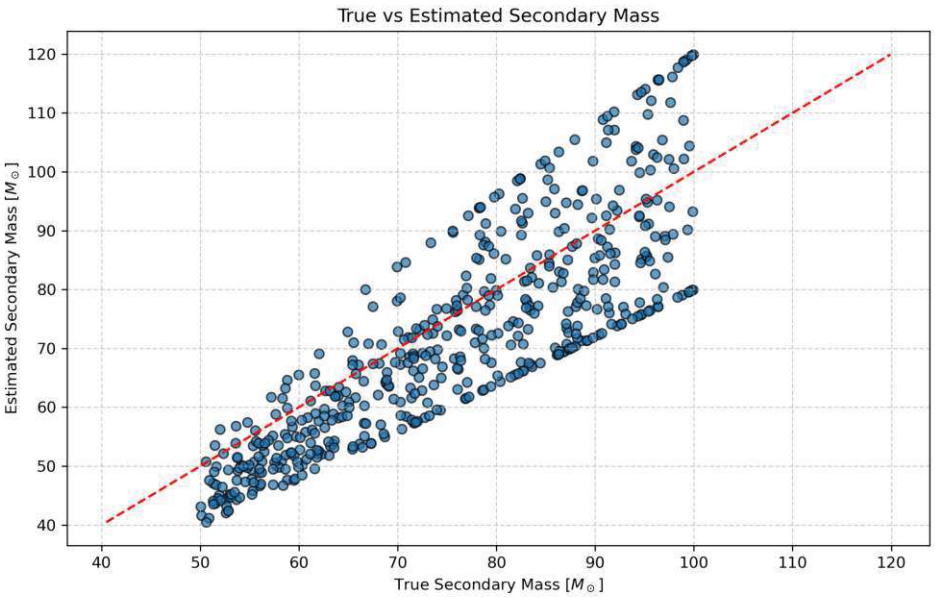

Figure 6.16.: Scatter plot between true and estimated secondary mass

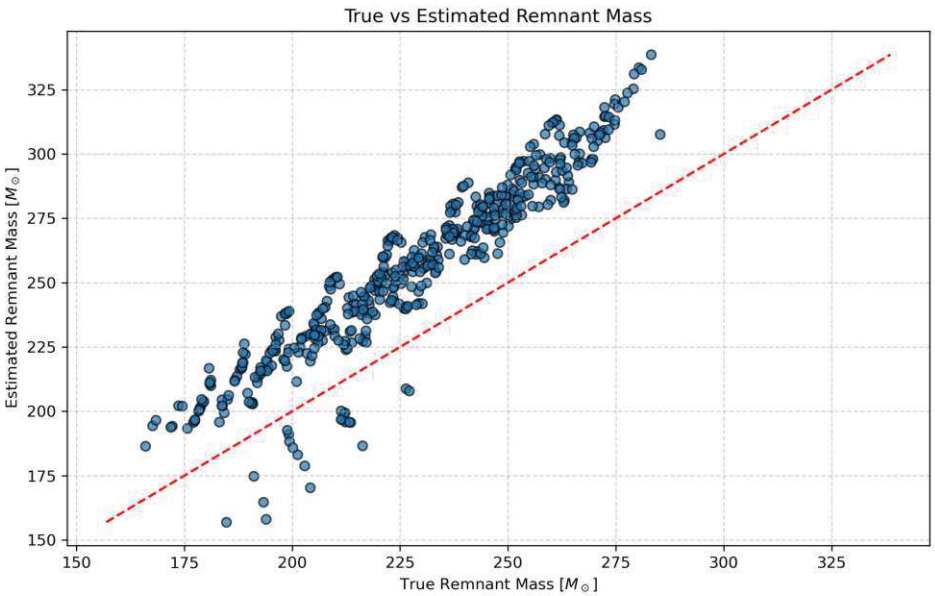

Figure 6.17.: Scatter plot between true and estimated remnant mass

Die approbierte gedruckte Originalversion dieser Diplomarbeit ist an der TU Wien Bibliothek verfügbar
The approved original version of this thesis is available in print at TU Wien Bibliothek.

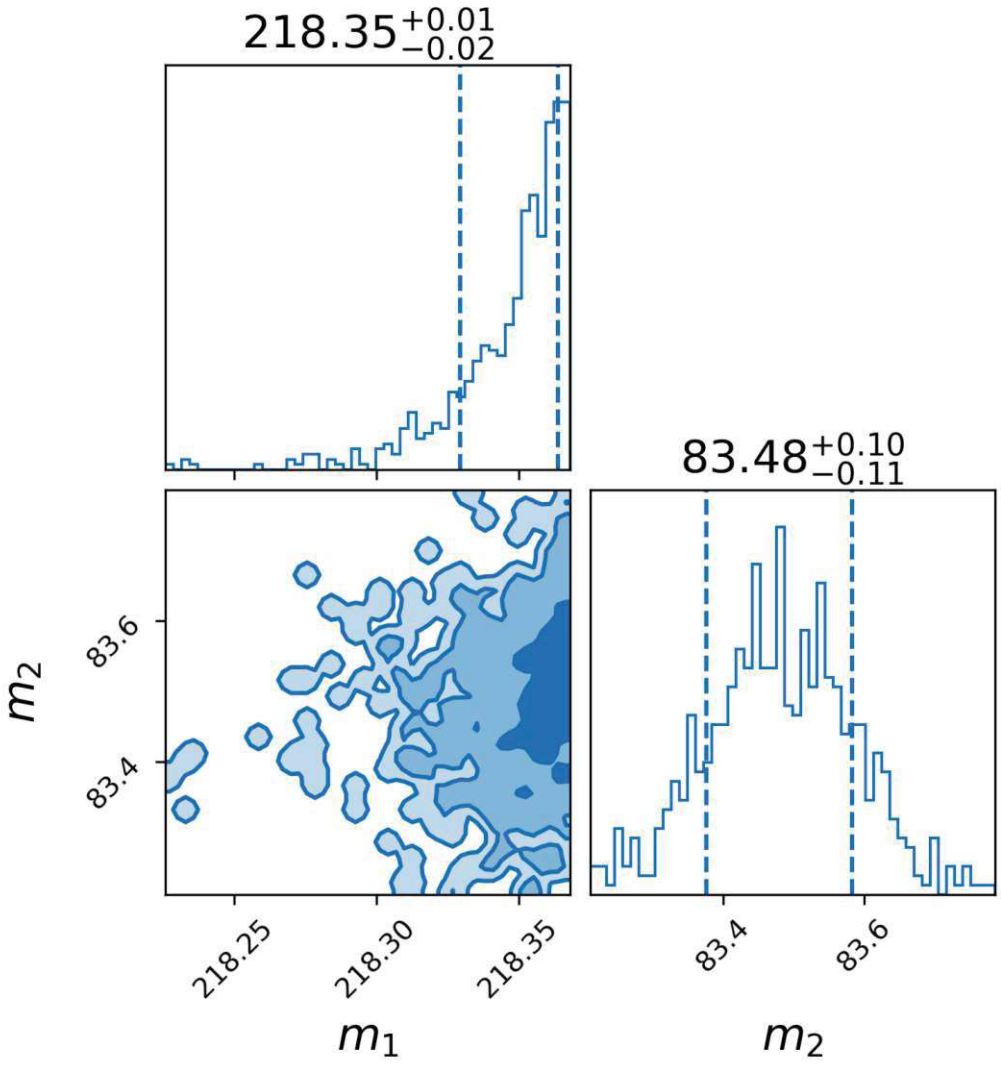

Figure 6.18.: Poserior distribution of primary mass m_1 and secondary mass m_2 for a single gravitational wave event, showing joint 2D contours and marginalized 1D distributions.

6.3.3. Summary

In conclusion, this study highlights significant biases in the parameter estimation of IMBH systems, particularly the systematic overestimation of primary, total mass and remnant mass alongside a consistent bias in luminosity distance. These findings emphasize the need for improved waveform models and parameter estimation methods to reduce systematic errors.

Die approbierte gedruckte Originalversion dieser Diplomarbeit ist an der TU Wien Bibliothek verfügbar
The approved original version of this thesis is available in print at TU Wien Bibliothek.
TU Bibliothek Your knowledge hub WIEN

6.4. Conclusion

This thesis explored the theoretical and practical aspects of gravitational wave science, with a particular focus on waveform modeling and parameter estimation for intermediate-mass black hole systems. The work was structured to provide a comprehensive overview of gravitational wave theory, detection methods, data analysis techniques, and the challenges in waveform modeling.

The initial chapters laid the foundation by introducing the theoretical framework of General Relativity and gravitational waves, including their production, propagation, and detection. The discussion of gravitational wave detection detailed the principles of Michelson interferometry, sources of detector noise, and the global network of detectors, including LIGO, Virgo, and KAGRA. These chapters provided the necessary context for understanding the complexities of data analysis and waveform modeling.

The thesis then delved into the principles of GW data analysis, with an emphasis on matched filtering, Bayesian parameter estimation, and nested sampling methods. These techniques are fundamental for extracting information from GW signals and were essential for the subsequent research presented in this study.

The core research focused on simulating GW signals from IMBH systems and assessing the impact of higher order modes on waveform signals and waveform approximant selection on parameter estimation accuracy. By comparing two prominent waveform models, `NRSur7dq4` (a surrogate model) and `IMRPhenomPv2` (a phenomenological model), the study quantified biases in key source parameters such as masses and luminosity distance.

The results revealed that higher-order modes play a crucial role in accurately modeling IMBH mergers, especially in cases with higher mass ratios and larger inclinations, where their contribution becomes more pronounced. These modes significantly affect the morphology of gravitational wave signals. Furthermore, the study demonstrated that relying on less accurate approximants, such as `IMRPhenomPv2`, leads to systematic biases in the estimation of key source parameters.

In summary, this thesis serves as a foundational contribution to IMBH research, providing a comprehensive theoretical and methodological framework while offering original insights into waveform modeling and parameter estimation. The findings presented here highlight the trade-offs between accuracy and efficiency in current approaches and lay the groundwork for future advancements in gravitational wave data analysis and astrophysical modeling, paving the way for further

Die approbierte gedruckte Originalversion dieser Diplomarbeit ist an der TU Wien Bibliothek verfügbar
The approved original version of this thesis is available in print at TU Wien Bibliothek.
TU Bibliothek Your knowledge hub WIEN

progress in this emerging field.

Despite its contributions, the study is subject to certain limitations. Addressing these limitations in future work could enhance the robustness and applicability of the findings.

6.5. Future Work

This study lays the groundwork for exploring systematic biases in parameter estimation, but several avenues remain open for future research. One natural extension is to increase the statistical robustness of the results by analyzing a larger population of gravitational wave events beyond the 500 considered here. Expanding the study to cover different regions of the parameter space would also provide insights into how the biases observed in this work vary across diverse IMBH configurations. Furthermore, other waveform approximants could be employed to test their accuracy and assess how biases change when different modeling techniques are used. A broader range of priors could also be considered to evaluate the influence of prior assumptions on parameter estimation biases. Another promising direction involves exploring how bias evolves dynamically by varying one parameter at a time, such as inclination or mass ratio, to identify potential trends or correlations.

For the related studies involving higher-order modes, future work could examine the role of other critical parameters, such as spin magnitudes and orientations, to determine their impact on the waveform structure. Additionally, more focused investigations could target specific phases of the waveform - such as the merger or ringdown - where nonlinear effects are most pronounced, enabling a more detailed understanding of the influence of higher-order modes in these regimes. These directions would not only build upon the findings of this study but also enhance the broader understanding of gravitational waveforms and their astrophysical implications.

Die approbierte gedruckte Originalversion dieser Diplomarbeit ist an der TU Wien Bibliothek verfügbar
The approved original version of this thesis is available in print at TU Wien Bibliothek.
TU Bibliothek Your knowledge hub WIEN

Bibliography

[1] B. P. Abbott et al. "Observation of Gravitational Waves from a Binary Black Hole Merger". In: *Physical Review Letters* 116.6 (2016), p. 061102. DOI: 10.1103/PhysRevLett.116.061102. URL: https://journals.aps.org/prl/abstract/10.1103/PhysRevLett.116.061102.

[2] B. P. Abbott et al. "Prospects for observing and localizing gravitational-wave transients with Advanced LIGO, Advanced Virgo and KAGRA". In: *Living Reviews in Relativity* 23.3 (2020), pp. 1–69. DOI: 10.1007/s41114-020-00026-9. URL: https://link.springer.com/article/10.1007/s41114-020-00026-9.

[3] R. Abbott et al. "GWTC-2: Compact Binary Coalescences Observed by LIGO and Virgo during the First Half of the Third Observing Run". In: *Physical Review X* 11.2 (2021), p. 021053. DOI: 10.1103/PhysRevX.11.021053.

[4] R. Abbott et al. "GWTC-2.1: Deep extended catalog of compact binary coalescences observed by LIGO and Virgo during the first half of the third observing run". In: *Physical Review D* 109 (2024), p. 022001. DOI: 10.1103/PhysRevD.109.022001.

[5] T. Accadia et al. "Virgo: a laser interferometer to detect gravitational waves". In: *Journal of Instrumentation* 7 (2012), P03012. DOI: 10.1088/1748-0221/7/03/P03012.

[6] F. Acernese et al. "Advanced Virgo: a second-generation interferometric gravitational wave detector". In: *Classical and Quantum Gravity* 32.2 (2015), p. 024001. DOI: 10.1088/0264-9381/32/2/024001.

[7] Michael Boyle et al. "The SXS Collaboration catalog of binary black hole simulations". In: *arXiv preprint arXiv:1904.04831* (2019). URL: https://arxiv.org/abs/1904.04831.

[8] Surabhi Sachdev et al. "The GstLAL Search Analysis Methods for Compact Binary Mergers in Advanced LIGO's Second and Advanced Virgo's First Observing Runs". In: *arXiv preprint arXiv:1901.08580* (2019). URL: https://arxiv.org/abs/1901.08580.

Die approbierte gedruckte Originalversion dieser Diplomarbeit ist an der TU Wien Bibliothek verfügbar
The approved original version of this thesis is available in print at TU Wien Bibliothek.
TU Bibliothek Your knowledge hub WIEN

[9] Fabio Antonini and Mark Gieles. "Population synthesis of black hole binary mergers from star clusters". In: *Monthly Notices of the Royal Astronomical Society* 492.4 (2020), pp. 2936–2956. DOI: 10.1093/mnras/stz3584. arXiv: 1906.11855 [astro-ph.HE]. URL: https://doi.org/10.48550/arXiv.1906.11855.

[10] Gregory Ashton et al. "BILBY: A user-friendly Bayesian inference library for gravitational-wave astronomy". In: *Astrophys. J. Suppl.* 241.2 (2019), p. 27. DOI: 10.3847/1538-4365/ab06fc. arXiv: 1811.02042 [astro-ph.IM].

[11] Abbas Askar, Vivienne F. Baldassare, and Mar Mezcua. "Intermediate-Mass Black Holes in Star Clusters and Dwarf Galaxies". In: *arXiv preprint* (Feb. 2024). Version 5. arXiv: 2311.12118 [astro-ph.GA]. URL: https://arxiv.org/abs/2311.12118.

[12] Matthias Bartelmann. *Theoretische Physik*. Springer, 2014.

[13] Jonathan Blackman et al. "A Numerical Relativity Waveform Surrogate Model for Generically Precessing Binary Black Hole Mergers". In: *Physical Review D* 96 (2017), p. 024058. DOI: 10.1103/PhysRevD.96.024058. arXiv: 1705.07089 [gr-qc]. URL: https://doi.org/10.1103/PhysRevD.96.024058.

[14] Jonathan Blackman et al. *gwsurrogate*. https://pypi.python.org/pypi/gwsurrogate/.

[15] Luc Blanchet. "Gravitational Radiation from Post-Newtonian Sources and Inspiralling Compact Binaries". In: *Living Reviews in Relativity* 17.2 (2014). DOI: 10.12942/lrr-2014-2. URL: https://doi.org/10.12942/lrr-2014-2.

[16] Marica Branchesi et al. "Science with the Einstein Telescope: a comparison of different designs". In: *arXiv preprint* (2023). Accepted in JCAP, ET-0084A-23. arXiv: 2303.15923 [gr-qc]. URL: https://arxiv.org/abs/2303.15923.

[17] Tito Dal Canton et al. "Real-time Search for Compact Binary Mergers in Advanced LIGO and Virgo's Third Observing Run Using PyCBC Live". In: *The Astrophysical Journal* 923.2 (2021), p. 254. DOI: 10.3847/1538-4357/ac2f9a. URL: https://doi.org/10.3847/1538-4357/ac2f9a.

[18] Sean M. Carroll. *Spacetime and Geometry: An Introduction to General Relativity*. San Francisco: Addison-Wesley, 2004. ISBN: 978-0805387322.

[19] J. Casares and P. G. Jonker. "Mass Measurements of Stellar and Intermediate-Mass Black Holes". In: *Space Science Reviews (Space Sci. Rev.)* 183 (Sept. 2014), pp. 223–252. DOI: 10.1007/s11214-013-0030-6. arXiv: 1311.5118.

Die approbierte gedruckte Originalversion dieser Diplomarbeit ist an der TU Wien Bibliothek verfügbar
The approved original version of this thesis is available in print at TU Wien Bibliothek.
TU Bibliothek Your knowledge hub WIEN

[20] A. Celotti, J. C. Miller, and D. W. Sciama. "Astrophysical Evidence for the Existence of Black Holes". In: *Classical and Quantum Gravity* 16.12A (1999), A3–A21. DOI: 10.1088/0264-9381/16/12A/002.

[21] S. Chandrasekhar. "Some Remarks on the State of Matter in the Interior of Stars". In: *Zeitschrift für Astrophysik* 5 (1932), pp. 32–40.

[22] S. Chandrasekhar. "The highly collapsed configurations of a stellar mass (Second paper)". In: *Monthly Notices of the Royal Astronomical Society (MNRAS)* 95 (Jan. 1935), pp. 207–225.

[23] Event Horizon Telescope Collaboration. "First M87 Event Horizon Telescope Results. I. The Shadow of the Supermassive Black Hole". In: *The Astrophysical Journal Letters* 875.1 (2019), p. L1. DOI: 10.3847/2041-8213/ab0ec7.

[24] LIGO Scientific Collaboration. "Advanced LIGO". In: *LIGO-P1400177* (2014). Version 5. URL: https://arxiv.org/abs/....

[25] The LIGO Scientific Collaboration and The Virgo Collaboration. "GW170817: Observation of Gravitational Waves from a Binary Neutron Star Inspiral". In: *arXiv preprint* (2017). arXiv: 1710.05832 [gr-qc]. URL: https://arxiv.org/abs/1710.05832.

[26] The LIGO Scientific Collaboration, the Virgo Collaboration, and the KAGRA Collaboration. "GWTC-3: Compact Binary Coalescences Observed by LIGO and Virgo During the Second Part of the Third Observing Run". In: *Physical Review X* 13 (2023). Submitted on 5 Nov 2021, last revised 23 Oct 2023, p. 031001. DOI: 10.1103/PhysRevX.13.031001.

[27] The LIGO Scientific Collaboration et al. "GW190521: A Binary Black Hole Merger with a Total Mass of 150 $M_\odot$". In: *Physical Review Letters* 125.10 (2020), p. 101102. DOI: 10.1103/PhysRevLett.125.101102. arXiv: 2009.01075 [gr-qc]. URL: https://doi.org/10.48550/arXiv.2009.01075.

[28] Cosmic Explorer Consortium. *Cosmic Explorer: Next-generation gravitational-wave observatories*. https://cosmicexplorer.org. Accessed: 2024-11-24. 2024.

[29] Jolien D. E. Creighton and Warren G. Anderson. *Gravitational-Wave Physics and Astronomy: An Introduction to Theory, Experiment and Data Analysis*. Wiley Series in Cosmology. Weinheim, Germany: Wiley-VCH, 2011. ISBN: 978-3-527-40886-3.

[30] J. Droste. "The field of a single centre in Einstein's theory of gravitation, and the motion of a particle in that field". In: *Ned. Acad. Wet., SA* 19 (1917), p. 197.

Die approbierte gedruckte Originalversion dieser Diplomarbeit ist an der TU Wien Bibliothek verfügbar
The approved original version of this thesis is available in print at TU Wien Bibliothek.
TU Bibliothek Your knowledge hub WIEN

[31] J Glanzer et al. “Noise in the LIGO Livingston Gravitational Wave Observatory due to Trains”. In: *arXiv preprint arXiv:2304.07477* (2023). URL: https://arxiv.org/abs/2304.07477.

[32] David J. Griffiths. *Introduction to Electrodynamics*. 3rd. Upper Saddle River, NJ: Prentice Hall, 1999.

[33] S. W. Hawking. “Gravitationally Collapsed Objects of Very Low Mass”. In: *Monthly Notices of the Royal Astronomical Society* 152.1 (1971), pp. 75–78. DOI: 10.1093/mnras/152.1.75.

[34] Xin-Bo He, Pak-Hin Thomas Tam, and Rong-Feng Shen. “GRB 170817A: a short GRB seen off-axis”. In: *Research in Astronomy and Astrophysics* 18.4 (2018), p. 043. DOI: 10.1088/1674-4527/18/4/43.

[35] David Hilbert. “Die Grundlagen der Physik”. In: *Nachrichten von der Gesellschaft der Wissenschaften zu Göttingen, Mathematisch-Physikalische Klasse* (1917), pp. 53–76.

[36] J. D. Hunter. “Matplotlib: A 2D Graphics Environment”. In: *Computing in Science & Engineering* 9.3 (2007), pp. 90–95.

[37] IGWN Collaboration. *Online Pipelines - IGWN Public Alerts User Guide*. https://emfollow.docs.ligo.org/userguide/analysis/searches.html. Accessed: 30 November 2024.

[38] IGWN Collaboration. *Sky Localization and Parameter Estimation - IGWN Public Alerts User Guide*. https://emfollow.docs.ligo.org/userguide/analysis/sky_localization.html. Accessed: 30 November 2024.

[39] Walter Isaacson. *Einstein: His Life and Universe*. New York: Simon & Schuster, 2007. ISBN: 978-0-7432-6473-0.

[40] Science Japan by JST. *The ’KAGRA’ gravitational wave telescope has resumed observations for the first time in three years: Possible development of a sensitivity improvement strategy through international collaboration*. https://sj.jst.go.jp/stories/2023/s0711-01p.html. Accessed: 2024-11-24. 2023.

[41] Sebastian Khan et al. “Phenomenological model for the gravitational-wave signal from precessing binary black holes with two-spin effects”. In: *arXiv preprint arXiv:1809.10113* (2018). URL: https://arxiv.org/abs/1809.10113.

[42] S. Klimenko et al. “Constraint likelihood analysis for a network of gravitational wave detectors”. In: *Physical Review D* 72 (2005), p. 122002. DOI: 10.1103/PhysRevD.72.122002. URL: https://doi.org/10.1103/PhysRevD.72.122002.

Die approbierte gedruckte Originalversion dieser Diplomarbeit ist an der TU Wien Bibliothek verfügbar
The approved original version of this thesis is available in print at TU Wien Bibliothek.

[43] S. Klimenko et al. “Method for detection and reconstruction of gravitational wave transients with networks of advanced detectors”. In: *Physical Review D* 93 (2016), p. 042004. DOI: 10.1103/PhysRevD.93.042004. URL: https://doi.org/10.1103/PhysRevD.93.042004.

[44] Kostas D. Kokkotas and Bernd G. Schmidt. “Quasi-Normal Modes of Stars and Black Holes”. In: *Living Reviews in Relativity* 2.2 (1999). DOI: 10.12942/lrr-1999-2. URL: https://doi.org/10.12942/lrr-1999-2.

[45] L. D. Landau. “On the theory of stars”. In: *Physikalische Zeitschrift der Sowjetunion* 1 (1932), pp. 285–288.

[46] Caltech LIGO Laboratory and MIT. *LIGO-India: A Planned Joint India-US Detector*. https://ligo.caltech.edu/page/ligo-india. Accessed: 2024-11-24. 2024.

[47] Ryan Lynch et al. “Information-theoretic approach to the gravitational-wave burst detection problem”. In: *Physical Review D* 95 (2017), p. 104046. DOI: 10.1103/PhysRevD.95.104046. URL: https://doi.org/10.1103/PhysRevD.95.104046.

[48] Piero Madau and Martin J. Rees. “Massive Black Holes as Population III Remnants”. In: *Astrophysical Journal Letters* 551 (2001), pp. L27–L30. DOI: 10.1086/319848. arXiv: astro-ph/0101223 [astro-ph]. URL: https://doi.org/10.48550/arXiv.astro-ph/0101223.

[49] J. M. Miller, A. C. Fabian, and M. C. Miller. “A Comparison of Intermediate Mass Black Hole Candidate ULXs and Stellar-Mass Black Holes”. In: *Astrophysical Journal* 614 (2004), pp. 117–120. DOI: 10.1086/425316. arXiv: astro-ph/0406656 [astro-ph]. URL: https://doi.org/10.48550/arXiv.astro-ph/0406656.

[50] Charles W. Misner, Kip S. Thorne, and John Archibald Wheeler. *Gravitation*. San Francisco: W. H. Freeman and Company, 1973. ISBN: 978-0716703440.

[51] NASA and ESA. *Laser Interferometer Space Antenna (LISA)*. https://lisa.nasa.gov. Accessed: 2024-11-24. 2024.

[52] NASA General Coordinates Network. *Gravitational Wave Network - LIGO/Virgo/KAGRA*. https://gcn.nasa.gov/missions/lvk. Accessed: 2024-11-24. 2023.

[53] Alex Nitz et al. *gwastro/pycbc: v2.3.3 release of PyCBC*. Version v2.3.3. 2024. DOI: 10.5281/zenodo.10473621. URL: https://zenodo.org/record/10473621.

Die approbierte gedruckte Originalversion dieser Diplomarbeit ist an der TU Wien Bibliothek verfügbar
The approved original version of this thesis is available in print at TU Wien Bibliothek.
TU Bibliothek Your knowledge hub WIEN

[54] Alexander H. Nitz et al. “Rapid detection of gravitational waves from compact binary mergers with PyCBC Live”. In: *Physical Review D* 98.2 (2018), p. 024050. DOI: 10.1103/PhysRevD.98.024050. URL: https://doi.org/10.1103/PhysRevD.98.024050.

[55] OpenAI. *ChatGPT*. 2024. URL: https://openai.com/chatgpt.

[56] Frans Pretorius. “Evolution of Binary Black Hole Spacetimes”. In: *Physical Review Letters* 95 (2005), p. 121101. DOI: 10.1103/PhysRevLett.95.121101. URL: https://arxiv.org/abs/gr-qc/0507014.

[57] R. A. Remillard and J. E. McClintock. “X-Ray Properties of Black-Hole Binaries”. In: *Annual Review of Astronomy and Astrophysics (ARA&A)* 44 (Sept. 2006), pp. 49–92. DOI: 10.1146/annurev.astro.44.051905.092532. arXiv: astro-ph/0606352.

[58] K. F. Riley, M. P. Hobson, and S. J. Bence. *Mathematical Methods for Physics and Engineering*. 3rd. Cambridge University Press, 2006.

[59] Carl L. Rodriguez et al. “Dynamical Formation of the GW150914 Binary Black Hole”. In: *Astrophysical Journal Letters* 824.2 (2016), p. L8. DOI: 10.3847/2041-8205/824/2/L8. arXiv: 1604.04254 [astro-ph.HE]. URL: https://doi.org/10.48550/arXiv.1604.04254.

[60] Samuel Rowlinson et al. “Feasibility study of beam-expanding telescopes in the interferometer arms for the Einstein Telescope”. In: *arXiv preprint* (2020). To be published in Phys. Rev. D 103, 023004 (2021). arXiv: 2011.02983 [astro-ph.IM]. URL: https://arxiv.org/abs/2011.02983.

[61] R. H. Sanders and T. Lowinger. “The Distribution of Mass in the Galactic Nucleus”. In: *The Astronomical Journal* 77.4 (May 1972), pp. 292–293. DOI: 10.1086/111310.

[62] Karl Schwarzschild. “On the Gravitational Field of a Mass Point According to Einstein’s Theory”. English (translated from German). In: *Sitzungsberichte der Königlich Preußischen Akademie der Wissenschaften* (1916). Original title: "Über das Gravitationsfeld eines Massenpunktes nach der Einsteinschen Theorie", pp. 189–196. URL: https://ui.adsabs.harvard.edu/abs/1916SPAW.....189S.

[63] Vasileios Skiliris, Michael R. K. Norman, and Patrick J. Sutton. “Real-Time Detection of Unmodelled Gravitational-Wave Transients Using Convolutional Neural Networks”. In: *arXiv preprint arXiv:2009.14611* (2020). URL: https://doi.org/10.48550/arXiv.2009.14611.

Die approbierte gedruckte Originalversion dieser Diplomarbeit ist an der TU Wien Bibliothek verfügbar
The approved original version of this thesis is available in print at TU Wien Bibliothek.
TU Bibliothek Your knowledge hub WIEN

[64] John Skilling. "Nested Sampling". In: *Bayesian Inference and Maximum Entropy Methods in Science and Engineering: 24th International Workshop on Bayesian Inference and Maximum Entropy Methods in Science and Engineering*. Ed. by Rainer Fischer, Roland Preuss, and Udo von Toussaint. Vol. 735. AIP Conference Proceedings. Melville, NY: American Institute of Physics, 2004, pp. 395–405. DOI: 10.1063/1.1835238.

[65] Joshua S. Speagle. "dynesty: A Dynamic Nested Sampling Package for Estimating Bayesian Posteriors and Evidences". In: (2020). DOI: 10.1093/mnras/staa278. URL: https://github.com/joshspeagle/dynesty/blob/master/paper/dynesty.pdf.

[66] Mario Spera and Michela Mapelli. "Very massive stars, pair-instability supernovae and intermediate-mass black holes with the SEVN code". In: *Monthly Notices of the Royal Astronomical Society* 470.4 (2017), pp. 4739–4749. DOI: 10.1093/mnras/stx1576. arXiv: 1706.06109 [astro-ph.SR]. URL: https://doi.org/10.48550/arXiv.1706.06109.

[67] The LIGO Scientific Collaboration, J Aasi, B P Abbott, R Abbott, et al. "Advanced LIGO". In: *Classical and Quantum Gravity* 32.7 (2015), p. 074001. DOI: 10.1088/0264-9381/32/7/074001.

[68] Kip S. Thorne. "Multipole Expansions of Gravitational Radiation". In: *Reviews of Modern Physics* 52.2 (1980), pp. 299–339.

[69] Vijay Varma et al. "Surrogate models for precessing binary black hole simulations with unequal masses". In: *Physical Review Research* 1 (2019), p. 033015. DOI: 10.1103/PhysRevResearch.1.033015. arXiv: 1905.09300 [gr-qc]. URL: https://doi.org/10.1103/PhysRevResearch.1.033015.

[70] Robert M. Wald. *General Relativity*. Chicago, IL: University of Chicago Press, 1984.

[71] B. L. Webster and P. Murdin. "Cygnus X-1 - a Spectroscopic Binary with a Heavy Companion?" In: *Nature* 235 (Jan. 1972), pp. 37–38. DOI: 10.1038/235037a0.

[72] Hermann Weyl. "Zur Gravitationstheorie". In: *Annalen der Physik (Leipzig)* 54 (1917), pp. 117–145.

[73] S. E. Woosley and A. Heger. "The Pair-Instability Mass Gap for Black Holes". In: *The Astrophysical Journal* 842.2 (2017), p. 105. DOI: 10.3847/1538-4357/aa743d.

Die approbierte gedruckte Originalversion dieser Diplomarbeit ist an der TU Wien Bibliothek verfügbar
The approved original version of this thesis is available in print at TU Wien Bibliothek.

Die approbierte gedruckte Originalversion dieser Diplomarbeit ist an der TU Wien Bibliothek verfügbar
The approved original version of this thesis is available in print at TU Wien Bibliothek.

Danksagung

Ich möchte diese Arbeit all den Menschen widmen, die mich auf meinem Weg begleitet, unterstützt und inspiriert haben. Ohne euch wäre ich heute nicht hier.

Zunächst gilt mein tiefster Dank meiner Familie – meinen Eltern Teresa und Reinhart, die mir immer den Rücken gestärkt, an mich geglaubt und mich in allen Lebenslagen bedingungslos unterstützt haben. Auch meiner Schwester Kimberly danke ich von Herzen für ihre Ermutigung und dafür, dass sie immer für mich da war. Eure Liebe und Unterstützung haben mich durch die herausforderndsten Zeiten getragen.

Ein besonderer Dank geht an meine Freunde, die mich immer wieder motiviert und dazu gebracht haben, weiterzumachen - selbst wenn es manchmal schwer war. Besonders möchte ich die Freundesgruppe "ApoRassel" hervorheben, die mit ihrem Humor und ihrer Gemeinschaftsfreude unvergessliche Momente geschaffen hat, die mir halfen, den Kopf frei zu bekommen und neue Energie zu tanken.

Mein Dank gilt auch meinen Betreuern Gianluca Inguglia und Christoph Schwanda und dem gesamten Team des HEPHY, die diese Arbeit und meine Forschung erst möglich gemacht haben. Ihre Unterstützung und Expertise waren von unschätzbarem Wert und haben mich inspiriert, mein Bestes zu geben.

Schließlich möchte ich einem Menschen danken, ohne den ich niemals Physik studiert hätte: meinem ehemaligen Oberstufen-Physikprofessor Benjamin Buhr. Seine Begeisterung für die Physik war ansteckend und hat in mir eine Leidenschaft für dieses Fach geweckt, die bis heute anhält. Er hat mir gezeigt, wie faszinierend und erfüllend es sein kann, die Geheimnisse des Universums zu erforschen. Ohne ihn hätte ich vielleicht nie den Mut oder die Überzeugung gefunden, diesen Weg einzuschlagen.

Diese Arbeit ist nicht nur das Ergebnis harter Arbeit, sondern auch das vieler Menschen, die mich inspiriert, unterstützt und an mich geglaubt haben. Euch allen danke ich von Herzen - für alles, was ihr für mich getan habt.

Die approbierte gedruckte Originalversion dieser Diplomarbeit ist an der TU Wien Bibliothek verfügbar
The approved original version of this thesis is available in print at TU Wien Bibliothek.

Die approbierte gedruckte Originalversion dieser Diplomarbeit ist an der TU Wien Bibliothek verfügbar
The approved original version of this thesis is available in print at TU Wien Bibliothek.

A. Theoretical Framework

A.1. Derivation of the Inverse Metric in Linearized Gravity

In the framework of linearized gravity, the metric tensor is expressed as

$$g_{\mu\nu} = \eta_{\mu\nu} + h_{\mu\nu}, \quad \text{with} \quad |h_{\mu\nu}| \ll 1, \tag{A.1}$$

where $\eta_{\mu\nu}$ is the flat Minkowski metric and $h_{\mu\nu}$ represents small perturbations to the metric. The inverse metric $g^{\mu\nu}$ satisfies the condition:

$$g^{\mu\alpha} g_{\alpha\nu} = \delta^{\mu}_{\nu}. \tag{A.2}$$

Assuming a linear expansion for the inverse metric, we write

$$g^{\mu\nu} = \eta^{\mu\nu} + \delta g^{\mu\nu}, \tag{A.3}$$

where $\delta g^{\mu\nu}$ denotes the perturbative correction to the inverse metric. Substituting the expansions of $g^{\mu\nu}$ and $g_{\mu\nu}$ into the inverse condition (A.2), we obtain

$$(\eta^{\mu\alpha} + \delta g^{\mu\alpha})(\eta_{\alpha\nu} + h_{\alpha\nu}) = \delta^{\mu}_{\nu}. \tag{A.4}$$

Expanding the left-hand side and retaining terms up to first order in h and δg, we have

$$\eta^{\mu\alpha}\eta_{\alpha\nu} + \eta^{\mu\alpha} h_{\alpha\nu} + \delta g^{\mu\alpha}\eta_{\alpha\nu} = \delta^{\mu}_{\nu}. \tag{A.5}$$

Simplifying using $\eta^{\mu\alpha}\eta_{\alpha\nu} = \delta^{\mu}_{\nu}$, the equation reduces to

$$\delta^{\mu}_{\nu} + \eta^{\mu\alpha} h_{\alpha\nu} + \delta g^{\mu\alpha}\eta_{\alpha\nu} = \delta^{\mu}_{\nu}. \tag{A.6}$$

Subtracting δ^{μ}_{ν} from both sides yields

$$\eta^{\mu\alpha} h_{\alpha\nu} + \delta g^{\mu\alpha}\eta_{\alpha\nu} = 0. \tag{A.7}$$

Multiplying both sides by $\eta^{\nu\beta}$, we obtain

$$\eta^{\nu\beta}\eta^{\mu\alpha} h_{\alpha\nu} + \eta^{\nu\beta}\delta g^{\mu\alpha}\eta_{\alpha\nu} = 0. \tag{A.8}$$

Die approbierte gedruckte Originalversion dieser Diplomarbeit ist an der TU Wien Bibliothek verfügbar
The approved original version of this thesis is available in print at TU Wien Bibliothek.
TU Bibliothek Your knowledge hub WIEN

Simplifying using $\eta^{\nu\beta}\eta_{\alpha\nu} = \delta^{\beta}_{\alpha}$, the equation becomes

$$\eta^{\mu\alpha}h_{\alpha}^{\ \beta} + \delta g^{\mu\beta} = 0. \tag{A.9}$$

Thus, the perturbative correction to the inverse metric is

$$\delta g^{\mu\beta} = -\eta^{\mu\alpha}h_{\alpha}^{\ \beta}. \tag{A.10}$$

Since $h_{\alpha}^{\ \beta} = \eta^{\beta\gamma}h_{\alpha\gamma}$, we have

$$\delta g^{\mu\nu} = -h^{\mu\nu}. \tag{A.11}$$

A.2. Gauge Transformation in linearized gravity

[50] Consider an infinitesimal change in coordinates given by

$$x'^{\mu} = x^{\mu} + \xi^{\mu}(x), \tag{A.12}$$

where $\xi^{\mu}(x)$ is a small vector field satisfying

$$|\xi^{\mu}| \ll 1. \tag{A.13}$$

This transformation represents a slight shift from the original coordinates x^{μ} to the new coordinates x'^{μ}. Under the coordinate transformation, the spacetime metric in the new coordinates x'^{μ} can be expressed using the tensor transformation law:

$$g'_{\alpha\beta}(x') = \frac{\partial x^{\mu}}{\partial x'^{\alpha}}\frac{\partial x^{\nu}}{\partial x'^{\beta}}g_{\mu\nu}(x). \tag{A.14}$$

Given that ξ^{μ} is small, we can expand the partial derivatives to first order in ξ^{μ}:

$$\frac{\partial x^{\mu}}{\partial x'^{\alpha}} \approx \delta^{\mu}_{\alpha} - \partial_{\alpha}\xi^{\mu}, \tag{A.15}$$

$$\frac{\partial x^{\nu}}{\partial x'^{\beta}} \approx \delta^{\nu}_{\beta} - \partial_{\beta}\xi^{\nu}, \tag{A.16}$$

where δ^{μ}_{α} is the Kronecker delta. Substituting these approximations into the metric transformation, we obtain:

$$\begin{aligned} g'_{\alpha\beta}(x') &\approx \left(\delta^{\mu}_{\alpha} - \partial_{\alpha}\xi^{\mu}\right)\left(\delta^{\nu}_{\beta} - \partial_{\beta}\xi^{\nu}\right)\left(\eta_{\mu\nu} + h_{\mu\nu}\right) \\ &= \eta_{\mu\nu}\delta^{\mu}_{\alpha}\delta^{\nu}_{\beta} + h_{\mu\nu}\delta^{\mu}_{\alpha}\delta^{\nu}_{\beta} - \eta_{\mu\nu}\left(\delta^{\mu}_{\alpha}\partial_{\beta}\xi^{\nu} + \delta^{\nu}_{\beta}\partial_{\alpha}\xi^{\mu}\right) \\ &= \eta_{\alpha\beta} + h_{\alpha\beta} - \partial_{\beta}\xi_{\alpha} - \partial_{\alpha}\xi_{\beta}. \end{aligned} \tag{A.17}$$

Here, we have lowered the indices on ξ^{μ} using the Minkowski metric $\eta_{\mu\nu}$:

$$\xi_{\alpha} = \eta_{\alpha\mu}\xi^{\mu}. \tag{A.18}$$

The new metric perturbation $h'_{\alpha\beta}$ in the transformed coordinates is thus given by

$$h'_{\alpha\beta} = h_{\alpha\beta} - \partial_{\beta}\xi_{\alpha} - \partial_{\alpha}\xi_{\beta}. \tag{A.19}$$

Die approbierte gedruckte Originalversion dieser Diplomarbeit ist an der TU Wien Bibliothek verfügbar
The approved original version of this thesis is available in print at TU Wien Bibliothek.
TU Bibliothek Your knowledge hub WIEN

A.3. Phase and Group velocity of gravitational waves

A wave vector k^μ is termed *null* or *lightlike* if it satisfies the condition:

$$k^\mu k_\mu = 0. \tag{A.20}$$

In Minkowski spacetime this condition expands to:

$$-\left(\frac{\omega}{c}\right)^2 + |\mathbf{k}|^2 = 0 \quad \Rightarrow \quad \omega = c|\mathbf{k}|, \tag{A.21}$$

where ω is the angular frequency of the wave and $\mathbf{k}$ is the spatial wave vector with magnitude $|\mathbf{k}|$. [12]

The **phase velocity** v_p is defined as the rate at which the phase of the wave propagates in space [32]

$$v_p = \frac{\omega}{|\mathbf{k}|}. \tag{A.22}$$

Substituting Equation (A.21) into Equation (A.22) yields:

$$v_p = \frac{c|\mathbf{k}|}{|\mathbf{k}|} = c. \tag{A.23}$$

Thus, the phase velocity equals the speed of light.

The **group velocity** $\mathbf{v}_g$ is the velocity at which the waves envelope[1] propagates through space [32]

$$\mathbf{v}_g = \nabla_{\mathbf{k}}\omega. \tag{A.24}$$

For a null wave vector, where $\omega = c|\mathbf{k}|$, the gradient with respect to $\mathbf{k}$ is:

$$\begin{aligned} \mathbf{v}_g &= \nabla_{\mathbf{k}}(c|\mathbf{k}|) \\ &= c\nabla_{\mathbf{k}}|\mathbf{k}| \\ &= c\frac{\mathbf{k}}{|\mathbf{k}|}. \end{aligned} \tag{A.25}$$

The magnitude of the group velocity is therefore:

$$v_g = |\mathbf{v}_g| = c. \tag{A.26}$$

Hence, the group velocity also equals the speed of light.

[1] the overall shape of the wave's amplitudes

Die approbierte gedruckte Originalversion dieser Diplomarbeit ist an der TU Wien Bibliothek verfügbar
The approved original version of this thesis is available in print at TU Wien Bibliothek.

A.4. Invariance of Gravitational Wave Polarization States under Rotation

To determine the angle of rotation that leaves the polarization states invariant, we perform a coordinate rotation and analyze the transformation of the polarization tensors under this rotation. A rotation in the xy-plane by an angle θ is represented by the rotation matrix [58]

$$R(\theta) = \begin{pmatrix} \cos\theta & \sin\theta & 0 \\ -\sin\theta & \cos\theta & 0 \\ 0 & 0 & 1 \end{pmatrix} \tag{A.27}$$

Under rotation, the polarization tensors transform according to:

$$e'_{ij} = R_{ik}(\theta) R_{j\ell}(\theta) e_{k\ell} \tag{A.28}$$

$$= R(\theta) e_{ij} R^T(\theta) \tag{A.29}$$

Our goal is to find the angle θ such that:

$$e'^{(+)}_{ij} = e^{(+)}_{ij} \quad \text{and} \quad e'^{(\times)}_{ij} = e^{(\times)}_{ij} \tag{A.30}$$

To find the angle θ that satisfies both conditions, we solve the resulting equations from the above transformations. Upon solving, we find that the smallest non-trivial angle that satisfies both conditions is

$$\theta = 180^\circ \tag{A.31}$$

Die approbierte gedruckte Originalversion dieser Diplomarbeit ist an der TU Wien Bibliothek verfügbar
The approved original version of this thesis is available in print at TU Wien Bibliothek.